

Wave-dynamical properties of dielectric resonators investigated with microwaves

Vom Fachbereich Physik
der Technischen Universität Darmstadt

zur Erlangung des Grades
eines Doktors der Naturwissenschaften
(Dr. rer. nat.)

genehmigte

D i s s e r t a t i o n

angefertigt von

Dipl.-Phys. Stefan Bittner
aus Frankfurt am Main

Darmstadt 2010

D 17

Referent: Professor Dr. rer. nat. Dr. h.c. mult. A. Richter
Korreferent: Professor Dr. rer. nat. J. Wambach

Tag der Einreichung: 19. Oktober 2010
Tag der Prüfung: 8. November 2010

But the trouble was that ignorance became more interesting, [...] and people started getting interested in the chaos itself — partly because it was a lot easier to be an expert on chaos, but mostly because it made really good patterns that you could put on a t-shirt. And instead of getting on with proper science (like finding that bloody butterfly whose flapping wings cause all these storms we've been having lately and getting it to stop) scientists suddenly went around saying how impossible it was to know anything, and that there wasn't really anything you could call reality to know anything about, and how all this was tremendously exciting [...]? Incidentally, don't you think this is a rather good t-shirt?

in *Witches Abroad* by Terry Pratchett, from the Discworld series

Abstract

The aim of the experiments described in this thesis was the investigation of different aspects of dielectric resonators with microwave experiments. Dielectric cavities have received much attention in the last years due to applications of microlasers and -cavities in telecommunications, integrated optics or as sensors. A key issue in current research is the correspondence between the ray- and the wave-dynamics in these systems, that is their semiclassical description. Therefore, different semiclassical approaches to dielectric resonators have been tested experimentally with macroscopic flat dielectric microwave resonators. The results can be directly applied to microcavities working in the infrared up to optical frequency regime via scaling as long as the ratio between wavelength and resonator dimensions is similar. Both quasi two-dimensional setups consisting of a dielectric plate squeezed between two metal plates and three-dimensional setups with “levitating” dielectric plates surrounded by air have been investigated. Both the frequency spectra and near field distributions were measured.

In the first part of the thesis, a two-dimensional approximation for three-dimensional flat dielectric resonators has been tested quantitatively with two different circular Teflon disks. The approximation is based on the projection of the three-dimensional ray-dynamics onto two dimensions and the introduction of a so-called effective index of refraction. Comparison of the model calculations with the measured resonance frequencies and widths reveal that they predict the correct order of magnitude, but significant deviations remain. It was thus shown that the model of an effective index of refraction is too imprecise for the detailed understanding of measured frequency spectra, and that furthermore the systematic error of the model calculations is not under control.

In the second part of the thesis, the localization of resonance states on certain periodic orbits was investigated. The existence of such so-called superscars in polygonal metal cavities is well known and was recently predicted also for dielectric polygonal resonators. Therefore, the field distributions of a square ceramic resonator were measured experimentally. The measurements confirmed the existence of superscarred states, but also showed localized states with unexpected character. The physical origin of these states is unclear so far, motivating further investigations.

In the third part of the thesis, a trace formula connecting the resonance density of

two-dimensional dielectric resonators with the periodic orbits of the corresponding classical billiards was investigated with quasi two-dimensional resonators of circular and square shape. The length spectra deduced from the measured frequency spectra reveal contributions of the periodic orbits to the resonance density, but also show significant deviations from the trace formula since only a part of the expected resonances could be observed experimentally. The results demonstrate that the systematics of the observed states must be taken into account for an understanding of the experimental length spectra. A connection between the most long-lived resonances of the cavities and the most strongly confined periodic orbits of the corresponding classical billiards was established.

In the fourth part of the thesis, the applicability of the trace formula for two-dimensional dielectric resonators to flat three-dimensional resonators was investigated. An approach combining the trace formula with the effective index of refraction model investigated in the first part was tested for two flat circular Teflon disks. Preliminary results show good qualitative agreement between the model and the experimental data, but also that additional effects due to the dispersion of the effective index of refraction and due to the systematic error of the model must be taken into account.

Zusammenfassung

Ziel der in der vorliegenden Arbeit beschriebenen Experimente war die Untersuchung verschiedener Aspekte von dielektrischen Resonatoren anhand von Experimenten mit Mikrowellenresonatoren. Dielektrische Resonatoren haben aufgrund der Anwendungen von Mikrolasern und -kavitäten in der Telekommunikation, in integrierten optischen Schaltkreisen oder als Sensoren in den vergangenen Jahren großes Interesse hervorgerufen. Eine der zentralen Fragestellungen ist der Zusammenhang zwischen der Strahlen- und der Wellendynamik in diesen Systemen, entstammt also ihrer semiklassischen Beschreibung. Es wurden verschiedene semiklassische Ansätze für dielektrische Resonatoren experimentell mit Hilfe von makroskopischen, flachen dielektrischen Mikrowellenresonatoren getestet. Die Ergebnisse sind direkt auf Mikrokavitäten im infraroten und optischen Frequenzbereich übertragbar, sofern das Verhältnis der Wellenlänge zur Größe des Resonators vergleichbar ist. Sowohl quasi-zweidimensionale Aufbauten bestehend aus dielektrischen Scheiben zwischen zwei Metallplatten als auch dreidimensionale Aufbauten mit „freischwebenden“, nur von Luft umgebenen dielektrischen Scheiben wurden untersucht. Zusätzlich zu den Frequenzspektren wurden auch Feldverteilungen gemessen.

Im ersten Teil der Dissertation wurde eine zweidimensionale Näherungsmethode für dreidimensionale, flache dielektrische Resonatoren quantitativ untersucht. Dafür wurden zwei kreisförmigen Teflonscheiben verwendet. Die Näherungsmethode basiert auf einer Projektion des dreidimensionalen Strahlengangs im Resonator auf die Ebene und der Einführung eines sogenannten effektiven Brechungsindex. Diese Modellrechnungen ergeben zwar die richtige Größenordnung für gemessene Resonanzfrequenzen und -breiten, aber es verbleiben signifikante Abweichungen. Es wurde gezeigt, daß die Modellrechnungen basierend auf dem effektiven Brechungsindex zu unpräzise für ein detailliertes Verständnis von gemessenen Frequenzspektren sind. Darüber hinaus ist der systematische Fehler der Modellrechnungen nicht unter Kontrolle.

Im zweiten Teil der Dissertation wurden Resonanzzustände untersucht, welche auf bestimmten periodischen Bahnen lokalisiert sind. Solche sogenannten Superscars sind für metallische Polygonbillards bekannt und wurden kürzlich auch für dielektrische vorausgesagt. Daher wurden die Feldverteilungen eines quadratischen Mikrowellenresonators aus Keramik gemessen. Die Messungen bestätigen die Exi-

stanz solcher Superscars, es wurden jedoch auch lokalisierte Zustände mit unerwarteten Eigenschaften gemessen. Da der physikalische Ursprung dieser Zustände nicht klar ist, sind weitere Untersuchungen geplant.

Im dritten der Dissertation Teil wurde eine Spurformel, welche die Resonanzdichte zweidimensionaler dielektrischer Resonatoren mit den periodischen Bahnen des entsprechenden klassischen Billards verknüpft, mittels quasi-zweidimensionaler Mikrowellenresonatoren kreisförmiger und quadratischer Geometrie untersucht. Die aus den gemessenen Frequenzspektren gewonnenen Längenspektren bestätigen den Beitrag der periodischen Bahnen zur Resonanzdichte, jedoch zeigen sich auch deutliche Abweichungen gegenüber den Vorhersagen der Spurformel da nur ein Teil aller Resonanzzustände experimentell beobachtet wird. Für ein Verständnis der experimentellen Längenspektren muß daher die Systematik der beobachtbaren Resonanzen berücksichtigt werden. Darüber hinaus wurde ein Zusammenhang zwischen den langlebigsten Resonanzen des Resonators und den am stärksten im dielektrischen Billiard gebundenen periodischen Bahnen ermittelt. Im vierten Teil der Dissertation wurde die Anwendbarkeit der Spurformel für zweidimensionale dielektrische Resonatoren auf flache dreidimensionale untersucht. Eine Kombination aus der Spurformel und dem Modell eines effektiven Brechungsindex aus dem ersten Teil der Dissertation wurde mit den Daten für zwei Kreisscheiben aus Teflon verglichen. Die vorläufigen Ergebnisse zeigen eine gute qualitative Übereinstimmung, jedoch müssen zusätzlich die Dispersion des effektiven Brechungsindex und der systematische Fehler des Modells aus Teil eins berücksichtigt werden.

Contents

1	Introduction	1
2	Basics	4
2.1	Maxwell and Helmholtz equations	5
2.2	The Helmholtz equation in cylindrical coordinates	6
2.3	Metallic cavity	7
2.4	Dielectric plate between two metal plates	7
2.5	Quasi-bound modes in open dielectric resonators	9
2.6	The two-dimensional dielectric circle	10
2.7	Three-dimensional dielectric plate and effective index of refraction	12
2.8	Measurement of frequency spectra and scattering matrix	15
3	Test of a two-dimensional approximation for flat resonators	18
3.1	Experimental setup and measurements	19
3.2	Comparison of model and experiment	24
3.2.1	Results for disk A	25
3.2.2	Results for disk B	31
3.2.3	Results for a microlaser experiment	34
3.3	Conclusions	36
4	Superscars in the dielectric square billiard	39
4.1	Experimental setup and technique	40
4.2	Measured and constructed superscar states	41
4.3	Summary and outlook	49

5	Trace formula for two-dimensional dielectric cavities	51
5.1	Resonance density and trace formula	51
5.2	Experimental setup	53
5.3	Circular Teflon resonator	55
5.4	Square Teflon resonator	62
5.5	Square alumina resonator	68
5.6	Conclusions	73
6	Trace formula for three-dimensional dielectric cavities	75
6.1	Three-dimensional approach	76
6.2	Approach with effective index of refraction	79
6.3	Conclusions	86
7	Conclusions	88
A	Effective index of refraction for other setups	91
A.1	Setup with additional metal plate	91
A.1.1	Modified Fresnel reflection coefficients	91
A.1.2	Effective index of refraction with additional metal plate	93
A.2	Quasi-2d setup with air gap	96
B	Trace formula for single and multiple subspectra of the dielectric circle	98
B.1	Single resonance family	98
B.2	Two resonance families	100
C	Exact trace formula for the dielectric circle billiard	102

1 Introduction

At the end of the 19th century, it was generally believed that with the establishment of classical mechanics by Newton [1] the calculation of all dynamical problems, including celestial mechanics, became feasible. This was proven wrong by Henri Poincaré with his results on the three-body problem in 1892 [2]. He showed that the solution could not be expanded into a convergent series, and that slightest deviations in the initial conditions resulted in very different trajectories, implying unpredictability of the evolution of the system with time. This highly sensitive dependence on the initial conditions is the essence of chaotic behavior in classical systems: Even though the time evolution of a dynamical system is in principle fully determined by its equations of motion and initial conditions, it cannot be predicted for arbitrarily long times because the initial conditions are only known with finite precision. This seeming contradiction has led to the term *Deterministic Chaos* [3].

The effects of chaotic behavior have not only been studied in classical, but also in quantum systems. Since position and momentum of a particle cannot be measured precisely at the same time in quantum mechanics, other measures to characterize quantum manifestations of classical chaos, so-called quantum chaos, were developed. One is the investigation of the statistical properties of energy spectra. It has been conjectured that the spectral fluctuation properties of chaotic quantum systems are universal and are described by random matrix theory [4], which has been confirmed e.g. for the spectra of nuclei [5–8] and atoms [9]. Furthermore, Gutzwiller introduced the periodic orbit theory with his work on trace formulas for regular [10] and chaotic [11] systems. The trace formulas provide a semiclassical connection between the density of states (DOS) of the quantum system and the periodic orbits (POs) of the corresponding classical system. In general, semiclassics can be used to connect different properties of a quantum mechanical system with those of the analogous classical system [12] and is the second important tool in quantum chaos besides random matrix theory.

Originally it seemed that chaotic motion is a property of very complex systems, but in 1963 Lorenz found, as he investigated a model for convective flow, that also a system with only three degrees of freedom could exhibit chaos [13]. In fact, even systems with only two degrees of freedom can be chaotic. One such class

of systems are two-dimensional (2d) billiards. A billiard is a domain of arbitrary shape inside which a point-like particle moves freely and is reflected elastically at the boundaries of the domain. Therefore, the dynamics is only determined by the shape of the boundary and can be regular (i.e. circle and rectangle billiard), fully chaotic (i.e. stadium billiard [14]) or mixed. Billiards are widely used as model systems both for classical and quantum chaos. In a quantum billiard a particle is confined by an infinitely high potential along its boundary, which can be realized e.g. as electrons in a quantum dot [15]. Below a certain energy a quantum billiard can also be investigated with analog experiments using flat microwave resonators because the stationary Schrödinger equation describing the former is identical to the Helmholtz equation for the latter [16, 17]. In fact, many properties of chaotic quantum systems like the spectral statistics are also found in other wave-dynamical systems like three-dimensional (3d) microwave [18, 19] or acoustic [20, 21] resonators, even though they are not fully equivalent to a quantum billiard. It seems that these properties are universal for systems described by a wave equation, and one also speaks more generally of wave-dynamical chaos. Another interesting class of wave-dynamical systems are dielectric microresonators and -lasers working in the infrared to optical frequency regime. Microlasers were first introduced in 1992 by McCall *et al.* [22] and have since then been a field of intense research due to potential applications in telecommunications, in integrated optics, as sensors etc. [23]. In contrast to closed quantum billiards, dielectric resonators are open systems which lose some of the stored energy by radiation, but can have resonant modes with very long lifetimes (high quality factors Q) due to total internal reflection (TIR). Especially geometries with rotational symmetry like circular disks [22], toroids [24] and spheres [25] are known for their high- Q modes, which have low lasing thresholds. On the other hand, these resonators emit light uniformly due to their symmetry. However, directional emission is required for many applications. This can be achieved with asymmetric (and thus chaotic) resonator geometries, which have the drawback of lower quality factors though [26, 27]. Therefore, one of the main goals of current research is a resonator geometry which combines unidirectional emission with high quality factors. Promising candidates are the Limaçon [28–30] and annular [31] billiard geometries. It has been established that the emission directionality of asymmetric microlasers is closely related to the unstable manifolds of certain

POs of the corresponding classical billiards [32–34]. The classical analog, the so-called dielectric billiard, is an open billiard where at each reflection at the boundary a part of the ray exits according to the Fresnel formulas. Thus, the ray-wave correspondence between the ray-dynamics of the classical billiard and the wave-dynamics of the resonator and semiclassical methods have become very important for the investigation of dielectric cavities. Another point of interest is the occurrence of modes localized on a certain PO. Such states were first found for closed quantum billiards by Heller [35], who called them scars, and have also been reported for microlasers [36, 37].

Since there is no inherent scale in electromagnetism, the properties of a resonator only depend on the ratio between its dimensions and the wavelength. Therefore, results from experiments with dielectric microwave resonators like [33] can be directly applied also to microcavities. The only difference is in the choice of materials, and that the microwave resonators are passive ones whereas the microlasers contain an active medium. The advantage of microwave resonators is their easier handling due to their macroscopic dimensions and the larger frequency range available. They are especially suited to investigate the properties of passive resonators since nonlinear effects due to the active medium like mode-pulling can be excluded. This thesis treats several aspects of dielectric cavities experimentally with dielectric microwave resonators. The basics of the experiments and the theoretical description of dielectric resonators is outlined in chapter 2. In chapter 3, the approximation of flat 3d resonators as 2d objects by introducing a so-called effective index of refraction, n_{eff} , is tested. This approximation, the so-called n_{eff} -model, is widely used in the description of flat dielectric resonators. A test of the model with experimental data is presented. In chapter 4, the electric field distributions of a dielectric square billiard are investigated. This was motivated by the prediction of (super-) scarred states in the dielectric square [38], and the existence of such states could be confirmed experimentally. Chapter 5 presents an experimental test of a trace formula for dielectric cavities recently proposed by Bogomolny *et al.* [39]. The length spectra of several 2d dielectric microwave resonators are compared to the predictions of the trace formula. Chapter 6 finally investigates the length spectra of flat 3d dielectric resonators, and an approach for their theoretical description by combining the trace formula for 2d resonators and the n_{eff} -model is presented. Chapter 7 closes with some final remarks.

2 Basics

In this chapter the basic theory and experimental techniques for (dielectric) microwave resonators are described. Schematic, idealized side views of the different resonator setups discussed in the following are shown in Fig. 2.1. All the resonators shown there are of cylindrical form (with the z -axis parallel to the cylinder axis) with arbitrary shape of the cross section. A closed metallic cavity of height b is shown in Fig. 2.1(a). Such flat cylindrical cavities are used as analogs for 2d quantum billiards [17], where the cross section in the plane perpendicular to the z -axis defines the billiard geometry. Figure 2.1(b) depicts a dielectric plate between two copper plates, used for the experimental realization of a 2d open dielectric resonator. The simplest setup is shown in Fig. 2.1(c): It consists of a flat dielectric plate surrounded only by air (or other materials with lower index

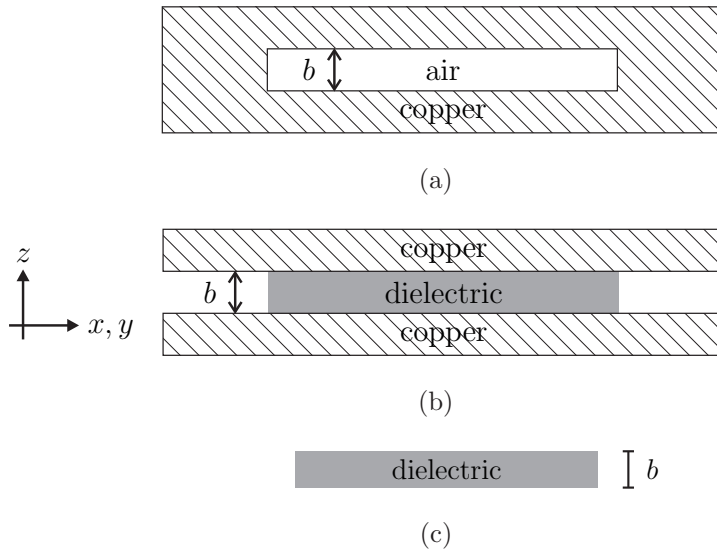


Fig. 2.1: Basic resonator setups (not to scale). (a): A closed metallic cavity. The shape of its cross-section in the plane perpendicular to the z -axis defines the billiard geometry. It is equivalent to a 2d quantum billiard below a certain cutoff frequency. (b): A dielectric plate with arbitrary shape between two copper plates. This setup is the experimental realization of an open 2d dielectric resonator. (c): A dielectric plate surrounded by air (or other media with lower index of refraction). This is the typical setup also of microlasers.

of refraction). Such a setup, e.g. a plate atop a small pillar [22], is often used in microlaser experiments since the use of metallic enclosures is discouraged by the high losses at optical frequencies. In contrast to the other two setups, however, it can be treated only approximately as a 2d system (see chapter 3). In the next section, the solutions of the Helmholtz equation for these setups are discussed.

2.1 Maxwell and Helmholtz equations

The Maxwell equations for the electric (\vec{E}) and magnetic fields (\vec{B}) in a linear, isotropic medium are

$$\begin{aligned}\vec{\nabla} \cdot \vec{E} &= \rho / (\epsilon_r \epsilon_0) & \vec{\nabla} \times \vec{E} &= -\frac{\partial \vec{B}}{\partial t} \\ \vec{\nabla} \cdot \vec{B} &= 0 & \vec{\nabla} \times \vec{B} &= \mu_r \mu_0 \left(\epsilon_r \epsilon_0 \frac{\partial \vec{E}}{\partial t} + \vec{j} \right),\end{aligned}\tag{2.1}$$

where ϵ_r and μ_r are the relative electric and magnetic permeability of the medium, ρ the free charge density and \vec{j} the free electric currents [40]. The general boundary conditions at an interface between two media 1 and 2 are

$$\begin{aligned}\vec{n} \cdot (\vec{E}^{(2)} - \vec{E}^{(1)}) &= \sigma / (\epsilon_r \epsilon_0) & \vec{n} \cdot (\vec{B}^{(2)} - \vec{B}^{(1)}) &= 0 \\ \vec{n} \times (\vec{E}^{(2)} - \vec{E}^{(1)}) &= 0 & \vec{n} \times (\vec{B}^{(2)} - \vec{B}^{(1)}) &= \mu_r \mu_0 \vec{g}\end{aligned}\tag{2.2}$$

with \vec{n} being the surface normal vector pointing to medium 2, and σ and \vec{g} being the surface charge and current densities. Two important cases are a perfect electric conductor as medium 2 or the interface between two dielectric media (with $\mu_r = 1$ each). At the surface S of a perfect conductor, $\vec{B}_\perp|_{\partial S}$ and $\vec{E}_\parallel|_{\partial S}$ must vanish (the indices \perp and \parallel denote the parts of the vector perpendicular respectively parallel to the surface), while $\vec{E}_\perp|_{\partial S}$ and $\vec{B}_\parallel|_{\partial S}$ are discontinuous. At the interface between two dielectrics, the quantities $\epsilon_r^{(j)} \vec{E}_\perp^{(j)}$, $\vec{B}_\perp^{(j)}$, $\vec{B}_\parallel^{(j)}$ and $\vec{E}_\parallel^{(j)}$ ($j = 1, 2$) are continuous.

In absence of free charges and currents, RF fields with harmonic time dependence $e^{-i\omega t}$, where ω is the angular frequency, are described by the vectorial Helmholtz equation

$$(\Delta + n^2(\vec{r}) k^2) \begin{Bmatrix} \vec{E} \\ \vec{B} \end{Bmatrix} = 0.\tag{2.3}$$

Here, $n(\vec{r})$ is the index of refraction at a given point \vec{r} in space, and $k = \omega/c$ is the wave number with c the speed of light in vacuum. The solutions \vec{E} and \vec{B} and the corresponding wave numbers k are called the eigenfunctions and -values of the Helmholtz equation.

2.2 The Helmholtz equation in cylindrical coordinates

Due to the cylindrical geometry of the setups depicted in Fig. 2.1, the vectorial Helmholtz equation (2.3) is solved in cylinder coordinates. Therefore we assume for the fields a harmonic z -dependence, i.e. $\vec{E}, \vec{B} \propto e^{\pm ik_z z}$, $\sin(k_z z)$ or $\cos(k_z z)$ and a time dependence of $e^{-i\omega t}$, which will be suppressed in the following calculations. We also define $\vec{A}_t = A_x \vec{e}_x + A_y \vec{e}_y$ as the transverse component of a vector \vec{A} , respectively $\Delta_t = \frac{\partial^2}{\partial x^2} + \frac{\partial^2}{\partial y^2}$. Then the fields fulfill

$$(\Delta_t + \gamma^2) \begin{Bmatrix} \vec{E} \\ \vec{B} \end{Bmatrix} = 0 \quad (2.4)$$

with

$$\frac{\omega^2}{c^2} = k^2 = \frac{\gamma^2 + k_z^2}{n^2}. \quad (2.5)$$

Some simple calculations yield that the transverse components of \vec{E} and \vec{B} , \vec{E}_t and \vec{B}_t , can be expressed solely in terms of the field components E_z and B_z ,

$$\begin{aligned} \vec{E}_t &= \frac{1}{\gamma^2} \vec{\nabla}_t \frac{\partial E_z}{\partial z} - i \frac{\omega}{\gamma^2} \vec{e}_z \times \vec{\nabla}_t B_z \\ \vec{B}_t &= \frac{1}{\gamma^2} \frac{\partial B_z}{\partial z} + i \frac{\omega n^2}{c^2 \gamma^2} \vec{e}_z \times \vec{\nabla}_t E_z, \end{aligned} \quad (2.6)$$

so that only the Helmholtz equation for E_z and B_z needs to be solved [40]. Depending on the boundary conditions, these equations can be further simplified by considering transverse magnetic (TM) modes with $B_z = 0$ or transverse electric (TE) modes with $E_z = 0$.

2.3 Metallic cavity

For a metallic cavity as shown in Fig. 2.1(a) with bottom plate at $z = 0$ and top plate at $z = b$, the z -dependence of the fields must be $E_z \propto \cos(k_z z)$ and $B_z \propto \sin(k_z z)$ with $k_z = n_z \pi / b$ and n_z integer due to the boundary conditions described in section 2.1. Accordingly, one obtains $E_z|_{\partial S} = 0$ and $\frac{\partial B_z}{\partial n}|_{\partial S} = 0$ at the boundary ∂S in the x - y -plane, with \vec{n} being the normal vector to ∂S . So, E_z and B_z are not coupled, and all modes can be classified as TM_{n_z} and TE_{n_z} modes. Below the frequency

$$f_{2d} = \frac{c}{2nb}, \quad (2.7)$$

only TM_0 modes exist and the resonator is quasi two-dimensional, where n is the index of refraction of the medium filling the cavity (e.g. air). With $n = 1$, the fields for the TM_0 modes are

$$\begin{aligned} \vec{E} &= \Psi(x, y) e^{-i\omega t} \vec{e}_z \\ \vec{B} &= \frac{i}{\omega} \vec{e}_z \times \vec{\nabla}_t \Psi(x, y) e^{-i\omega t}. \end{aligned} \quad (2.8)$$

The function $\Psi(x, y)$ fulfills the scalar Helmholtz equation

$$(\Delta + k^2)\Psi = 0 \quad \text{with} \quad \Psi|_{\partial S} = 0, \quad (2.9)$$

which is identical to the stationary Schrödinger equation for a 2d quantum billiard. Therefore, Ψ is also called wave function. Due to this mathematical identity, flat cylindrical microwave resonators are used as analogs of quantum billiards [16, 17].

2.4 Dielectric plate between two metal plates

For the resonator setup shown in Fig. 2.1(b), the z -dependence of the fields E_z and B_z is the same as in the previous section, but the boundary conditions in transverse direction are more complicated. At an interface ∂S between two dielectric media 1 and 2 with indices of refraction $n_{1,2}$ the continuity conditions

parallel to \vec{e}_z can be summarized as [41]

$$\left. \begin{pmatrix} E_z^{(1)} \\ B_z^{(1)} \end{pmatrix} \right|_{\partial S} = \left. \begin{pmatrix} E_z^{(2)} \\ B_z^{(2)} \end{pmatrix} \right|_{\partial S} \quad (2.10)$$

$$\underline{A}_1 \left. \begin{pmatrix} E_z^{(1)} \\ cB_z^{(1)} \end{pmatrix} \right|_{\partial S} = \underline{A}_2 \left. \begin{pmatrix} E_z^{(2)} \\ cB_z^{(2)} \end{pmatrix} \right|_{\partial S}$$

with the matrices \underline{A}_j

$$\underline{A}_j = \begin{pmatrix} i \frac{kn_j^2}{\gamma_j^2} \frac{\partial}{\partial n} & \frac{1}{\gamma_j^2} \frac{\partial}{\partial z} \frac{\partial}{\partial l} \\ -\frac{1}{\gamma_j^2} \frac{\partial}{\partial z} \frac{\partial}{\partial l} & i \frac{k}{\gamma_j^2} \frac{\partial}{\partial n} \end{pmatrix}. \quad (2.11)$$

Here, \vec{n} is the unit vector normal to ∂S , the unit vector $\vec{l} = \vec{e}_z \times \vec{n}$ lies in the x - y -plane and is tangential to ∂S , and $\gamma_j = \sqrt{n_j^2 k^2 - k_z^2}$. The important point is that E_z and B_z are coupled via the matrices \underline{A}_j , so that there are in general no pure TM or TE modes. They are decoupled only when the off-diagonal elements of \underline{A}_j vanish, e.g. for $k_z = 0$. For the present setup, this is only the case for TM₀ modes. Then, the continuity conditions simplify to

$$\begin{aligned} E_z^{(1)}|_{\partial S} &= E_z^{(2)}|_{\partial S} \\ \text{and } \frac{\partial E_z^{(1)}}{\partial n} \Big|_{\partial S} &= \frac{\partial E_z^{(2)}}{\partial n} \Big|_{\partial S} \end{aligned} \quad (2.12)$$

for TM₀, respectively,

$$\begin{aligned} B_z^{(1)}|_{\partial S} &= B_z^{(2)}|_{\partial S} \\ \text{and } \frac{1}{n_1^2} \frac{\partial B_z^{(1)}}{\partial n} \Big|_{\partial S} &= \frac{1}{n_2^2} \frac{\partial B_z^{(2)}}{\partial n} \Big|_{\partial S} \end{aligned} \quad (2.13)$$

for TE₀ modes. The fields obey the scalar Helmholtz equation

$$(\Delta + n^2(\vec{r})k^2)\Psi = 0 \quad (2.14)$$

where the wave function Ψ signifies E_z for TM respectively B_z for TE modes. It should be noted that a TE₀ mode can only exist in a dielectric cylinder infinitely extended in the z -direction. The general properties of the solutions of the

Helmholtz equation (2.14) for open 2d dielectric resonators are summarized in the next section. It can usually be solved only numerically, e.g. with the boundary element method [42]. The only case of an analytic solution is the dielectric circle, which will be given in section 2.6.

2.5 Quasi-bound modes in open dielectric resonators

While the Helmholtz equation (2.9) for closed metallic resonators has real eigenvalues k and eigenfunctions Ψ , only so-called quasi-bound states exist in a dielectric resonator [described by Eq. (2.14)] due to its openness. The related eigenvalues can be calculated as the poles (i.e. resonances) of the scattering matrix [43–45]. The quasi-bound modes or resonances are characterized by a complex wave number k whose real and imaginary part correspond to the resonance frequency respectively width. The width signifies the losses due to radiation. For a time dependence $e^{-i\omega t}$ the imaginary part of $k = \omega/c$ is negative, and the resonance width (full width at half maximum, FWHM) equals

$$\Gamma = -2\frac{c}{2\pi}\text{Im}(k) , \quad (2.15)$$

the resonance frequency

$$f = \frac{c}{2\pi}\text{Re}(k) . \quad (2.16)$$

The decay rate of the energy stored in the resonator is $2\pi\Gamma$, and the quality factor of a resonance is

$$Q = \frac{f}{\Gamma} = -\frac{\text{Re}(k)}{2\text{Im}(k)} . \quad (2.17)$$

The quality factors of the resonances of a resonator usually differ by several orders of magnitude, and for most applications like lasers with low threshold only those with high Q s are relevant. The above statements generally apply both to 2d and to 3d dielectric resonators.

2.6 The two-dimensional dielectric circle

The 2d dielectric circle billiard is simply a dielectric disk with radius R and index of refraction $n > 1$ surrounded by air ($n = 1$). The solution of the scalar Helmholtz equation (2.14) in polar coordinates (r, φ) is

$$\begin{aligned}\Psi^{(1)}(r, \varphi) &= E_0^{(1)} J_m(nkr) f(\varphi) : r \leq R \\ \Psi^{(2)}(r, \varphi) &= E_0^{(2)} H_m^{(1)}(kr) f(\varphi) : r \geq R\end{aligned}\tag{2.18}$$

with Ψ corresponding to E_z for TM and to B_z for TE modes. For $r > R$, only outgoing solutions are considered because the field mode is excited inside the dielectric disk. Here, $J_m(x)$ is a Bessel-function of the first kind and $H_m^{(1)}(x)$ a Hankel-function of the first kind and order m , where m is the azimuthal quantum number. The function $f(\varphi)$ is either equal to $\cos(m\varphi)$ or $\sin(m\varphi)$, so that all modes with $m > 0$ are doubly degenerate. Imposing the boundary conditions for

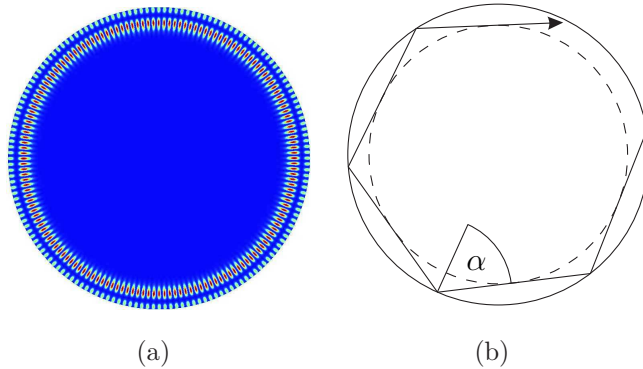


Fig. 2.2: (a): Calculated intensity distribution of a dielectric circle with index of refraction $n = 1.42$. The related mode has quantum numbers ($m = 80$, $n_r = 2$), rescaled resonance frequency $\text{Re}(kR) = 65.6$ and quality factor $Q = 1.4 \cdot 10^7$. The plot shows $|\Psi|^2$ inside the circle in false colors (blue is low and red high intensity). There are $2m$ maxima in azimuthal and $n_r = 2$ rings in radial direction. The mode is of the whispering gallery type with its field intensity located close to the boundary of the circle. (b): Trajectory corresponding to this mode. The dashed line is the caustic of the trajectory and $\alpha = 59.2^\circ$ the angle of incidence with respect to the surface normal.

TM [Eq. (2.12)] respectively TE modes [Eq. (2.13)] on the functions Eq. (2.18) at $r = R$ yields the quantization condition

$$\mu n \frac{J'_m(nkR)}{J_m(nkR)} = \frac{H'_m{}^{(1)}(kR)}{H_m^{(1)}(kR)} \quad \text{with} \quad \mu = \begin{cases} 1 & : \text{ TM} \\ \frac{1}{n^2} & : \text{ TE} \end{cases} \quad (2.19)$$

for the dielectric circle [44]. It can be solved numerically. For each m there is an infinite number of roots k_{m,n_r} , where n_r is the radial quantum number. An example of a calculated wave function is shown in Fig. 2.2(a). The graph shows the field intensity $|\Psi|^2$ for the $(m = 80, n_r = 2)$ -mode. The mode has a very high quality factor of $Q = 1.4 \cdot 10^7$ and its intensity is located close to the boundary of the disk. Such modes are called whispering gallery modes (WGMs). The term comes from the acoustic effect that a person standing at the wall of a circular room and whispering in azimuthal direction can be heard along the circumference, but not in the middle of the room. This phenomenon was first discovered by Rayleigh in St. Paul's cathedral, London, in 1910 (cf. [46, 47]). In fact, all the high- Q modes of the dielectric circle are WGMs with large m and low n_r . Their high quality factors can be explained as follows: Each resonance has an angular momentum of $L_z = \hbar m$. A classical trajectory with the same angular momentum has an angle of incidence α with respect to the surface normal given by [44]

$$\sin \alpha = \frac{m}{nkR}. \quad (2.20)$$

Such a trajectory is shown in Fig. 2.2(b). It has a large angle of incidence α so that the ray is confined in the resonator by TIR, and the corresponding resonance mode has only minimal losses. These are due to tunneling escape at the curved interface [44]. If α is smaller than $\alpha_{\text{crit}} = \arcsin(1/n)$, then a part of the ray escapes at each reflection according to the Fresnel formulas (so-called refractive escape), and the corresponding mode has a low quality factor.

2.7 Three-dimensional dielectric plate and effective index of refraction

The resonator setup shown in Fig. 2.1(c) is the typical setup of microlasers: A dielectric disk of arbitrary shape containing the active medium is placed atop a small pillar [22], on top of a substrate [48] or sandwiched between media of lower index of refraction [49]. The most simple treatment of such setups is to approximate the bulk of the resonator as a dielectric slab waveguide infinitely extended in the plane of the disk (see e.g. [38, 50]). Although the Helmholtz equation for such an infinite slab waveguide can be solved analytically, this is only an approximation because the lateral boundaries of the disk are ignored. They will be discussed further below. The electromagnetic waves can be confined in the slab waveguide by TIR. This corresponds to rays traveling through the waveguide in a zig-zag fashion with angle of incidence greater than the critical angle as illustrated in Fig. 2.3. The fields in the slab waveguide can again be classified as TM or TE modes, and the ansatz for E_z , respectively, B_z corresponding to Fig. 2.3 is

$$\Psi(x, y)e^{-i\omega t} \cdot \begin{cases} (a_1 e^{ik_z z} + a_2 e^{-ik_z z}) & : \text{ inside the slab} \\ b_j e^{-q_j |z|} & : \text{ outside the slab} \end{cases}, \quad (2.21)$$

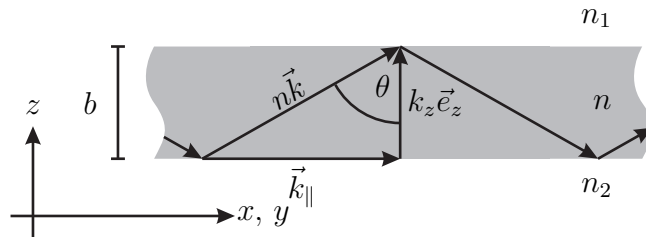


Fig. 2.3: Ray traveling through an infinite dielectric slab waveguide. The slab with index of refraction n and thickness b is surrounded by media of lower indices of refraction $n_{1,2}$. The wave vector $n\vec{k}$ is decomposed into its components perpendicular ($k_z\vec{e}_z$) and parallel (\vec{k}_{\parallel}) to the plane of the waveguide, where $|\vec{k}_{\parallel}| = \gamma = n_{\text{eff}}|\vec{k}|$. The angle of incidence on the surfaces is θ .

where $a_{1,2}$ and $b_{1,2}$ are constants and Ψ fulfills $(\Delta_t + \gamma^2)\Psi = 0$. Due to the TIR, only evanescent fields exist outside the slab which decay exponentially in z -direction with

$$q_j = \sqrt{\gamma^2 - n_j^2 k^2}. \quad (2.22)$$

The effective index of refraction is defined as

$$n_{\text{eff}} = n \sin \theta, \quad (2.23)$$

where θ is the angle of incidence of the rays (see Fig. 2.3). It describes the phase velocity of the waves in the plane of the slab, $\omega/\gamma = c/n_{\text{eff}}$, and the Helmholtz equation for Ψ can be written as

$$(\Delta + n_{\text{eff}}^2 k^2)\Psi(x, y) = 0. \quad (2.24)$$

The allowed values for k_z are determined from the condition

$$e^{2ik_z b} r_1(\theta) r_2(\theta) = 1, \quad (2.25)$$

where $r_j(\theta)$ is the Fresnel coefficient for reflection at the medium j with angle of incidence θ with respect to the surface normal. For θ larger than the critical angle, the Fresnel coefficients can be written in the form

$$r_j = \exp(-2i\delta_j) \quad (2.26)$$

with

$$\delta_j = \arctan \left(\nu_j \frac{\sqrt{n^2 \sin^2 \theta - n_j^2}}{n \cos \theta} \right). \quad (2.27)$$

The parameter ν_j equals n^2/n_j^2 for TM and 1 for TE polarization. With the definition of n_{eff} we furthermore obtain that

$$k_z = k \sqrt{n^2 - n_{\text{eff}}^2}. \quad (2.28)$$

Inserting Eqs. (2.26)–(2.28) into Eq. (2.25) leads to the quantization condition

$$kb \sqrt{n^2 - n_{\text{eff}}^2} = \arctan \left(\nu_1 \frac{\sqrt{n_{\text{eff}}^2 - n_1^2}}{\sqrt{n^2 - n_{\text{eff}}^2}} \right) + \arctan \left(\nu_2 \frac{\sqrt{n_{\text{eff}}^2 - n_2^2}}{\sqrt{n^2 - n_{\text{eff}}^2}} \right) + \zeta \pi \quad (2.29)$$

for the effective index of refraction [38]. The index $\zeta = 0, 1, 2, \dots$ denotes the excitation in z -direction. Usually, the thickness b is chosen such that only modes with $\zeta = 0$ exist in the frequency range of interest. The effective index of refraction only depends on kb , i.e. the ratio between thickness b and wavelength λ , and the indices of refraction. Equation (2.29) can also be deduced by matching the fields in- and outside the slab [Eq. (2.21)] using the boundary conditions from section 2.1.

The idea for modeling the flat 3d dielectric plate of Fig. 2.1(c) is to treat it as a 2d plate with index of refraction equal to n_{eff} . Accordingly the scalar Helmholtz equation

$$\Delta\Psi_{\text{in,out}} = \begin{cases} -n_{\text{eff}}^2 k^2 \Psi_{\text{in}} & : \vec{r} \in S \\ -k^2 \Psi_{\text{out}} & : \vec{r} \notin S \end{cases} \quad (2.30)$$

is used for the wave function $\Psi(x, y)$ in analogy to Eq. (2.14), where S is the domain of the dielectric plate. The material outside the plate is assumed to be air with $n = 1$. Furthermore, boundary conditions analogous to Eqs. (2.12) and (2.13) are imposed, i.e.

$$\Psi_{\text{in}}|_{\partial S} = \Psi_{\text{out}}|_{\partial S} \quad \text{and} \quad \mu \frac{\partial \Psi_{\text{in}}}{\partial n} \Big|_{\partial S} = \frac{\partial \Psi_{\text{out}}}{\partial n} \Big|_{\partial S} \quad (2.31)$$

with $\mu = 1$ for TM and $\mu = 1/n_{\text{eff}}^2$ for TE modes. Equations (2.30) and (2.31) constitute the so-called n_{eff} -model for flat dielectric resonators. The boundary conditions Eq. (2.31) are a simplification as they assume that the fields are homogeneous in z -direction. If this is not the case the more complicated boundary conditions of Eq. (2.10) have to be applied, implying that E_z and B_z are coupled so that there are no states of pure polarization. Furthermore, diffraction at the edges of the disk is neglected. Therefore, the n_{eff} -model only provides an approximate description of the resonator. A drawback of the n_{eff} -model is that it uses a separation of the z and in-plane variables although this is not possible at the cylindrical sidewalls. Its advantage is that it reduces the dimensionality of the problem and that is why it is commonly used. A detailed experimental test of its accuracy concerning the resonance frequencies and widths is given in chapter 3.

2.8 Measurement of frequency spectra and scattering matrix

The resonances of a microwave resonator can be determined experimentally with a vectorial network analyzer (VNA). Two different VNAs, models HP 8510C and N5230A by Agilent Technologies, were used for the experiments presented in this thesis. Antennas attached to the resonator are used to couple in and out RF power (details on the antennas and their usage are given in the corresponding chapters). The antennas are connected via coaxial cables to the VNA, which measures the so-called S -parameter. The squared modulus of the S -parameter is the ratio between the input and output signal of the VNA, or explicitly

$$|S_{ba}(f)|^2 = \frac{P_{\text{out},b}}{P_{\text{in},a}} \quad (2.32)$$

where $P_{\text{in},a}$ is the power coupled into the resonator via antenna a and $P_{\text{out},b}$ is the power coupled out via antenna b for a given frequency f . The function $|S_{ba}(f)|^2$ plotted versus the frequency f yields the frequency spectrum. For $b \neq a$ it is called a transmission and for $b = a$ a reflection spectrum. The VNA furthermore measures the phase shift between input and output signal, or the S -parameter $S_{ba}(f)$, which in fact is a complex quantity.

The system consisting of the resonator and the antennas can be viewed as a scattering system with the antennas acting as scattering channels where S_{ba} is the scattering matrix element for scattering from channel a to channel b . It can be treated with methods developed in nuclear physics for compound nucleus reactions [51]. For an ideal metallic cavity, the scattering matrix in the vicinity of an isolated resonance is of Breit-Wigner shape, and for a series of weakly overlapping resonances it is well described by [52]

$$S_{ba}(f) = \delta_{ba} - i \sum_j \frac{\gamma_j^a \gamma_j^b}{f - f_j + i\Gamma_j/2}. \quad (2.33)$$

The factors in the numerator are proportional to the electric field of the resonance at the positions $\vec{r}_{a,b}$ of the antennas, i.e. $\gamma_j^{a,b} \propto E_z(\vec{r}_{a,b})$. The total width of each resonance is $\Gamma_j = \Gamma_j^a + \Gamma_j^b$, where $\Gamma_j^{a,b} = |\gamma_j^{a,b}|^2$ are the partial widths which describe the loss of energy due to the coupling of the antennas to the resonator. The

transmission scattering matrix element at a resonance frequency f_j is accordingly

$$S_{ba}(f_j) \propto E_z(\vec{r}_b; f_j)E_z(\vec{r}_a; f_j). \quad (2.34)$$

This can be exploited to measure the field distributions of resonances with the so-called scanning antenna technique, which will be treated in more detail in chapter 4. Another method of measuring field distributions, the perturbation body method, is described in chapter 3.

For an open dielectric resonator, the resonance shapes can deviate from the simple Breit-Wigner shape. In addition to the resonance terms in Eq. (2.33), S_{ba} includes contributions due to direct transmission between the antennas. For closed cavities, the direct transmission is usually negligible, but this is not the case for dielectric cavities. This can lead to resonances with Fano profile [53], but usually the resonance shape is still described reasonably well by the Breit-Wigner shape, and the resonance frequencies and widths are extracted from the measured spectra using Eq. (2.33) with the program *GWignerfit* [54].

In an experiment, there are losses in addition to the energy coupled out by the antennas. First, there are Ohmic losses (Γ_Ω) in the metallic components of a cavity. These can be reduced almost to zero with superconducting cavities made of niobium or lead-plated copper [55]. In an open dielectric resonator, there are furthermore losses due to radiation and due to absorption in the dielectric material. The radiation losses (Γ_{rad}) are accounted for by Eq. (2.15) and are an intrinsic property of each resonance like the resonance frequency. Therefore, they cannot be avoided or reduced except by changing the resonator shape. The absorption losses are determined by the properties of the dielectric medium, which are usually characterized by the loss tangent

$$\tan \delta = \frac{|\text{Im}(\epsilon_r)|}{\text{Re}(\epsilon_r)}, \quad (2.35)$$

that is, the angle between the real and imaginary part of the dielectric constant. For low loss materials like Teflon, the loss tangent is in the order of 10^{-4} – 10^{-3} , and the absorption loss Γ_{abs} of the resonator is approximately given by

$$\Gamma_{\text{abs}} = f \tan \delta. \quad (2.36)$$

The total width of a resonance (including possible Ohmic losses if metal plates are used) is then

$$\Gamma_j = \Gamma_j^a + \Gamma_j^b + \Gamma_\Omega + \Gamma_{\text{rad}}^j + \Gamma_{\text{abs}}. \quad (2.37)$$

The resonance widths in an experiment are therefore expected to be somewhat larger than predicted by the solutions of the Helmholtz equation, as there only Γ_{rad}^j is accounted for.

3 Test of a two-dimensional approximation for flat resonators

Dielectric microcavities have been constructed with many different shapes and geometries (including e.g. microtoroids [24] and -spheres [25]), but the most common ones are flat cylindrical plates with circular [22] or asymmetric cross section [56]. This typical geometry is illustrated in Fig. 3.1(b), with the thickness b of the disk being usually much smaller than its transverse dimensions. The limiting cases are the 2d disk in Fig. 3.1(a) and the infinitely long cylinder in Fig. 3.1(c). The resonance frequencies of 2d dielectric resonators of arbitrary shape can be computed e.g. with the boundary element method [42], and quasi-2d resonators can be realized experimentally by squeezing a dielectric plate between two (infinitely extended) metal plates (see section 2.4). Such a setup has been constructed with macroscopic dielectric microwave resonators [33] and is also used in chapter 5. However, it is not suitable for microcavities due to the large losses in metals at optical frequencies. The case of an infinitely long cylinder can also be reduced to a 2d problem by separation of variables (see [41] and sections 2.2 and 2.4). An experimental realization are e.g. ZnO nanorods [57] or liquid microjets [58]. The most common setup, the microdisk with finite thickness b , however, cannot be solved analytically, and 3d numerical simulations using e.g. the finite difference time domain method are feasible, but computationally demanding [59, 60].

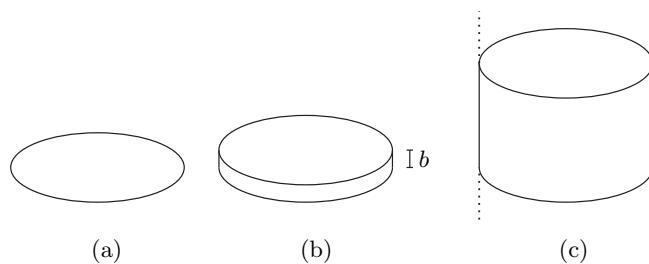


Fig. 3.1: Geometry of microlasers. The typical design of a plate with thickness b much smaller than its transverse dimension is shown in panel (b). The limiting cases are the 2d disk shown in panel (a) and the infinitely long cylinder in panel (c). The cross section is circular here, but can generally be of any shape.

Therefore, a 2d approximation for the disk with finite thickness is favorable. This is commonly done by introducing an effective index of refraction n_{eff} as explained in section 2.7. In the following, we will test the n_{eff} -model rigorously by comparing measured resonance frequencies and widths of two different circular dielectric microwave resonators with calculations based on the n_{eff} -model. The key results have been published in [61].

3.1 Experimental setup and measurements

Figure 3.2 shows a sketch of the experimental setup: A circular Teflon disk is hanging down from three metal suspensions, but is otherwise surrounded by air. Two antennas put on opposite sides of the disk are used to couple in and out RF power and the whole setup is surrounded by a thermostat to keep it at a fixed temperature. The three suspensions form an equilateral triangle. They perturb the resonator only negligibly due to two reasons: First, the only observed modes are of WGM type and the distance of the suspensions from the center of the disk is only 145 mm compared to a radius of $R = 275$ mm, so that the WGMs which are localized near the boundary of the disk have no overlap with the suspensions, and second, while the suspensions are made of metal, the actual bolts going through the Teflon disk are also made of Teflon. Further perturbations are caused by the antennas themselves and the bending of the resonator under its own weight,

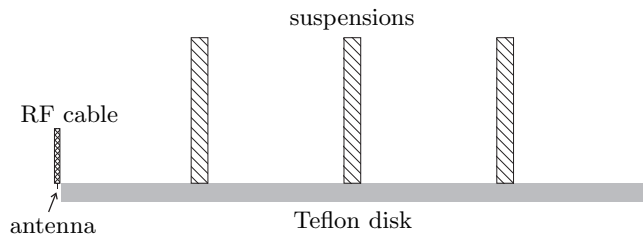


Fig. 3.2: Schematic side view of the experimental setup (not to scale). The Teflon disk is hanging on three metal suspensions. Two dipole antennas protruding from an RF cable are placed close to the rim of the disk on opposite sides. Reprinted from [61].



Fig. 3.3: Sketches of the two antenna types. Left: The dipole antenna is an inner conductor protruding about 4.5 mm from a semi-rigid coaxial cable. Right: Curved antenna with a total length of about 30 mm. The cylindrical sidewall of the Teflon disk is shown in gray in the background. Both types of antennas are placed directly alongside the sidewall of the disk to obtain good coupling to the resonator.

but these shift the resonance frequencies by less than 2% of the mean resonance spacing, i.e. less than 4 MHz for a resonance spacing of about 120 MHz. The two types of antennas used are shown in Fig. 3.3: Vertical dipole antennas were utilized to excite mainly TM modes, while the so-called curved antennas excite mainly TE modes. The antennas may slightly lift the double degeneracy of the WGMs.

The experiments were performed with circular disks made of Teflon (by the company Grünberg Kunststoffe GmbH). Two disks with different thickness b were studied to investigate the relation between the aspect ratio R/b and the precision of the n_{eff} -model. Disk A has a radius of $R = 274.8$ mm and a thickness of $b = 16.7$ mm, and disk B of $R = 274.9$ mm and of $b = 5.0$ mm. A frequency of 10 GHz corresponds to $kR = 57.6$, and $kb = 3.5$ (disk A) and $kb = 1.0$ (disk B), respectively. The indices of refraction were determined as $n = 1.434 \pm 0.01$ for disk A and $n = 1.439 \pm 0.01$ for disk B with a split-cylinder resonator technique [62, 63]. A frequency spectrum of disk A measured with dipole antennas is shown in Fig. 3.4. The spectrum shows a superposition of several series of almost equidistant resonances. Each series (or subspectrum) consists of modes with fixed polarization and radial quantum number n_r and increasing azimuthal quantum number m as indicated in the lower panel of Fig. 3.4. The resonance spacings of each subspectrum are of the order of 120–130 MHz, with slightly larger resonance spacings for the series with larger n_r . For each subspectrum, the resonance

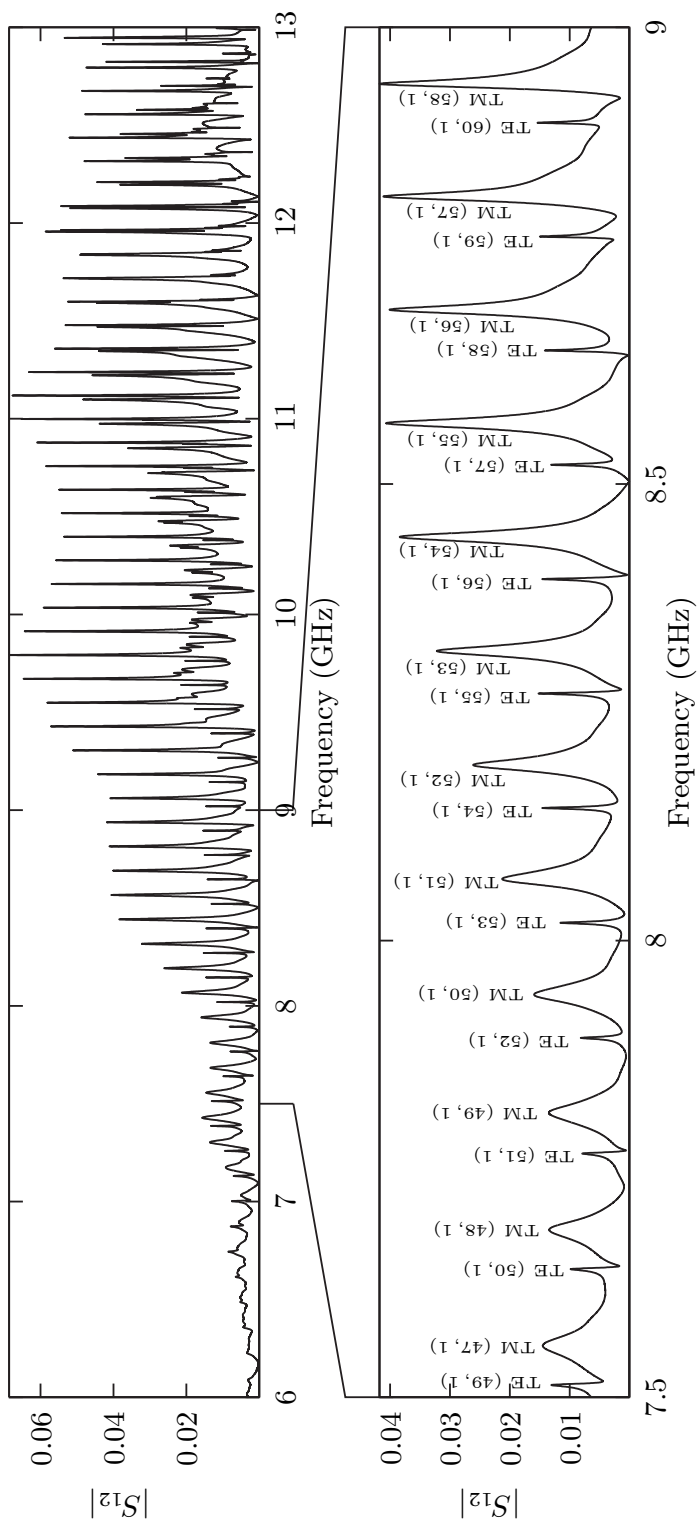


Fig. 3.4: Frequency spectrum of disk A measured with dipole antennas. The transmission amplitude, i.e. $|S_{12}|$, is shown with respect to the frequency f . In the magnified part of the spectrum, the resonances are labeled with TM or TE(m, n_r) to indicate their polarization as well as their azimuthal and radial quantum numbers m and n_r , respectively. Two series of resonances are observed: the broader and larger resonances correspond to modes with TM polarization and radial quantum number $n_r = 1$, the sharper and smaller resonances to modes with TE polarization and $n_r = 1$. Resonances with $n_r > 1$ can also be seen at higher frequencies. Reprinted from [61].

widths decrease with increasing azimuthal quantum number, while resonances with higher radial quantum number have larger widths than those with lower n_r at the same frequency. This can be explained within the ray-picture presented in section 2.6: Each resonance can be associated with a classical trajectory of the same angular momentum $L_z = \hbar m$. A higher angular momentum, respectively, azimuthal quantum number implies a larger angle of incidence [cf. Fig. 2.2(b)] and thus lower radiation losses. As a consequence, the different subspectra only become distinguishable above a certain frequency.

The polarization (TM or TE) of the resonances can be guessed from their different amplitudes for dipole or curved antennas, but the polarizations were additionally determined unambiguously with a perturbation technique: a metal plate was introduced parallel to the Teflon disk with varying vertical distance D , shifting the resonance frequencies as shown in Fig. 3.5. The direction of the shift depends on the polarization of the modes: TE modes are shifted to higher frequencies with decreasing distance D while TM modes are shifted to lower frequencies. A detailed explanation of this effect is given in appendix A.1.

In order to determine the quantum numbers of the resonance modes, the in-

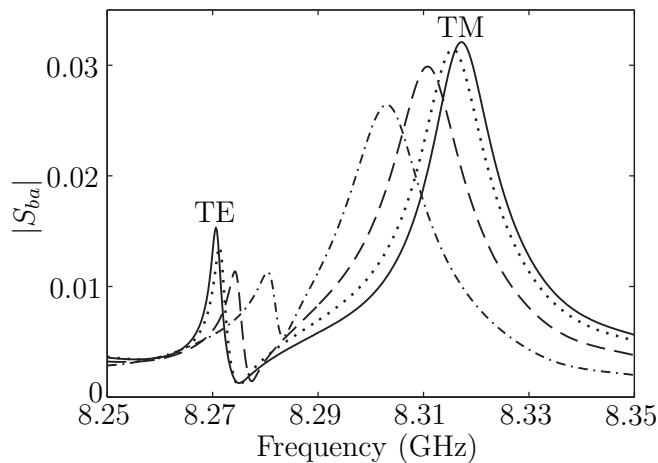


Fig. 3.5: Shift of resonances due to the influence of a metal plate parallel to the Teflon disk. The solid line is the unperturbed spectrum (same as in Fig. 3.4), the dotted line is the spectrum with a metal plate at a distance of $D = 16$ mm, the dashed line for $D = 10$ mm and the dash-dotted line for $D = 6$ mm. With decreasing D the TE modes are shifted to higher, the TM modes to lower frequencies.

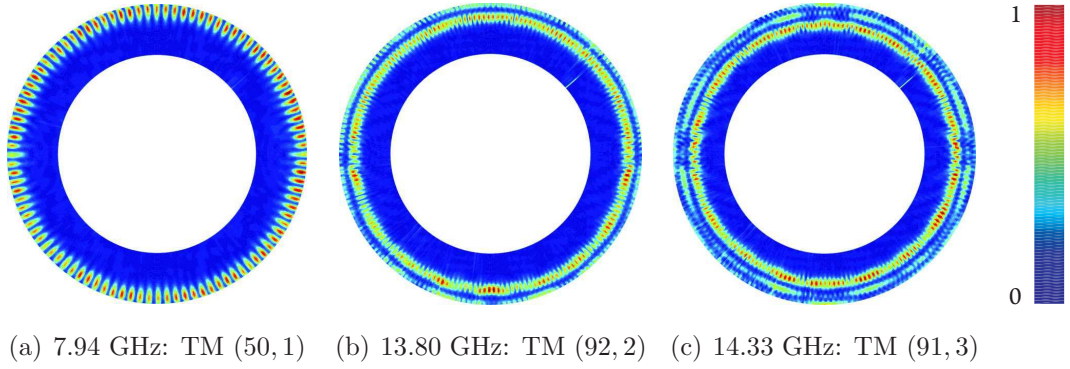


Fig. 3.6: Measured intensity distributions of three TM modes with quantum numbers (m, n_r) . A mode with azimuthal quantum number m and radial quantum number n_r has $2m$ maxima in azimuthal direction and n_r rings. Shown are modes of whispering gallery type, as are all other identifiable modes. Therefore, the intensity distributions were only measured in the outer ring of the resonator. Adapted from [61].

tensity distributions were measured with the perturbation body method [64]. A perturbation body made of magnetic rubber [65, 66] was moved along the surface of the disk by a computer controlled positioning unit developed in [66]. The dimensions of the cylinder (diameter of 4 mm and height of 8 mm) are small compared to a free space wavelength of $\lambda = 30$ mm at 10 GHz. The shift of the resonance frequency f_j induced by the perturbation body at position \vec{r} equals

$$\Delta f_j(\vec{r}) \propto -|\vec{E}_j(\vec{r})|^2. \quad (3.1)$$

Thus, the electric field intensity can be mapped by measuring Δf_j for different positions of the perturbation body. In practice, only the shift of the phase of the scattering matrix element S_{ba} at the resonance is measured, which is in turn proportional to the shift of the resonance frequency¹, so that

$$\Delta \arg [S_{ba}(f_j)] \propto -|\vec{E}_j(\vec{r})|^2. \quad (3.2)$$

It should be noted that this simple relation between phase shift and field intensity fails for strongly overlapping resonances. Three examples of measured intensity distributions are shown in Fig. 3.6. The modes are of the WGM type, as are all

¹Consider Eq. (2.33) for an isolated resonance and a small shift of the resonance frequency.

measured resonances. Therefore, the intensity distributions were only measured close to the boundary of the disk. The azimuthal and radial quantum numbers (m, n_r) were determined simply by counting the number of field maxima in radial and azimuthal direction (see section 2.6). The knowledge of the polarization and quantum numbers enables a direct comparison of the measured resonance frequencies and widths with those computed from the n_{eff} -model.

3.2 Comparison of model and experiment

In the following, the experimental data is compared to calculations based on the n_{eff} -model, i.e. Equations (2.30) and (2.31). The solution of this set of equations for the circle is then the same as for the 2d dielectric circle, but with the index of refraction n replaced by the effective index of refraction, $n_{\text{eff}}(k)$. So the resonance frequencies and widths are computed by solving

$$\mu n_{\text{eff}} \frac{J'_m(n_{\text{eff}} k R)}{J_m(n_{\text{eff}} k R)} = \frac{H_m^{(1)}(k R)}{H_m^{(1)}(k R)} \quad \text{with} \quad \mu = \begin{cases} 1 & : \text{ TM} \\ \frac{1}{n_{\text{eff}}^2} & : \text{ TE} \end{cases} . \quad (3.3)$$

The effective index of refraction is calculated according to Eq. (2.29), with $n_1 = n_2 = 1$ for air, and with n and b for disk A and B given in the previous section. The effective index of refraction is shown in Fig. 3.7(a) for disk A and in Fig. 3.7(b) for disk B. The effective index of refraction is increasing monotonically with increasing frequency and is always in between the indices of refraction of the surrounding media ($n_j = 1$ here) and the index of refraction of the Teflon itself. The solid lines are for the TM and the dashed lines for the TE modes. For a given frequency, n_{eff} for disk A is always larger than n_{eff} for disk B because disk A is thicker. At about 8.76 GHz, modes with higher z -excitation ($\zeta = 1$) begin to exist for disk A, and further z -excitations for higher frequencies. Obviously, n_{eff} is strongly frequency dependent, and the dependence on (the real part of) k is fully taken into account when solving Eq. (3.3).

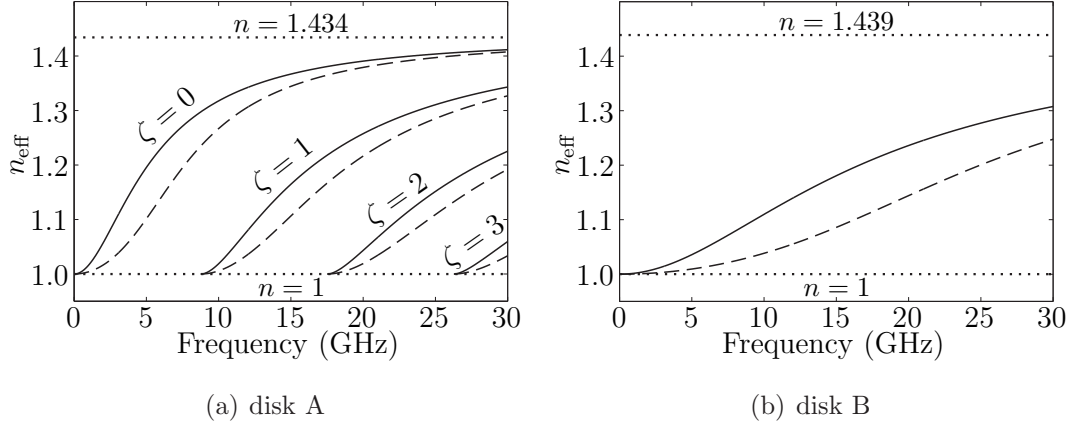
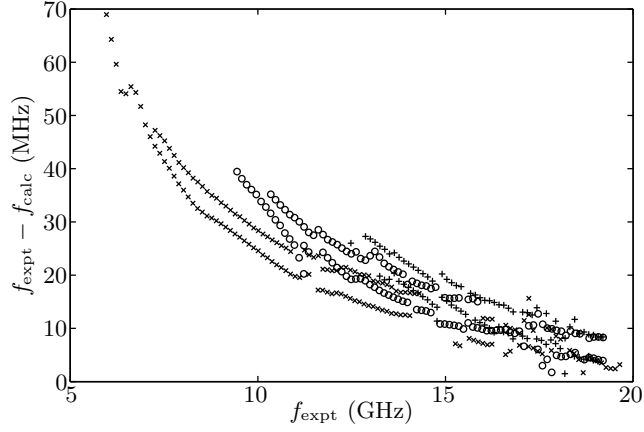


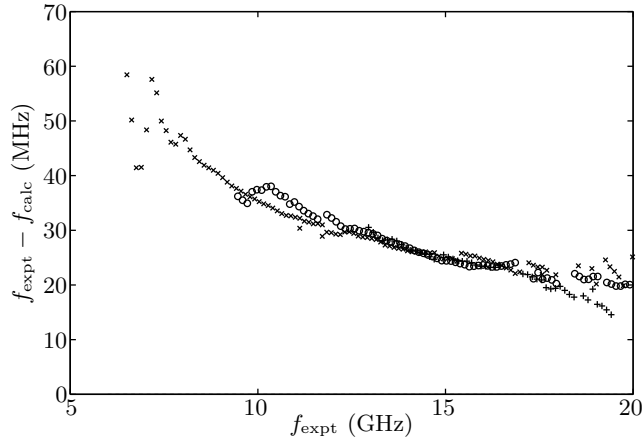
Fig. 3.7: Effective index of refraction n_{eff} with respect to the frequency for disk A with $b = 16.7$ mm (left) and disk B with $b = 5.0$ mm (right). The solid lines correspond to the TE modes, the dashed lines to the TM modes with various z -excitations. The dotted lines are the indices of refraction of the Teflon and air, respectively.

3.2.1 Results for disk A

The difference between the measured resonance frequencies f_{expt} of disk A ($b = 16.7$ mm thick) and those calculated with Eq. (3.3), f_{calc} , are shown in Fig. 3.8. There are actually two series of data points for each radial quantum number n_r in the case of the TE modes in Fig. 3.8(a) because the curved antennas used in the measurement slightly lift the degeneracy of the modes. The data points scatter around the frequency dependent average by about 5 MHz. This stems from problems with the determination of the resonance frequencies, either because the resonances are badly shaped (at lower frequencies) or because of overlapping resonances (at higher frequencies). Some resonances are also missing in the experimental data due to the overlap with others. Although the deviations between the measured and computed resonance frequencies are less than 1%, they must still be considered significant. The deviations are as large as half a resonance spacing (up to 60 MHz compared to a spacing of 120 MHz), rendering impossible the correct identification of the resonances just by comparison with the model calculations. The deviations are a bit larger for modes with higher n_r , especially for the TE modes. With increasing frequency the difference between the calculated and measured resonance frequencies decreases and appears to reach a finite value, which is different for the two polarizations, though. Thus, although the



(a) TE modes



(b) TM modes

Fig. 3.8: Difference between measured (f_{expt}) and calculated (f_{calc}) resonance frequencies with respect to f_{expt} for disk A. The different symbols correspond to the different radial quantum numbers (\times : $n_r = 1$; \circ : $n_r = 2$; $+$: $n_r = 3$). (a) TE modes: the range of azimuthal quantum numbers for $n_r = 1$ is $m = 37$ – 148 . (b) TM modes: the range of azimuthal quantum numbers for $n_r = 1$ is $m = 39$ – 150 . The measurement was done with dipole antennas, and no break up of degenerate modes was observed. Reprinted from [61]

calculations are more precise in the high frequency or, equivalently, semiclassical limit, the experimental data indicates a systematic failure of the n_{eff} -model in all frequency regimes. Furthermore, the calculations overestimate the resonance spacings by about 0.4 MHz, though the exact magnitude of this deviation

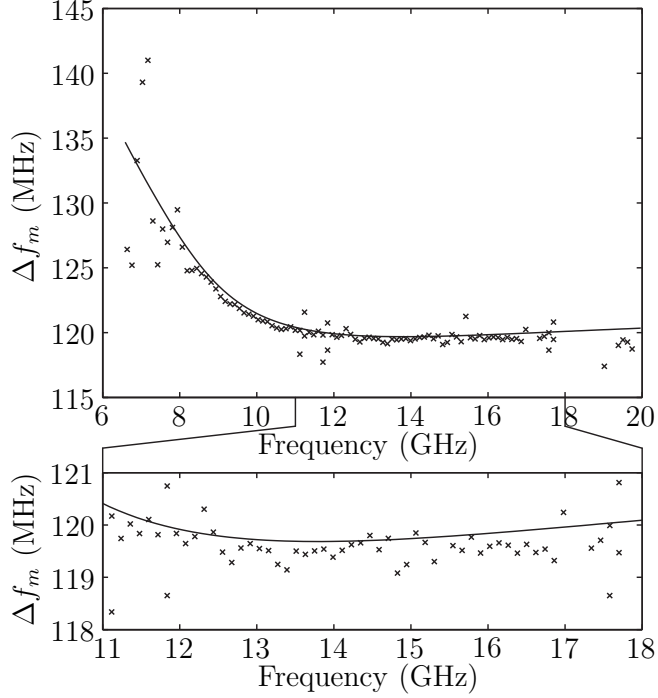


Fig. 3.9: Comparison of the spacings $\Delta f_m = f_m - f_{m-1}$ between consecutive resonances for the TM modes of disk A with $n_r = 1$. The calculated spacings (shown as solid line to guide the eye) are slightly, but systematically larger than the measured ones. The deviation between calculated and measured spacings is in the order of 0.4 MHz, as can be seen from the magnified part (bottom panel).

is hard to tell due to the uncertainty in the experimental data. This is illustrated in Fig. 3.9, which shows the resonance spacings Δf_m between TM modes with $n_r = 1$. The experimental resonance spacings (\times) lie slightly, but systematically below the calculated ones (solid line). Thus the difference between calculated and measured spacings is small and hardly visible when comparing measured and calculated spectra, but adds up significantly over a larger frequency range. The same applies to other radial quantum numbers and the TE modes.

The calculated resonance frequencies and thus their deviations from the measured ones depend sensitively on the index of refraction n , which is only known with an uncertainty of $\Delta n = 0.01$. In Fig. 3.10, the differences $f_{\text{expt}} - f_{\text{calc}}$ between the measured resonance frequencies and three calculations with different indices of refraction are shown. The index of refraction was varied by only 0.002 there,

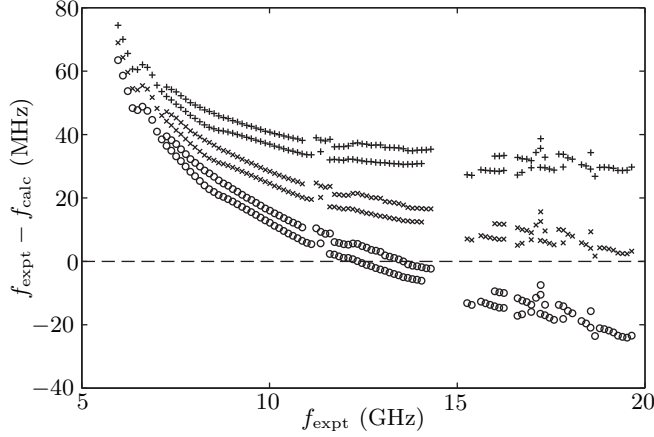
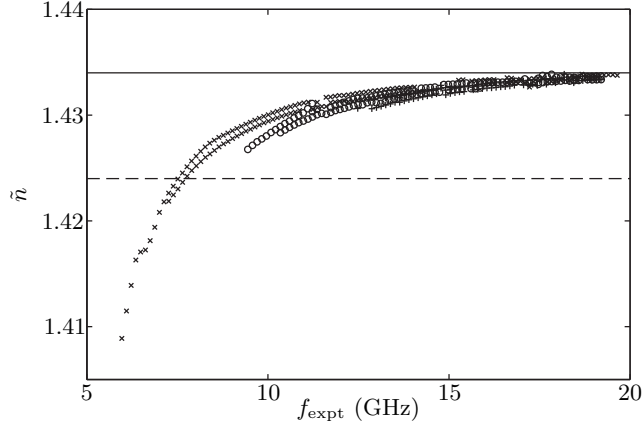
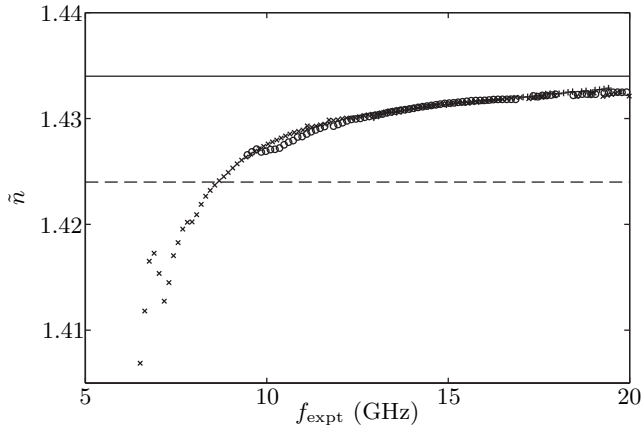


Fig. 3.10: Difference between measured (f_{expt}) and calculated (f_{calc}) resonance frequencies with respect to f_{expt} for the TE modes of disk A. Results from three different calculations with three different indices of refraction $n = 1.432$ (\circ), 1.434 (\times), and 1.436 ($+$) are shown. Only resonances with $n_r = 1$ are considered for the sake of clarity. Reprinted from [61].

which is even less than Δn . Only the data points with $n_r = 1$ are displayed since those for higher n_r show a similar behavior. The magnitude of the deviations is roughly the same for low frequencies, but very different in the semiclassical regime. Accordingly, due to the experimental uncertainty Δn , it is unclear whether the deviations reach a finite value for high frequencies or whether they even increase again at some point. In order to come to a conclusion independent of the measured n , the index of refraction was also considered as a fit parameter called \tilde{n} . For each resonance, it was varied such that Eq. (3.3), which depends on the index of refraction implicitly via n_{eff} , yields the measured resonance frequency. The thus obtained values of \tilde{n} are expected to scatter around the real index of refraction n if the n_{eff} -model describes the resonator correctly. Figure 3.11 shows the fitted \tilde{n} -values. The data points lie inside the error band $n - \Delta n$ except for low frequencies, but they do not scatter around some constant value and form three distinct curves corresponding to the different radial quantum numbers instead of just one. This is clear evidence for the failure of the n_{eff} -model, since n should not depend on the polarization or n_r . Furthermore, the \tilde{n} -curves show a relatively strong frequency dependence, but it is known from literature and was



(a) TE modes



(b) TM modes

Fig. 3.11: Values of the index of refraction \tilde{n} for which Eq. (3.3) yields the measured resonance frequencies for (a) the TE modes and (b) the TM modes of disk A. The different symbols denote the different radial quantum numbers (\times : $n_r = 1$; \circ : $n_r = 2$; $+$: $n_r = 3$). The solid line indicates the real index of refraction n of the disk, the dashed line the value of $n - \Delta n$, i.e. the lower end of the error band for n . The systematic deviation of the data points from the measured n signifies the failure of the n_{eff} -model. Reprinted from [61].

confirmed by our own experiments that Teflon has negligible dispersion in the considered frequency range. We conclude that, since it is impossible to achieve agreement between f_{expt} and f_{calc} in the whole frequency range with a single, fixed value of n , the deviations between model and experiment are not due to an incorrectly determined index of refraction. The same applies for the radius R

and the thickness b , or combinations of all three parameters. With experimental inaccuracies for the parameters and the measured resonance frequencies excluded as sources for the observed deviations, the following conclusion has to be drawn: the calculations do not correctly describe the measured resonance frequencies due to systematic errors of the n_{eff} -model.

As a further test of the n_{eff} -model, Fig. 3.12 shows the comparison of measured and calculated resonance widths of the TM modes. The experimental resonance widths Γ_{expt} are obtained by fitting Breit-Wigner curves to the measured resonance shapes and contain losses due to radiation, absorption and the antennas as described in section 2.8. The widths Γ_{calc} are computed via Eq. (2.15) and account only for the radiation losses. Even though the measured widths contain additional loss mechanisms, the calculated widths are up to twice as large for low frequencies (up to 8 GHz for $n_r = 1$ and up to 10.5 GHz for $n_r = 2$). On the other hand, the measured widths saturate at a value of about 4 MHz for higher frequencies. There the absorption and antenna losses, which are approximately

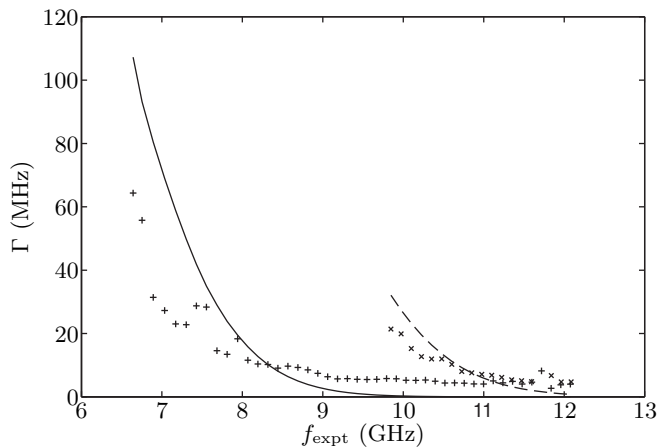
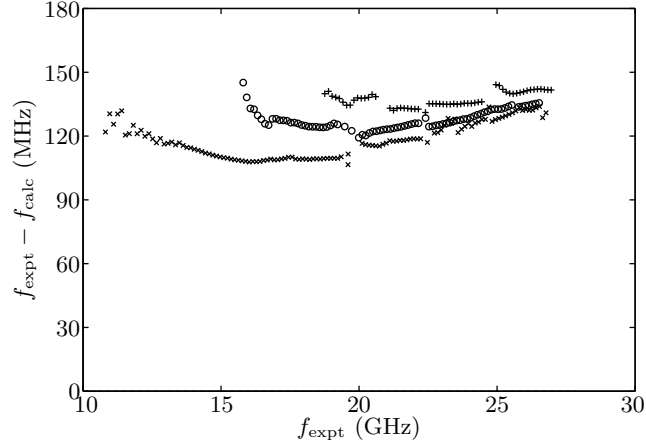


Fig. 3.12: Measured (Γ_{expt}) and calculated (Γ_{calc}) resonances widths for TM modes of disk A. Both Γ_{expt} and Γ_{calc} are plotted as function of the measured resonance frequency f_{expt} . The symbols denote the measured widths for different radial quantum numbers (+: $n_r = 1$; \times : $n_r = 2$). The calculated widths are plotted as curves (solid line for $n_r = 1$, dashed for $n_r = 2$) instead of data points to guide the eye. The calculations clearly overestimate the widths at least in some frequency regimes. Reprinted from [61].

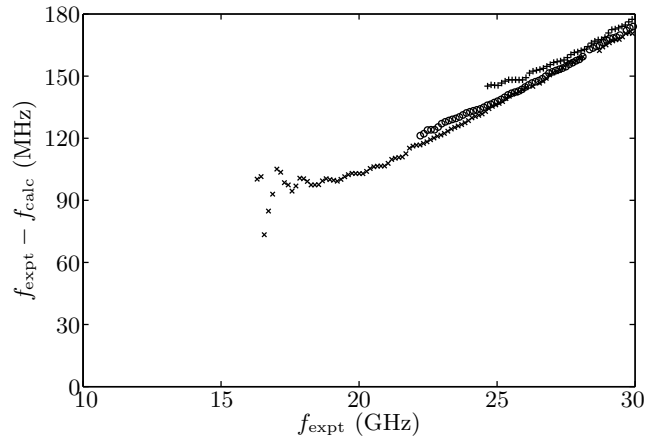
independent of the frequency, become dominant. Since the radiation losses Γ_{rad} can generally not be extracted from the measured widths Γ_{expt} , a quantitative comparison with the calculated widths is not possible. Nonetheless it is certain that the widths Γ_{calc} predicted by the n_{eff} -model are in general too large, and the actual differences are even larger than shown in Fig. 3.12 since Γ_{calc} does not account for absorption and antenna losses. This means that the n_{eff} -model fails to accurately predict both resonance frequencies and widths of the resonator. Since Γ_{calc} does not depend as sensitively on n as the resonance frequencies, the above statements are valid even under consideration of the uncertainty of the index of refraction. The widths for the TE modes show the same trend although the difference between Γ_{expt} and Γ_{calc} is not as large as for the TM modes.

3.2.2 Results for disk B

The differences between the measured and calculated resonance frequencies for the thinner disk B ($b = 5.0$ mm) is shown in Fig. 3.13. The frequency range of identifiable TE and TM modes differs due to the different quality factors of the resonances and the different antenna types used. A comparison with Fig. 3.8 shows that they seem to be larger than for disk A, but of the same order of magnitude, i.e. approximately equal to one resonance spacing. The difference even seems to increase with the frequency unlike the case of disk A, but this behavior depends sensitively on n as demonstrated for disk A in Fig. 3.10. In fact, the deviations can increase, decrease or reach a finite value in the semiclassical limit for different values of n within the range of accuracy $\Delta n = 0.01$. Nonetheless the deviations for disk B are somewhat larger than for disk A at least in the regime up to 20 GHz. The index of refraction \tilde{n} needed to obtain the measured resonance frequencies from Eq. (3.3) is shown in Fig. 3.14. The fitted values \tilde{n} increase with the frequency and seem to reach a certain value which depends on the polarization, and \tilde{n} follows a different curve for each radial quantum number, that is, the qualitative behavior is the same as for disk A in Fig. 3.11. This again demonstrates the systematic failure of the n_{eff} -model. In fact, the errors seem to be larger for the thinner disk, and also the dependence on n_r is more pronounced.

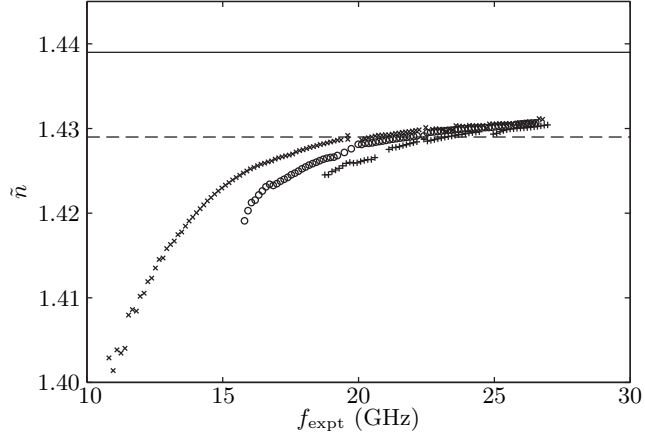


(a) TE modes

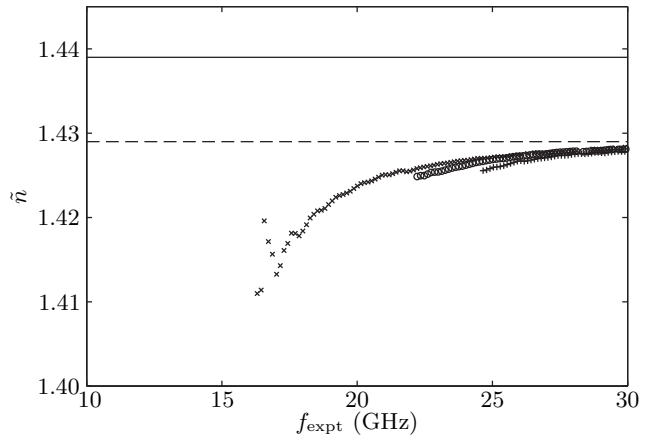


(b) TM modes

Fig. 3.13: Difference between measured (f_{expt}) and calculated (f_{calc}) resonance frequencies with respect to f_{expt} for disk B. The symbols correspond to the different radial quantum numbers (\times : $n_r = 1$; \circ : $n_r = 2$; $+$: $n_r = 3$). The TE modes measured with curved antennas are plotted in graph (a) and have a range of azimuthal quantum numbers $m = 64$ – 188 for resonances with $n_r = 1$. The TM modes shown in graph (b) were measured with dipole antennas and have azimuthal quantum numbers $m = 97$ – 204 for $n_r = 1$. Reprinted from [61].



(a) TE modes



(b) TM modes

Fig. 3.14: Index of refraction \tilde{n} required to reproduce the measured resonance frequencies with Eq. (3.3) as a function of the resonance frequency f_{expt} for disk B. Each symbol corresponds to a radial quantum number (\times : $n_r = 1$; \circ : $n_r = 2$; $+$: $n_r = 3$), the solid lines denote the index of refraction $n = 1.439$ of the disk and the dashed line $n - \Delta n$ its range of accuracy. Panel (a) shows the data points for the TE modes, panel (b) those for the TM modes. Reprinted from [61].

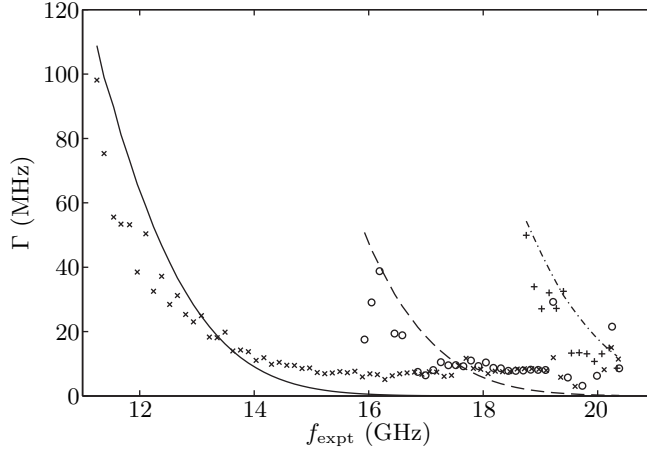


Fig. 3.15: Measured (Γ_{expt}) and calculated (Γ_{calc}) resonance widths for the TE modes of disk B with respect to the measured resonance frequency f_{expt} . The symbols denote the measured widths for different radial quantum numbers (\times : $n_r = 1$; \circ : $n_r = 2$; $+$: $n_r = 3$). The calculated widths are plotted as curves (solid line for $n_r = 1$, dashed for $n_r = 2$, dot-dashed for $n_r = 3$) instead of data points to guide the eye. Reprinted from [61].

The calculated and measured resonance widths for disk B are compared in Fig. 3.15. The former are significantly larger than the latter for lower azimuthal quantum numbers, but the difference is not as large as for disk A in Fig. 3.12. The measured widths saturate at a value of 7 MHz for higher frequencies due to absorption and antenna losses, so that a meaningful comparison with the calculated widths is not possible in this regime. For TM modes, the difference between Γ_{expt} and Γ_{calc} is somewhat smaller. All in all, the calculations overestimate the widths at least for some frequency regimes. This remains true even if the index of refraction is varied. In conclusion, the data for both disks confirms the failure of the n_{eff} -model, and the deviations found for the thinner disk are of the same order of magnitude or even a bit larger.

3.2.3 Results for a microlaser experiment

Another set of measured resonance frequencies was extracted from an experiment reported in [59] with a microlaser made of SiO_x . The microlaser has a radius of

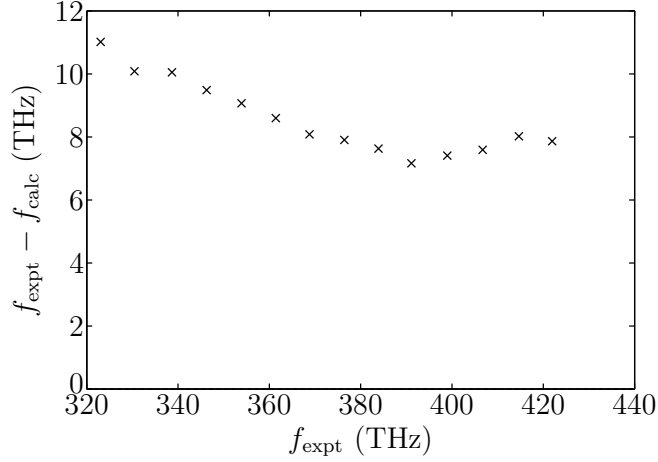


Fig. 3.16: Difference between measured (f_{expt}) and calculated (f_{calc}) resonance frequencies of a microlaser described in [59]. Only TE modes with radial quantum number $n_r = 1$ were observed in the experiment. The range of azimuthal quantum numbers is $m = 29\text{--}42$, and the resonance frequencies correspond to wavelength in the regime of $\lambda = 700\text{--}900$ nm. The deviations are in the order of the resonance spacing.

$R = 4\ \mu\text{m}$, and index of refraction of $n = 1.8$ and a thickness of $b = 135$ nm. The resonance frequencies were extracted graphically from the spectrum in Fig. 2 of [59], which shows several resonances with TE polarization around $\lambda = 800$ nm. This wavelength corresponds to $kR = 31.4$ and $kb = 1.1$. The effective index of refraction at 800 nm is about $n_{\text{eff}} = 1.34$ for TE modes. The differences between the measured resonance frequencies and calculations based on the n_{eff} -model are shown in Fig. 3.16. The observed deviations of ≥ 8 THz are in the order of the resonance spacing, which is 7.6 THz. The magnitude of the deviations with respect to the resonance spacing is thus in the same order as for the microwave resonators treated in the two previous sections. Consequently, this data provides a further independent proof of the inaccuracy of the n_{eff} -model.

3.3 Conclusions

The data presented above shows deviations between the measured resonance frequencies and those computed with the n_{eff} -model which cannot be explained by experimental effects like bending of the resonator or the shift of resonances due to the antennas. They definitely arise from a systematic failure of the model. The ratio between the deviations and the measured resonance frequencies is in the regime of 1–3%, which seems to be fairly accurate. However, the deviations are of the same order of magnitude as the resonance spacing². Therefore, an identification of the measured resonance modes only by comparison with the model calculations is not possible, especially when several series of resonances are visible in the spectrum. Only the additional measurement of the polarization and the intensity distribution enabled an unambiguous identification. Furthermore, the calculated resonance spacings differ from the measured ones. The deviations are quite small, but nonetheless significant (see Fig. 3.9). This can lead to the false impression that the n_{eff} -model yields accurate predictions when only a small frequency range is considered, while a comparison over a wider frequency regime shows the error of the calculations. An example for this effect are the data points marked with \circ (calculations for $n = 1.432$) in Fig. 3.10: only around 13 GHz the deviations are (almost) zero. Another example is Fig. 7 in reference [50], where some resonance frequencies are reproduced precisely by the calculations, but not the spacings to the adjacent resonances. As a consequence, methods to determine the index of refraction of a material sample by comparing the measured resonance spacing to n_{eff} -calculations as proposed in [67] also suffer from a systematic error. In addition, the resonance widths, which are important for applications because they dictate e.g. the lasing thresholds of a microlaser, are not predicted precisely either by the n_{eff} -model. Deviations of up to a factor of two are found for the widths. In conclusion, the n_{eff} -model predicts the correct order of magnitude for resonance frequencies and widths and is useful for a qualitative understanding of flat dielectric resonators, but cannot be used for a detailed and precise understanding or even design of such devices. Above all, the precision of the model calculations is not under control: Figure 3.8 indicates that the devia-

²Resonance spacing means here the frequency spacing between adjacent resonance modes of the same radial quantum number and polarization.

tions might reach a finite value in the semiclassical regime, but this cannot be taken for granted because the index of refraction of the microwave resonators is not known precisely, as Fig. 3.10 demonstrates. Also the role of the aspect ratio R/b is not clear, though the experiments indicate that the deviations are larger for thinner disks respectively larger aspect ratios.

We conjecture that the main reason for the imprecision of the n_{eff} -model are the boundary conditions given by Eq. (2.31), which are just imposed in view of the analogy to a 2d dielectric resonator. For an improvement of the model, a systematic approximation to the correct boundary conditions given by Eq. (2.10) would be needed. The improper choice of boundary conditions might be responsible especially for the large deviations for the resonance widths that were found in the experiments. Furthermore, it is expected that the resonators radiate not only in the plane of the disk, but also in z -direction. The n_{eff} -model, though, does not account for this. Preliminary numerical simulations of the full 3d resonator problem with the commercial program CST MicrowaveStudio [68] have been performed to get a better understanding of the system. These calculations successfully reproduced the measured resonance frequencies of disk A up to 10 GHz, as did other numerical simulations using a finite integration technique [69]. The simulation results showed that the field profiles of the resonance modes in the z -direction deviate from that assumed for the n_{eff} -model [see Eq. (2.21)] close to the boundary of the disk. This leads to the conclusion that the boundary conditions of the n_{eff} -model must be modified, and indicates that diffraction effects due to the edges of the disk are important.

It might be argued that the n_{eff} -model fails for the case of the circular disk because the WGMs are located close to the boundary. This is however not the case since the deviations for modes with higher radial quantum number, which are located further apart from the boundary, are actually even slightly larger. Nonetheless a test of the model with other cavity geometries has not yet been done and might be an interesting future problem.

Summing up, it has been shown that the n_{eff} -model is not capable of precise predictions for the resonance frequencies and widths of flat dielectric cavities. One way of obtaining more precise predictions are 3d numerical calculations with finite integration [69] or finite difference time domain methods (e.g. [59, 60]). The drawback of these methods is that even with improving numerical techniques and

computing power, the computational effort is very large especially for highly excited modes. Therefore, the development of an improved n_{eff} -model would still be worthwhile.

4 Superscars in the dielectric square billiard

Periodic orbits play an important role in the semiclassical theory of quantum systems. Not only is the resonance density of quantum systems related to the POs via so-called trace formulas (see chapter 5), but there also exist wave functions with patterns of high intensity along POs. Such wave functions localized on a certain PO were first discovered by McDonald for unstable, isolated POs in systems with chaotic (or mixed) dynamics [70] and were termed scars by Heller [35]. They have been experimentally observed in metallic microwave billiards [71], and they have also been reported in microlaser experiments [36, 37]. Additionally, e.g. in pseudointegrable quantum billiards [72], scarring wavefunctions were observed which are related to families of (non-isolated) POs. They were named superscars to stress the fact that the scar structure does not vanish in the semiclassical limit [72] as is the case for ordinary scars [73]. This term was also proposed by Heller as the superscars result “from the overlap of many scars” [35]. Superscarred wave functions have been measured in experiments with a closed microwave barrier billiard [65], and the distinct superscar states can be regarded as doorways to the nonscarring resonance states [74]. Furthermore, modes in (dielectric) billiards can be localized on stable POs [75, 76]. For the dielectric spiral even states which look like scars although there is no corresponding classical PO have been found [77–79]. These so-called quasi-scars can be explained by an adjusted ray dynamics incorporating the Goos-Hänchen shift and Fresnel filtering [80].

Superscars commonly appear in pseudointegrable billiards. Examples of such billiards are polygons whose internal angles are all equal to $\alpha_j = \pi m_j/n_j$, where m_j and n_j are co-prime integers and the m_j for at least one corner is greater than 1. Such corners are singular and induce the pseudointegrable dynamics [81]. Examples of such polygonal billiards are the hexagon and the barrier billiard. Polygonal resonator shapes are also of great interest for dielectric cavities, e.g. as add-drop filters [82, 83] or as microlasers [84, 85]. Recently, the existence of superscars in such polygonal dielectric resonators has been proposed [38], including the dielectric square even though the classical square billiard is integrable. This was the motivation for the investigation of the wave functions of a dielectric square resonator presented in this chapter.

4.1 Experimental setup and technique

A square alumina plate with a side length of $a = 300.0$ mm and a thickness of $b = 8.3$ mm was used as resonator. It is made of 99.5% Al_2O_3 (ceramic DeranoxTM995 by Morgan Advanced Ceramics) and has an index of refraction of about $n = 3.16$ [86]. A sketch of the experimental setup is shown in Fig. 4.1: the alumina plate is placed on top of a special foam (Rohacell 31IG by Gaugler und Lutz oHG) with an index of refraction, $n_2 = 1.02$, close to that of air to keep it at a distance of $D = 120$ mm from the optical table. This distance was chosen large enough so that the electromagnetic fields in the alumina resonator are only negligibly perturbed by the optical table (cf. appendix A). Two dipole antennas, a static one below the resonator and a movable one above it, are used to couple RF power into and out of the resonator. The emitting antenna below the alumina plate is connected to a semi-rigid coaxial cable lead through a hole in the foam, and the receiving antenna above is moved around with a positioning unit [66]. The transmission amplitude $S_{ba}(f)$ between two dipole antennas is proportional

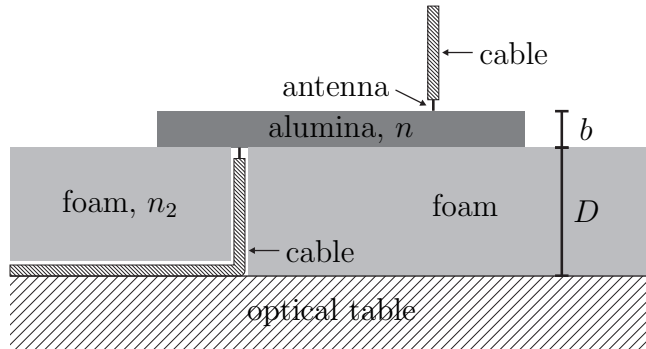


Fig. 4.1: Schematic drawing of the experimental setup (not to scale). The whole setup is placed on an optical table, and the alumina plate used as microwave resonator is separated from the table with a foam of index of refraction close to that of air, $n_2 = 1.02$, and thickness $D = 120$ mm. One static antenna is placed beneath the plate as emitter, and the receiving antenna above the plate can be moved around with a positioning unit. The field distributions in the resonator are measured by scanning it with the moving antenna.

to the electric fields $E_z(\vec{r})$ at their positions $\vec{r}_{a,b}$ [see Eq. (2.34)]. Therefore the near field distribution for a given resonance frequency f_j is obtained by keeping antenna a fixed and scanning the resonator with antenna b . Accordingly we interpret the transmission amplitude with respect to the antenna position \vec{r}_b as the wave function Ψ_j of the j th resonance, i.e.

$$\Psi_j(x, y) \sim S_{ba}(f_j; \vec{r}_b). \quad (4.1)$$

The advantage of this so-called scanning antenna technique is that not only the modulus, but also the phase of the complex wave functions is measured. The drawback is that the relation Eq. (4.1) is only an approximate one since the movable antenna itself is a position-dependent perturbation of the system [87]. It can be shown that S_{ba} is in fact proportional to the Green function of the resonator [88]. Furthermore, perturbations of the measured “wave functions” are found close to the static antenna due to direct transmission between the antennas (see below). The interpretation of $S_{ba}(\vec{r}_b)$ as a wave function fails in the regime of overlapping resonances [88, 89]. Nonetheless, the scanning antenna technique usually yields reliable near field distributions.

4.2 Measured and constructed superscar states

The top graph of Fig. 4.2 shows a frequency spectrum of the square alumina resonator measured with antennas at the positions indicated in the inset. Due to the use of dipole antennas, only TM modes were excited. From 5.5–6.5 GHz, the spectrum features a single family of roughly equidistant resonances with quality factors $Q = 500$ – 1000 . Additional resonances appear at about 6.5 GHz. The broad oscillating background below 5.5 GHz originates from the direct transmission between the antennas. A similar spectrum of equidistant resonances was observed for a square polymer microlaser in [38], and it was conjectured that the measured resonances are superscarred states around the family of the diamond PO shown in the bottom inset. For $n_{\text{eff}} \geq \sqrt{2}$, the diamond orbit is the shortest PO confined by total internal reflection. The effective index of refraction for the alumina resonator, calculated according to Eq. (A.13), is shown in the bottom

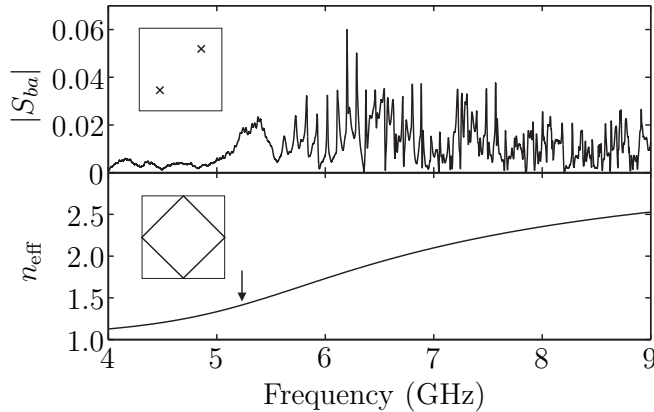


Fig. 4.2: Measured frequency spectrum (top) and effective index of refraction (bottom) of the square alumina resonator. The broad oscillating structure below 5.5 GHz stems from the direct transmission between the antennas. Their positions are indicated by the crosses in the top inset. Above 5.5 GHz, the spectrum shows a series of evenly spaced resonances. The arrow in the bottom graph indicates the frequency $f_{\text{crit}} \approx 5.23$ GHz for which $n_{\text{eff}} = \sqrt{2}$, i.e. the critical angle is equal to the angle of incidence of the diamond PO shown in the bottom inset, 45° .

graph of Fig. 4.2. The arrow marks the frequency $f_{\text{crit}} \approx 5.23$ GHz from which on the diamond PO is confined by TIR. In fact, no resonances are observed below this frequency, which is a first hint that the measured resonances are indeed related to the diamond PO. To confirm this, the associated wave functions were measured.

Two examples of measured field distributions are shown in the left column of Fig. 4.3. There are four symmetry classes of states in the dielectric square according to their symmetry with respect to the diagonals. The states shown in Fig. 4.3 are antisymmetric with respect to both diagonals, denoted as $(--)$ -symmetry. The white circle in Fig. 4.3(a) indicates the position of the static antenna. There a perturbation of the wave pattern due to the direct transmission between the antennas is visible. No such perturbation is observed for the wave function in Fig. 4.3(c). The visibility of this perturbation depends on the width and amplitude of the resonance in the frequency spectrum; the larger the amplitude of the resonance is, the smaller is the relative effect of the direct transmission. Both wave functions show a symmetric and regular pattern, and close to the diagonals,

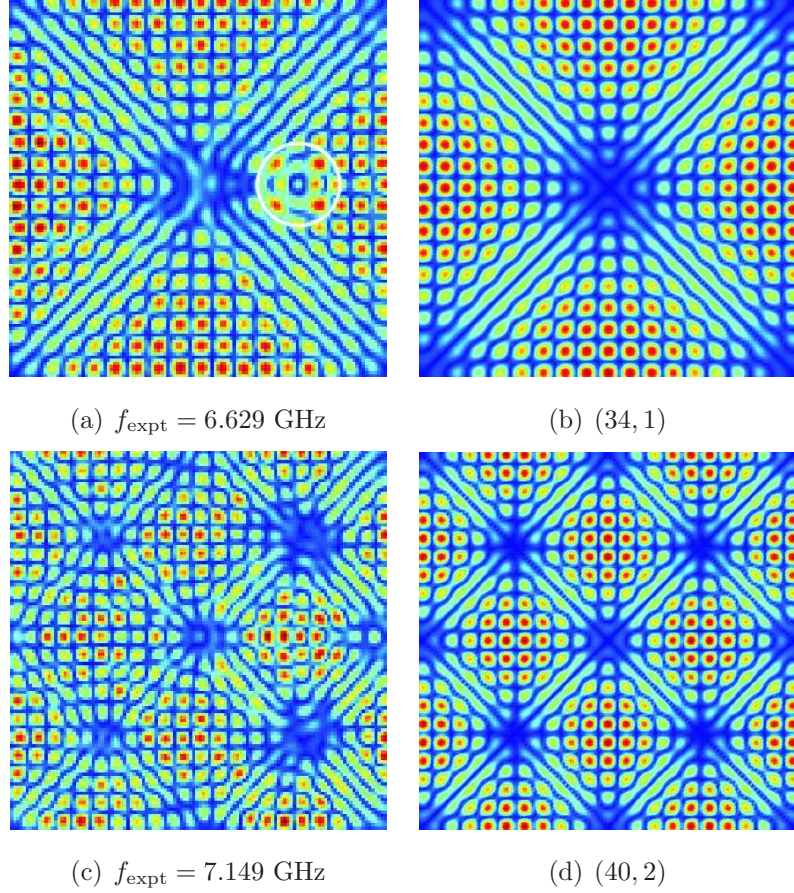


Fig. 4.3: Comparison of the measured near field distributions (left column) with the constructed superscar states (right column). Both resonance states are antisymmetric with respect to the diagonals, i.e. $(--)$ -symmetry. The modulus of the transmission amplitude, $|S_{ba}(x, y)|$, is plotted in false colors, where blue corresponds to low and red to high $|S_{ba}|$. Only the fields inside the resonator are shown. The resonance frequencies of the measured and the quantum numbers (m, p) of the constructed superscar states are indicated. The white circle in (a) marks the perturbation of the wave function due to the static antenna. The agreement between measured and constructed states is very good, the overlap integrals yielding $|c_{34,1}|^2 = 71\%$ (top) and $|c_{40,2}|^2 = 64\%$ (bottom).

the patterns resembles a plane wave traveling along the diamond PO. Indeed, the measured wave functions agree well with the calculated superscar wave functions shown in the right column, whose construction is explained in the following.

The POs in polygonal billiards form continuous families which can be obtained by

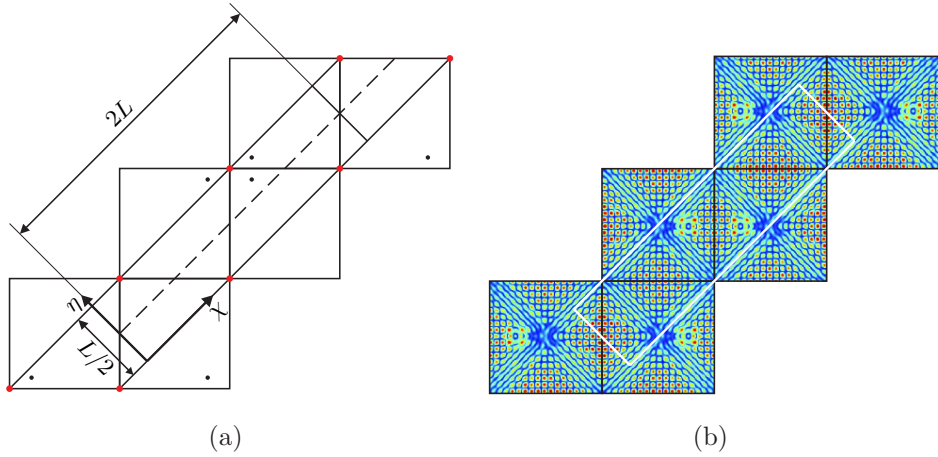


Fig. 4.4: Unfolding procedure. (a) The diamond PO (dashed line) is unfolded by reflecting the square billiard at its sides. The black dots indicate the orientations of the square. The corners of the square (red dots) form the (fictitious) boundaries of the periodic orbit channel. (b) Unfolding of the measured wave function with $(--)$ -symmetry from Fig. 4.3(a). The unfolded wave function obeys Dirichlet boundary conditions at the long sides of the channel (indicated by the white lines), and periodic boundary conditions at the short sides.

unfolding the particle trajectories in the classical billiard as shown in Fig. 4.4(a). There, the diamond PO (dashed line) is unfolded into a straight line by reflecting the billiard at the sides hit by the PO. After four reflections the billiard regains its original orientation (indicated by the black dots in the corners), and the diamond PO closes. The lines connecting the corners of the square (red dots) are parallel to the PO and define a channel, the so-called periodic orbit channel (POC). The associated family of POs comprises all trajectories traveling inside the POC parallel to its sides. In the case of the diamond PO and its family, the length respectively period of the POC is $2L$ and its width is $L/2$, where L is the length of the diagonal of the square. The superscar states are constructed by introducing a wave into the POC with periodic boundary conditions at the short sides (see [38, 65]). Figure 4.4(b) demonstrates that the unfolded $(--)$ -states from Fig. 4.3 obey Dirichlet boundary conditions at the long lateral sides in analogy to the case of closed polygonal billiards. The constructed superscar wave function

is thus

$$\Psi_{m,p}(\chi, \eta) = \Psi_0 \exp \{i[k_\chi \chi + \Phi(\chi)]\} \sin(k_\eta \eta) + \text{c.c.} \quad (4.2)$$

in the coordinates (χ, η) of the POC [see Fig. 4.4(a)] and m and p are the longitudinal and transverse quantum numbers of the superscar. The phase $\Phi(\chi)$ comprises the Fresnel phases accumulated on the reflections at the boundaries of the square. It is

$$\Phi = -2N_{\text{reff}} \delta(45^\circ) \quad (4.3)$$

where N_{reff} is the number of reflections and

$$\delta(\alpha) = \arctan \left(\frac{\sqrt{n_{\text{eff}}^2 \sin^2(\alpha) - 1}}{n_{\text{eff}} \cos(\alpha)} \right) \quad (4.4)$$

is related to the Fresnel reflection coefficient via Eq. (2.26). The wave number k_χ is given as

$$Lk_\chi = \pi m + 4\delta(45^\circ) \quad (4.5)$$

due to the periodic boundary conditions at the short sides, and k_η as

$$\frac{1}{2}Lk_\eta = p\pi \quad (4.6)$$

due to the Dirichlet boundary conditions at the lateral sides of the POC. The resonance frequency of the constructed superscar is thus

$$f_{m,p} = \frac{c}{2\pi n_{\text{eff}}} \sqrt{k_\chi^2 + k_\eta^2}. \quad (4.7)$$

Finally, the wave Eq. (4.2) is folded back into the square to obtain the constructed superscar wave function [66].

The constructed wave functions corresponding to the measured ones in Fig. 4.3 are shown in the right column. The top wave functions corresponds to the transverse quantum number $p = 1$, and the bottom ones to $p = 2$. The constructed wave functions $\Psi_{m,p}(x, y)$ agree very well with the measured ones and reproduce their structure precisely. This is also confirmed by the overlap integrals

$$c_{m,p} = \int_S dx dy S_{ba}(x, y) \Psi_{m,p}^*(x, y) \quad (4.8)$$

which yield $|c_{34,1}|^2 = 71\%$ for the top and $|c_{40,2}|^2 = 64\%$ for the bottom wave functions. The domain of integration S is the interior of the square resonator.

It should be noted though that the overlap integrals are not an exact measure due to possible perturbations near the static antenna and because $S_{ba}(x, y)$ is not exactly equivalent to the wave functions of the resonances as explained in section 4.1. Nonetheless the measured wave functions of $(--)$ -states clearly confirm the existence of superscarred states around the family of the diamond PO in the dielectric square resonator as predicted by [38].

The measured wave functions for two $(+-)$ -states are presented in the left column of Fig. 4.5. The structure looks similar to that of the $(--)$ -states, but it cannot be explained with the superscar construction discussed in the previous paragraphs. This is best seen when unfolding the wave function from Fig. 4.5(c), which is shown in Fig. 4.6. The white lines indicate the POC. Its side designated with a D lies on a nodal line of the measured wave function. Thus there it obeys Dirichlet boundary conditions like in the example in Fig. 4.4(b). The other lateral side (designated with an N), however, does not lie on a nodal line, but rather on a series of maxima of the wave function. This means that it obeys Neumann boundary conditions on that side. This is a surprising finding since superscars with Neumann boundary conditions on a side of the POC do not exist for metallic microwave billiards, and the origin of such wave functions in the dielectric square is not known. Mathematically, superscars with such boundary conditions (denoted as DN-superscars in the following) can be constructed with the same ansatz as before, Eq. (4.2). The only change due to the Neumann boundary conditions is that the transverse quantum number is now a half integer, $p = 1/2, 3/2, 5/2, \dots$. Thus, the wave function in Fig. 4.5(a) can be identified as a DN-superscar with $p = 1/2$, and the one in Fig. 4.5(c) has $p = 3/2$. The corresponding constructed wave functions (right column) agree well with the measured ones, and the overlap integrals yield $|c_{41,1/2}|^2 = 54\%$ (top) and $|c_{45,3/2}|^2 = 55\%$ (bottom), respectively. The agreement is not as good as for the superscars with Dirichlet boundary conditions on both sides of the POC (designated DD-superscars). This can also be seen when investigating the structure of the wave functions more closely: the white lines in Fig. 4.5(d) indicate the major nodal lines of the constructed DN-superscar. A comparison with the measured wave function shows these white lines do not agree precisely with the major nodal lines of the measured wave function. This is in contrast to the case of the DD-superscars, where the major nodal lines of constructed and measured wave functions agree perfectly. It indi-

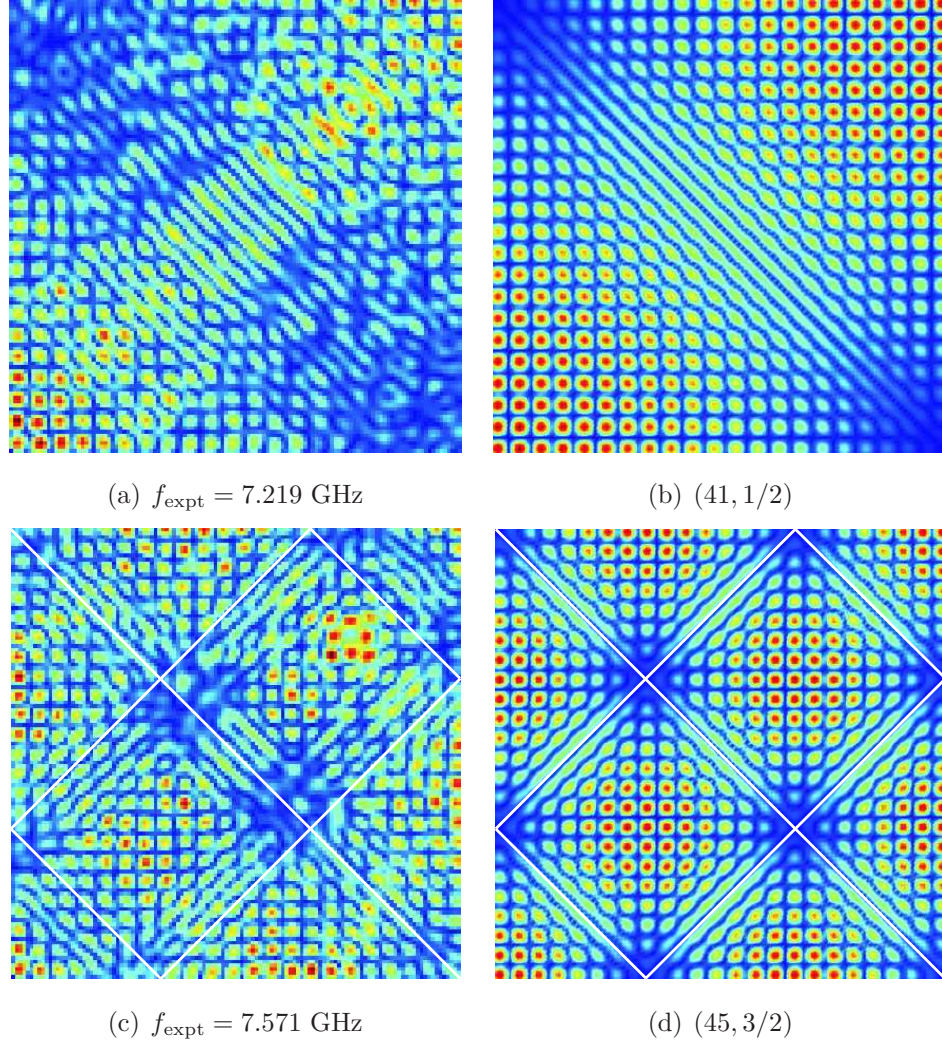


Fig. 4.5: Comparison of the measured near field distributions (left column) with the corresponding constructed superscar states (right column) for two $(+-)$ -symmetry states. The resonance frequencies of the measured and the quantum numbers (m, p) of the constructed superscar states are indicated. The agreement between measured and constructed wave functions is good with $|c_{41,1/2}|^2 = 54\%$ (top) and $|c_{45,3/2}|^2 = 55\%$ (bottom). The white lines in the bottom graphs indicate the major nodal lines of the constructed superscar with $p = 3/2$. A comparison with the measured wave function in (c) shows that there is actually a small deviation in the structure of the measured and the constructed wave function.

cates that there is some additional effect that is not accounted for by the simple DN-superscar model used here.

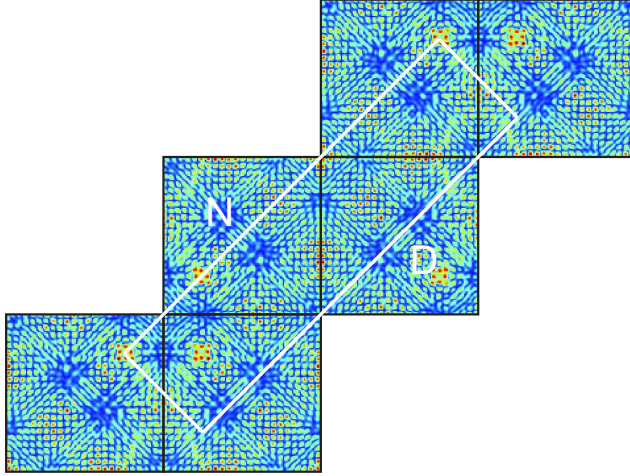


Fig. 4.6: Unfolding of the measured $(+-)$ -symmetry state from Fig. 4.5(c). The unfolding shows that the field distribution obeys Dirichlet boundary conditions (D) on one, but Neumann boundary conditions (N) on the other lateral side of the periodic orbit channel (indicated by the white lines).

Last but not least, we investigate wave functions of states with $(++)$ -symmetry in Fig. 4.7. Due to this symmetry, the antenna was placed in the middle of the square, leading to a perturbation there of the measured wave function as visible in Fig. 4.7(a). The unfolding of the wave function (not shown here) demonstrates that it obeys Neumann boundary conditions on both lateral sides of the POC. A corresponding superscar (so-called NN-superscar) can be constructed by replacing the term $\sin(k_\eta\eta)$ in Eq. (4.2) by $\cos(k_\eta\eta)$. The transverse quantum number is then an integer, $p = 1, 2, \dots$. Such a constructed NN-superscar is shown in Fig. 4.7(b), showing good agreement with an overlap of $|c_{44,2}|^2 = 49\%$. Nonetheless, a comparison of the locations of the major nodal lines of the constructed superscar (indicated by the white lines) with those of the measured one shows small discrepancies like for the case of the DN-superscars.

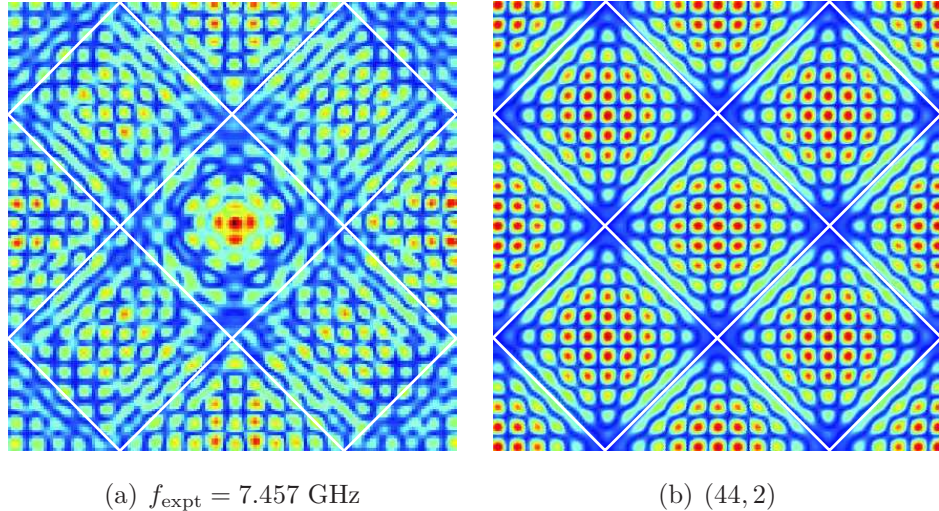


Fig. 4.7: Comparison of the measured near field distribution of a $(++)$ -state (left) with the corresponding constructed superscar state (right). The resonance frequency of the measured and the quantum numbers (m, p) of the constructed superscar state are indicated. The overlap integral yields $|c_{44,2}|^2 = 49\%$. The white lines indicate the major nodal lines of the constructed wave function. The comparison of those with the measured wave function shows up small discrepancies between the structures of the measured and constructed wave function.

4.3 Summary and outlook

In summary, the measured wave functions of resonance states with $(--)$ -symmetry confirm the existence of superscars based on the diamond PO as predicted by [38], and the constructed superscar wave functions with Dirichlet boundary conditions on the lateral sides of the POC describe the measured ones very well. These boundary conditions were conjectured in analogy to the case of metallic polygonal microwave billiards: it has been shown in [72, 90] for the metallic case that a wave in the POC, which is scattered at the infinite periodic array of corners forming the sides of the POC, effectively obeys Dirichlet boundary conditions in the semiclassical limit $k \rightarrow \infty$. A similar effect is expected for the scattering at dielectric corners, but this has not yet been shown mathematically. The investigation of $(+-)$ - and $(++)$ -symmetry states, however, showed wave functions which cannot be described by this standard superscar model, having Neumann

boundary conditions on one or both sides of the POC instead. Superscar states with such boundary conditions are easily constructed, but the mechanism leading to their formation is unknown. Moreover such states do not appear in metallic polygonal billiards. Thus, apparently the scattering at dielectric corners is much more complicated than at metallic ones and not yet understood. This suggests further investigations concerning dielectric corners and polygonal dielectric resonators since the existence of superscars has been proposed also for other cavities of this type, and they are used in a variety of applications [82–85].

It should furthermore be noted that numerical investigations of dielectric ellipse and rectangle resonators also yielded wave functions localized on POs [91]. Further investigations indicated that the formation of such wave functions is related to avoided resonance crossings where different modes hybridize to form these localized states [76]. It was conjectured that this happens for all dielectric resonators with integrable classical counterpart, which might provide an alternative explanation for the localized wave functions presented in this chapter.

The overlaps $|c_{m,p}|^2$ between the measured wave functions and the constructed superscars depend on the individual mode and are statistically distributed. This distribution has been investigated in [74] for the case of the barrier billiard, and it was shown that the idealized superscar states can be interpreted as so-called doorway states interacting with the complex resonance states of the real cavity. This doorway mechanism is well known e.g. from the giant resonances of nuclei [92]. Indications for such an interaction have also been found for a 2d dielectric square billiard (see section 5.5). Further investigations of the interaction effect and the distribution of the overlaps are planned in order to test recent theoretical predictions [93–95].

5 Trace formula for two-dimensional dielectric cavities

Trace formulas are a paradigm of semiclassical physics: they relate the level density of a quantum (or more general, wave-dynamical) system to the periodic orbits (POs) of the corresponding classical system, i.e. to trajectories that retrace themselves after a finite time. Trace formulas were first introduced by Gutzwiller in 1970 for regular [10] and chaotic [11] quantum systems and are applied not only in atomic and nuclear physics [96, 97], but also to other wave-dynamical systems like electromagnetic [98–100] or acoustic [101, 102] resonators. Recently, Bogomolny *et al.* proposed a trace formula for dielectric resonators [39], which was developed to explain the occurrence of peaks at the lengths of the POs in the Fourier transform (FT) of the spectra of flat polymer microlasers [38]. Similar findings have recently been reported for vertical cavity surface emitting lasers (VCSELs) [103]. In the following, we will present a detailed test of this trace formula with three different dielectric microwave resonators, a circular one made of Teflon ($n \approx 1.4$) and two square shaped ones made of Teflon and alumina ($n \approx 3$), respectively. The main focus here will be on the incompleteness of the measured spectra: Only the resonances with the lowest radiation losses are actually discernible in the measured frequency spectra. Therefore, the relation between the most long-lived resonances and certain POs can be investigated. The main results have been published in [104].

5.1 Resonance density and trace formula

The level density of a closed quantum system or microwave billiard equals

$$\rho(k) = \sum_j \delta(k - k_j). \quad (5.1)$$

The analogous quantity for a dielectric resonator is the resonance density (RD), which equals [39]

$$\rho(k) = -\frac{1}{\pi} \sum_j \frac{\text{Im}(k_j)}{[k - \text{Re}(k_j)]^2 + [\text{Im}(k_j)]^2} \quad (5.2)$$

since the quasi-bound modes or resonances are characterized by a complex k_j (see section 2.5). The RD can be decomposed into a smooth and a fluctuating part,

$$\rho(k) = \rho_{\text{Weyl}}(k) + \rho_{\text{fluc}}(k), \quad (5.3)$$

where the smooth part is also known as Weyl term. The Weyl term is only related to the gross geometrical parameters, i.e. the area A and circumference U , of the billiard, while the fluctuating part is connected to the POs. For a 2d dielectric cavity [39],

$$\rho_{\text{Weyl}}(k) = \frac{An^2}{2\pi}k + \tilde{r}(n)\frac{U}{4\pi} \quad (5.4)$$

where $\tilde{r}(n)$ is related to the dielectric boundary conditions with n again denoting the index of refraction. It is given by

$$\tilde{r}(n) = 1 + \frac{n^2}{\pi} \int_{-\infty}^{+\infty} \frac{dt}{t^2 + n^2} \tilde{R}(t) - \frac{1}{\pi} \int_{-\infty}^{+\infty} \frac{dt}{t^2 + 1} \tilde{R}(t) \quad (5.5)$$

where for TM modes

$$\tilde{R}(t) = \frac{\sqrt{t^2 + n^2} - \sqrt{t^2 + 1}}{\sqrt{t^2 + n^2} + \sqrt{t^2 + 1}}. \quad (5.6)$$

For a billiard with regular classical dynamics, the fluctuating part of the RD is [39]

$$\rho_{\text{fluc}}^{\text{scl}}(k) = \sum_{\text{po}} \left(\sqrt{n/\pi} \right)^3 B_{\text{po}} |R_{\text{po}}| \sqrt{k} e^{i(nk\ell_{\text{po}} + \varphi_{\text{po}})} + \text{c.c.} \quad (5.7)$$

Here, $B_{\text{po}} \propto A_{\text{po}}/\sqrt{\ell_{\text{po}}}$ is the amplitude of each PO contribution, where A_{po} is the area of the billiard in configuration space covered by the family of the POs with length ℓ_{po} . The factor R_{po} is the product of all Fresnel reflection coefficients for the reflections at the boundary, and φ_{po} includes phases picked up along the PO. These include the phase changes at reflections, i.e. $\arg(R_{\text{po}})$, and phases due to so-called conjugate points, e.g. caustics [12]. The details of B_{po} , R_{po} and φ_{po} for the dielectric circle and square billiards are given in the corresponding sections below. Note that for $n = 1$ and $R_{\text{po}} = (-1)^q$ with q denoting the number of reflections at the boundary in Eq. (5.7) and $\tilde{r} = -1$ in Eq. (5.4), the trace formula for a closed regular quantum billiard with Dirichlet boundary conditions is recovered. Thus the only significant modifications for dielectric resonators are the n -dependent factors accounting for the larger optical length or volume and the Fresnel reflection coefficients due to the open boundary conditions. In the limit

$k \rightarrow \infty$, the RD given by Eq. (5.2) should be well described by the semiclassical approximation $\rho_{\text{Weyl}}(k) + \rho_{\text{fluc}}^{\text{scl}}(k)$. For a comparison of the experimental $\rho(k)$ with the trace formula, it is useful to look at the FT of its fluctuating part,

$$\begin{aligned}\tilde{\rho}(\ell) &= \int_{k_{\min}}^{k_{\max}} dk [\rho(k) - \rho_{\text{Weyl}}(k)] e^{-ikn\ell} \\ &= \sum_j e^{-ik_j n\ell} - \text{FT}\{\rho_{\text{Weyl}}(k)\},\end{aligned}\tag{5.8}$$

where the summation runs over all resonances with $k_{\min} \leq \text{Re}(k_j) \leq k_{\max}$. The corresponding semiclassical expression is given as

$$\tilde{\rho}_{\text{scl}}(\ell) = \int_{k_{\min}}^{k_{\max}} dk \rho_{\text{fluc}}^{\text{scl}}(k) e^{-ikn\ell}.\tag{5.9}$$

The value ℓ has the meaning of a geometrical length, and $|\tilde{\rho}(\ell)|$ is called the length spectrum. Due to the terms $e^{ikn\ell_{\text{po}}}$ in the trace formula Eq. (5.7) it is expected that the length spectrum shows peaks at the lengths of the POs. It should be noted that long-lived resonances yield larger contributions to the length spectrum than short-lived ones due to the factor $\exp\{-n\ell|\text{Im}(k_j)|\}$ in Eq. (5.8).

5.2 Experimental setup

To construct a quasi-2d dielectric resonator, the dielectric plates are placed between two copper plates as sketched in Fig. 2.1(b). This is shown in more detail in Fig. 5.1. Two dipole antennas are used to excite TM modes and measure the transmission spectra between them. The antennas are placed next to the sidewalls of the resonators as shown in Fig. 5.1(a) so that they couple to the evanescent fields of the resonances. Three different resonators were investigated, and their details are given in the corresponding sections. In the case of the circular resonator, the antennas were put opposite to each other due to symmetry reasons because then one mode of each degenerate doublet is excited with equal amplitude for all doublets. In the case of the square resonators, the antennas were deliberately placed off any symmetry axis so that modes of all symmetry classes

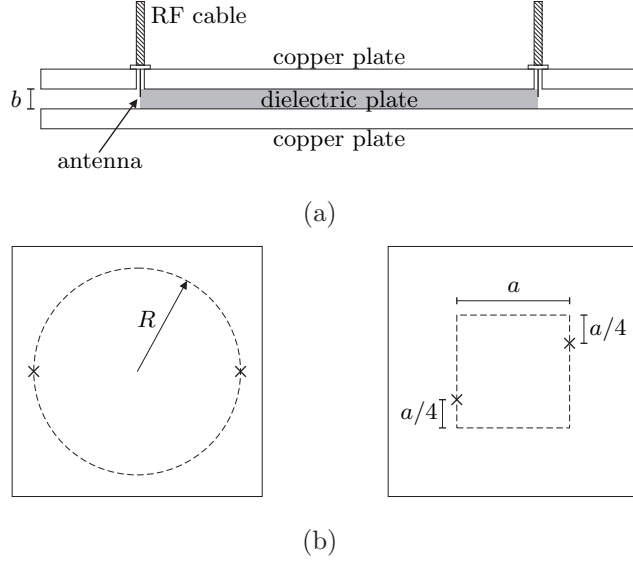


Fig. 5.1: Schematic picture of the experimental setup (not to scale). (a) Side view: the dielectric plate is placed between two copper plates. Two dipole antennas entering the resonator through small holes in the top plate are placed next to the sidewalls of the dielectric plate. (b) Top view: The solid lines indicate the contour of the copper plates, the dashed lines that of the dielectric plates, a circle with radius R or a square with side length a . The crosses indicate the positions of the antennas. Adapted from [104].

are excited with roughly equal amplitude [see Eq. (2.18)]. The influence of waves reflected at the edges of the copper plates is negligible. The indices of refraction n of the dielectric plates were deduced from the length spectra: The positions of the peaks corresponding to POs in the length spectrum depend sensitively on the value of n used in the FT Eq. (5.8). Therefore, n was fitted such that the positions of the peaks and the lengths of the POs agree. The n determined this way slightly deviates from the real index of refraction. This is attributed to air gaps between the dielectric disk and the copper plates. Thus, the fitted n is actually the effective index of refraction which corresponds to the in-plane phase velocity c/n_{eff} of the waves in the combination of the dielectric plate with the air gap (see also section 2.7). It is shown in appendix A.2 that

$$n_{\text{eff}} = \frac{n}{1 + \frac{d}{2b}(n^2 - 1)} \quad (5.10)$$

for small air gap sizes d . Thus, even an air gap smaller than 0.1 mm, i.e. 2% of the thickness b of the dielectric plate, leads to a deviation from the real n of a few percents. This air gap effect is well known and can hardly be avoided [105]. In order to minimize the air gap, several measures were taken: First, the whole setup was put on a flat optical table so that bending of the different components cannot induce additional gaps. Second, the upper plate was weighted with lead bricks to minimize remaining air gaps. Care was taken that the additional weight did not perceptibly deform the elastic Teflon plates. Then there still are air gaps, but the frequency spectra are reproducible with sufficient accuracy.

5.3 Circular Teflon resonator

The circular Teflon resonator (called Teflon circle in the following) is the same one as disk B from chapter 3. It has a radius of $R = 274.9$ mm and a thickness of $b = 5.0$ mm. The index of refraction which was determined via the positions of the peaks in the length spectrum is $n = 1.419 \pm 0.001$, which corresponds to a critical angle for TIR $\alpha_{\text{crit}} = 44.8^\circ$. This value of n is smaller than the one measured independently, 1.439. The error $\Delta n = 0.001$ only accounts for the accuracy of the fitting procedure, but not for the systematic error due to the air gaps. A frequency spectrum measured with two dipole antennas on opposite sides of the disk [see Fig. 5.1(b)] is shown in Fig. 5.2. A frequency of 10 GHz corresponds to $kR = 57.6$, and the quality factors of the resonances are in the regime of $Q = 1000\text{--}5000$. The spectrum consists of several families of modes with different radial quantum numbers n_r . It is similar to that shown in Fig. 3.4 except that there are no TE modes below $f_{2d} \gtrsim 20.5$ GHz. Only modes with low n_r are discernible in the measured spectrum since they have the lowest radiation losses as explained in section 2.6. The bars above the graph indicate the frequency regimes in which modes with different n_r can be observed experimentally. The trajectories corresponding to two modes with $n_r = 1$ and 2 are shown as insets, where the angle of incidence α with respect to the surface normal has been computed via Eq. (2.20). All observed resonance modes are like these of the whispering gallery type and thus correspond to trajectories with high α and are located close to the

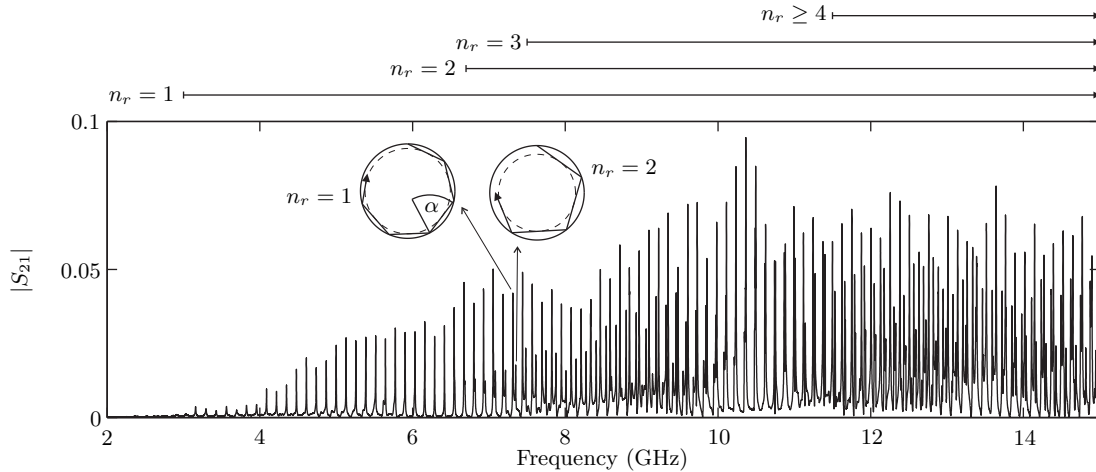


Fig. 5.2: Frequency spectrum of the Teflon circle. The classical trajectories associated with two resonances with radial quantum numbers $n_r = 1$ and 2 are shown as insets. There, α is the angle of incidence with respect to the surface normal of the trajectories and the dashed line is their caustic. The bars above the graph indicate the frequency regimes in which modes with certain radial quantum numbers are observed experimentally. All modes are of TM type due to the two copper plates. Reprinted from [104].

boundary of the disk like in chapter 3. The comparison between the two trajectories shown in Fig. 5.2 shows that modes with higher n_r (at a given frequency) correspond to trajectories with smaller α and thus smaller caustic (the dashed line in the insets). Figure 5.3 shows the integrated resonance density $N(f)$, which is the number of resonances below a certain frequency f . All resonances observed in the measured spectrum (solid line) were counted twice since the modes with $m > 0$ are doubly degenerate. Only modes below $f_{2d} \approx 20.5$ GHz were taken into account. The dashed line is Weyl's law obtained by integrating Eq. (5.4). The comparison of the experimental $N(f)$ with Weyl's law shows that the long-lived, observable resonance modes are only a small part (about 10%) of the spectrum. The question is therefore what effect the huge amount of missing modes has on the experimental length spectrum, which is shown as solid line in Fig. 5.4. It was obtained from the list of measured resonance frequencies and widths (including the double degeneracy of the modes) via Eq. (5.8). The length spectrum shown as dashed line was obtained from a complete spectrum calculated via Eq. (2.19),

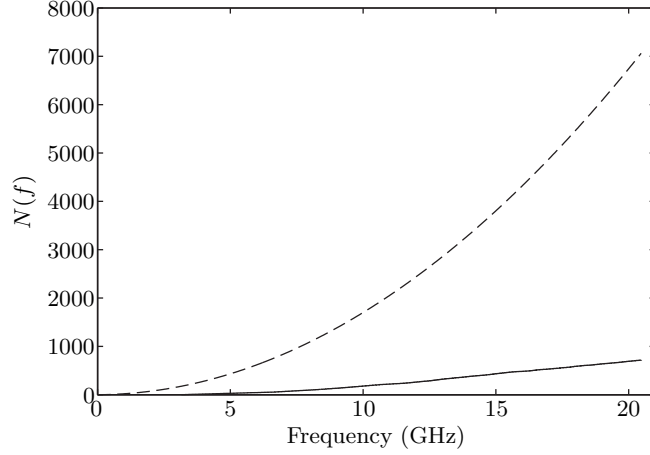


Fig. 5.3: The integrated resonance density $N(f)$ for the Teflon circle. The solid line is $N(f)$ for the measured spectrum shown in Fig. 5.2, and the dashed line is computed from Weyl's law. Altogether 716 resonances were identified in the spectrum up to 20.5 GHz, which is only 10% of all resonances. Reprinted from [104].

and the dotted line shows the FT of the trace formula, $\tilde{\rho}_{\text{scl}}(\ell)$ from Eq. (5.9). All FTs in this chapter were performed with the Welch function as window function in order to smooth the resulting curves [106]. The lengths of the POs and that of the circumference, $2\pi R$, are indicated by arrows. The POs in the circle billiard have the shapes of polygons and stars. They are characterized by their period, q , which is the number of reflections at the boundary, and the rotation number η , which is the number of turns around the center. So the PO with $(q, \eta) = (4, 1)$ is a square, while the $(5, 2)$ -orbit is a pentagram. The POs relevant for the lengths considered in Fig. 5.4 are shown as insets. Their lengths are

$$\ell_{\text{po}}(q, \eta) = 2Rq \sin(\eta\pi/q), \quad (5.11)$$

and the amplitudes and phases appearing in the trace formula Eq. (5.7) are

$$B_{\text{po}} = \frac{A_{\text{po}}}{\sqrt{\ell_{\text{po}}}} \sqrt{2} f_{\text{po}} \quad \text{with} \quad f_{\text{po}} = \begin{cases} 1 & : \quad q = 2\eta \\ 2 & : \quad \text{otherwise} \end{cases} \quad (5.12)$$

and

$$\varphi_{\text{po}} = \frac{\pi}{4} - q \frac{\pi}{2} + q \arg[r(\alpha_{\text{po}})]. \quad (5.13)$$

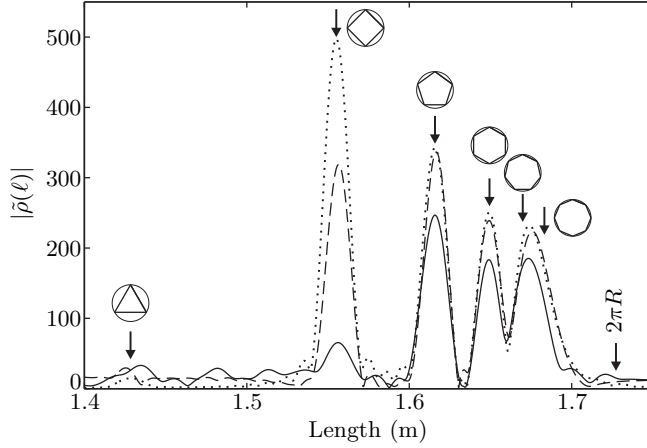


Fig. 5.4: Length spectrum for the Teflon circle. The modulus of $\tilde{\rho}(\ell)$ is plotted with respect to the geometrical length. The full line results from the measured spectrum, the dashed line from a complete calculated spectrum, and the dotted line is the semiclassical expression $|\tilde{\rho}_{\text{scl}}(\ell)|$. The arrows indicate the lengths of the depicted polygonal POs and of the circumference $2\pi R$ of the circle. The semiclassical expression (dotted line) and the calculated length spectrum (dashed line) agree well except for the square orbit. The experimental length spectrum has smaller peak amplitudes than the calculated one, but the deviations are smaller for the higher-order polygons. Reprinted from [104].

The area covered by the family of the (q, η) -orbits is $A_{\text{po}} = \pi R^2 \sin^2(\eta\pi/q)$, and $r(\alpha)$ is the Fresnel reflection coefficient for angle of incidence α with respect to the surface normal and electric field perpendicular to the plane of incidence (TM polarization). The angle of incidence of a PO is $\alpha_{\text{po}} = \pi/2 - \eta\pi/q$. For the case $r = -1$ in Eq. (5.7), the amplitudes and phases for a circle billiard with Dirichlet boundary conditions are recovered (cf. [12, 107]). For $q/\eta \rightarrow \infty$ with η fixed, the lengths of the POs converge to η times the circumference, but contribute only negligibly since $B_{\text{po}} \propto \sin^{3/2}(\eta\pi/q)$. Therefore, only the POs up to the octagon are indicated in Fig. 5.4. The calculated length spectrum (dashed line) and the FT of the trace formula (dotted line) agree very well except for the case of the square orbit, that is $\alpha_{\text{po}} = 45^\circ$. The trace formula generally overestimates the amplitudes of POs with an angle of incidence close to α_{crit} because for such orbits the stationary phase approximation used to derive Eq. (5.7) is only valid

in the strict semiclassical limit $k \rightarrow \infty$. For large but finite k , further corrections to the term R_{po} (the product of the reflection coefficients) must be taken into account [39], however a useful approximation has not yet been found. The use of modified Fresnel coefficients for curved interfaces [108], for example, does not yield more accurate results. Note that for POs like the triangle orbit which are not confined by TIR there are no discernible peaks as expected from the trace formula. The experimental length spectrum (solid line) also features peaks at the lengths of the POs, in agreement with the calculated and the semiclassical length spectrum. However, the peak amplitudes are significantly smaller, which was to be expected due to the many missing resonances. Still, some peaks in the experimental length spectrum are as large as 80% of the calculated ones. Thus, apparently the 10% most long-lived resonances suffice to reproduce the greater part of the peaks expected semiclassically. The reason for this is that the most long-lived modes give the dominant contributions to Eq. (5.8). Interestingly, the agreement between experimental and calculated length spectra is better for the higher order polygons like hexagon, heptagon and octagon, and worst for pentagon and the square orbit. The reason for this might be that the measured resonances are all WGMs, which correspond to trajectories close to the boundary like the high-order polygons (cf. the insets in Fig. 5.2). The spectrum was divided into the different subspectra with radial quantum numbers $n_r = 1, 2, 3$ and $n_r \geq 4$ in order to investigate the relation between the different resonance families and the different POs. The quantum numbers of the modes were identified by following the different series along the frequency spectrum and comparing them with the calculated spectrum. As a start, only the modes with $n_r = 1$ are considered, which form a series of almost (but not exactly) equidistant resonances. This is an interesting test case because spectra consisting of a single equidistant resonance family are often encountered in microlaser and -cavity experiments (e.g. [38, 109]). In Fig. 5.5, the length spectra resulting from modes with $n_r = 1$ up to a certain frequency f_{max} are shown. The solid line corresponds to modes up to $f_{\text{max}} = 20.5$ GHz, the dashed line up to $f_{\text{max}} = 15$ GHz and the dotted line up to $f_{\text{max}} = 10$ GHz. Each curve has only one peak at a length similar to the lengths of the polygon orbits, but there is no direct correspondence between the peak position and any particular PO. Instead, the position of the peak only depends on f_{max} . This can be explained by the structure of the subspectrum with $n_r = 1$

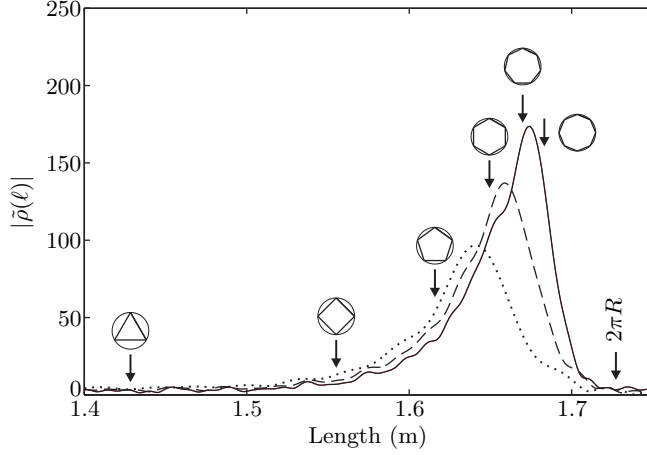


Fig. 5.5: Length spectrum for a single resonance family. Only measured modes with radial quantum number $n_r = 1$ were considered and only up to a certain frequency f_{\max} (solid line: 20.5 GHz; dashed line: 15 GHz; dotted line: 10 GHz). The arrows indicate the lengths of the POs shown as insets and of the circumference $2\pi R$ of the circle. Apparently, the position of the maximum of $|\tilde{\rho}(\ell)|$ only depends on the frequency f_{\max} , but is not related to any particular PO. Reprinted from [104].

and the fact that an equidistant series of resonances with spacing Δf results in a peak at a position $\ell \propto 1/\Delta f$ in the length spectrum. The wave numbers of the TM modes with low n_r of a dielectric circle can be approximated with $O(m^{-1/3})$ -precision as [110]

$$\operatorname{Re}(k_{m,n_r}) = \frac{m}{nR} + \frac{x_{n_r}}{nR} \left(\frac{m}{2}\right)^{1/3} - \frac{1}{R\sqrt{n^2-1}}, \quad (5.14)$$

with x_j being the modulus of the j th root of the Airy function $\operatorname{Ai}(x)$. The resonance spacing Δk between modes of the same n_r can thus be estimated as

$$\Delta k = \frac{1}{nR} + \frac{x_{n_r}}{6nR} \left(\frac{m}{2}\right)^{-2/3}. \quad (5.15)$$

Here, the resonance spacing is almost constant, but with a small m - (and thus frequency-) dependent additional term. In accordance, the length spectra in Fig. 5.5 show only one peak whose position is determined by the minimal resonance spacing $(\Delta k)_{\min}$, i.e. the maximal frequency considered, f_{\max} . This applies also to the length spectra shown in Fig. 5.6(a). A more detailed mathematical

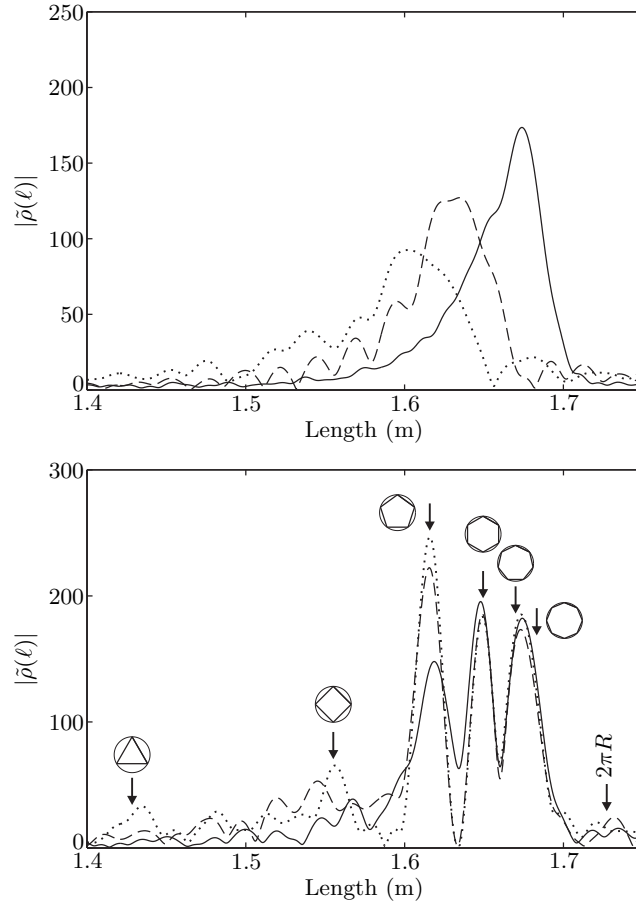


Fig. 5.6: Length spectra for different resonance families. (a) Only one radial quantum number taken into account each (solid line: $n_r = 1$; dashed line: $n_r = 2$; dotted line: $n_r = 3$). As in Fig. 5.5, the length spectra have a single peak each, whose position is not related to any PO. (b) Several families combined. The solid line is the length spectrum for the families with radial quantum numbers $n_r = 1$ and 2 combined, the dashed line is for $n_r = 1, 2$, and 3 combined, and the dotted line is for all resonances (identical with the solid line in Fig. 5.4). Reprinted from [104].

explanation is given in appendix B.1. The example Fig. 5.5 shows that caution is necessary when trying to relate a single family of resonances to a certain PO, and it explains a similar effect found for the case of a circular microlaser, see [38].

In conclusion, a single resonance family by itself has no clear relation to any PO. Therefore, the length spectra resulting from several resonance families are

investigated in Fig. 5.6(b). Indeed, already the combination of modes with $n_r = 1$ and 2 (solid line) gives rise to peaks whose positions coincide with the lengths of the POs. This is due to an interference effect between the two families (see appendix B.2). Moreover, the peaks with the highest amplitudes are those for the high-order polygons (hexagon to octagon). This length regime is the one where the corresponding single-family length spectra [solid and dashed lines in Fig. 5.6(a)] have their maxima. The combination of $n_r = 1, 2$ and 3 yields the dashed line in Fig. 5.6(b). The comparison with the $n_r = 1, 2$ case in Fig. 5.6(b) shows that the resonances with $n_r = 3$ mainly contribute in the length regime where the corresponding single-family length spectrum [dotted line in Fig. 5.6(a)] has its maximum. The few remaining resonances with $n_r \geq 4$, included to obtain the dotted length spectrum in Fig. 5.6(b), contribute mainly to the pentagon and square orbits. We can conclude that there indeed is a connection between the long-lived WGMs and the higher-order polygons: the different families of WGMs do not contribute to a single PO in the length spectrum, but to the higher-order polygons as a whole. In addition this explains why the peak amplitudes in the length spectrum are larger for the high-order polygons: the resonance states with the longest lifetimes of the circular dielectric resonator correspond to the most confined POs of the classical dielectric billiard. These results were also confirmed with a complete, calculated spectrum. A further effect which slightly decreases the peak amplitudes of the experimental length spectrum is the enlargement of the measured resonance widths due to absorption, Ohmic losses and the antennas, but these effects are of little importance here due to the generally large quality factors.

5.4 Square Teflon resonator

The square Teflon resonator (called the Teflon square in the following) has a side length of $a = 300$ mm, a thickness of $b = 5.1$ mm and an index of refraction of $n = 1.430 \pm 0.001$, which corresponds to $\alpha_{\text{crit}} = 44.4^\circ$. Figure 5.7 shows its frequency spectrum. A frequency of 10 GHz corresponds to $ka = 62.9$. The spectrum shows only a single family of broad equidistant resonances with quality

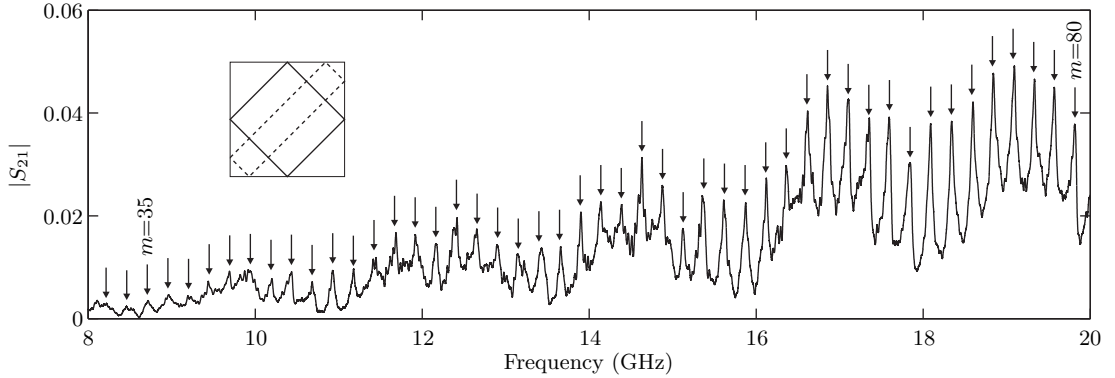


Fig. 5.7: Frequency spectrum of the Teflon square. The series of equidistant resonances atop the slowly oscillating background consists of superscarred states localized on the family of the diamond PO (shown as inset). The arrows indicate the computed resonance frequencies of the superscarred states according to Eq. (5.17). The quantum numbers $m = 35$ and $m = 80$ are indicated for two examples. Reprinted from [104].

factors $Q = 100\text{--}500$. The slowly oscillating background stems from the direct transmission between the antennas. A similar spectrum was observed for a polymer microlaser ($n_{\text{eff}} \approx 1.5$) in [38], and it was conjectured that the resonance modes of the dielectric square resonator are superscarred states localized on the family of the diamond PO (see inset of Fig. 5.7). The existence of superscarred states was confirmed experimentally in section 4 for a different setup with a dielectric square resonator. A simple quantization for a superscar localized on the diamond PO is

$$\exp(ink2L)r^4(45^\circ) = 1, \quad (5.16)$$

where $2L$ is the length of the diamond PO with $L = \sqrt{2}a$ being the length of the diagonal. This leads to

$$nL \operatorname{Re}(k_m) = \pi m + 2i \ln[r(45^\circ)] = \pi m + 4\delta(45^\circ), \quad (5.17)$$

where m is the longitudinal quantum number of the superscar and the phase $\delta(45^\circ) = \arctan(\sqrt{1 - 2/n^2})$ [cf. Eq. (4.4)] is related to the Fresnel reflection coefficient as in Eq. (2.26) via $r = \exp(-2i\delta)$. This approximation for the resonance frequencies of the superscars is a simplification of Eqs. (4.5) to (4.7) in the limit $m \gg p$, where p denotes the transverse excitation of the superscar. It is only

correct up to $O(1/m)$ (see [38]), but still quite accurate in the case considered here: The resonance frequencies computed according to Eq. (5.17) are indicated in Fig. 5.7 by the arrows and agree very well with the resonance positions in the measured spectrum. Thus the experimentally observed resonances are apparently superscattered states localized around the family of the diamond orbit with longitudinal quantum numbers $m = 35\text{--}80$ and first transverse excitation. The low quality factors, which are an order of magnitude smaller than for the Teflon circle, result from the fact that the angle of incidence of the diamond PO, $\alpha_{\text{po}} = 45^\circ$, is very close to the critical angle, which implies large radiation losses. Due to these, only 49 resonances were observed up to 20.5 GHz, which is only 2% of the approximately 2220 modes expected according to Weyl's law.

The length spectrum of the Teflon square is shown in Fig. 5.8. The experimental length spectrum is the solid line in the top graph, and the trace formula prediction is shown in the bottom graph with a different scale. The arrows indicate the

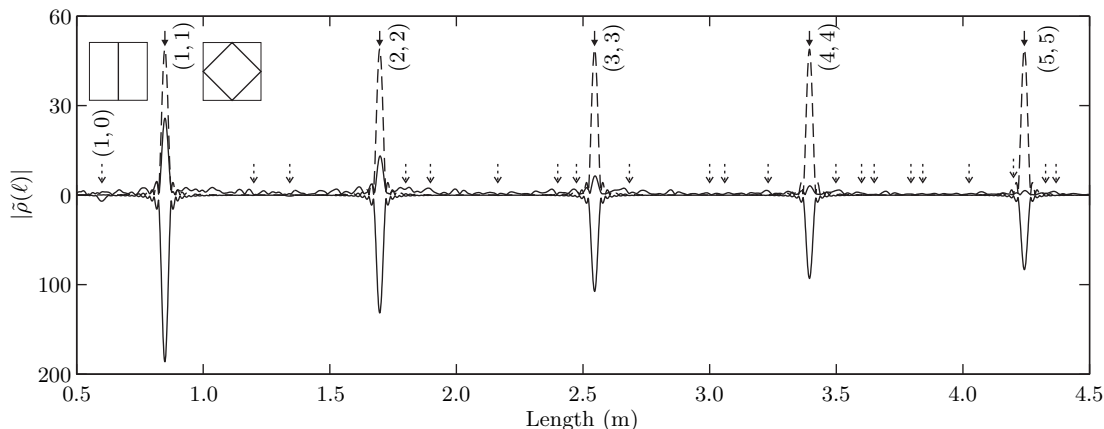


Fig. 5.8: Length spectrum for the Teflon square. The top graph shows the experimental length spectrum (solid line) and the length spectrum for a single family of superscars according to Eq. (5.22) (dashed line). The bottom graph shows the FT of the trace formula. Note the different scales of top and bottom graph. The arrows indicate the lengths of the POs (dashed arrows for POs not confined by TIR) labeled with (n_x, n_y) . The Fabry-Perot orbit (left inset) and the diamond orbit (right inset) are shown as examples. The experimental length spectrum features only the diamond orbit and its repetitions. Reprinted from [104].

lengths of the POs with dashed arrows for those POs not confined by TIR. The POs are labeled with indices (n_x, n_y) equal to half the number of bounces in the x - respectively y -direction. Two examples are shown as insets. The lengths of the POs are

$$\ell_{\text{po}}(n_x, n_y) = 2a\sqrt{n_x^2 + n_y^2}. \quad (5.18)$$

Since all families of POs cover the whole billiard area, i.e. $A_{\text{po}} = a^2$, the semiclassical amplitudes of the POs in Eq. (5.7) are

$$B_{\text{po}} = \frac{F_{\text{po}}}{\sqrt{2}} \frac{a^2}{\sqrt{\ell_{\text{po}}}} = \frac{F_{\text{po}} a^{3/2}}{2\sqrt{n_x^2 + n_y^2}}, \quad (5.19)$$

where $F_{\text{po}} = 2$ for the Fabry-Perot orbits $[(n_x, 0)$ or $(0, n_y)]$ and the diamond orbits ($n_x = n_y$) and $F_{\text{po}} = 4$ for all other POs. The total Fresnel reflection coefficient is

$$R_{\text{po}} = r^{2n_x}(\alpha_{\text{po}}) r^{2n_y}(\alpha'_{\text{po}}) \quad (5.20)$$

with $\alpha_{\text{po}} = \arctan(n_y/n_x)$ being the angle of incidence at the vertical sides and $\alpha'_{\text{po}} = \pi/2 - \alpha_{\text{po}}$ the one at the horizontal sides. The phase φ_{po} in Eq. (5.7) is accordingly

$$\varphi_{\text{po}} = -\frac{\pi}{4} + \arg(R_{\text{po}}). \quad (5.21)$$

Only the diamond PO and its repetitions are contained by TIR and found in the experimental length spectrum accordingly. The small peak predicted by the trace formula for the $(1, 0)$ -orbit (Fabry-Perot orbit, see left inset in Fig. 5.8) is not observed in the experimental length spectrum. Accordingly, the structure of the experimental length spectrum qualitatively agrees with the semiclassical prediction, and it also explains the very simple, equidistant frequency spectrum measured. On a quantitative level, however, there are large differences between the measurement and the trace formula: The peak amplitudes of the experimental length spectrum are less than 15% of the semiclassical ones due to the large amount of unobserved resonances, and they decay exponentially with the number of repetitions μ , while the trace formula predicts an algebraic decay $\propto 1/\sqrt{\mu}$. The exponential decay arises because only one family of superscarred states is observed, and these states have a finite lifetime. The (fluctuating part of the) RD for a single family of superscarred states with resonance frequencies given by

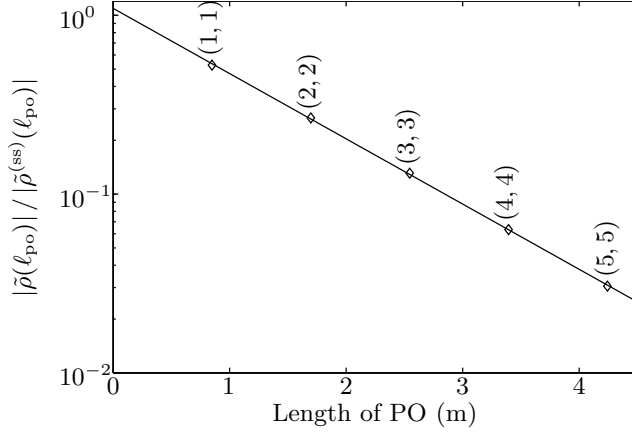


Fig. 5.9: Ratio between the peak amplitudes of the experimental and the super-scar length spectrum. The diamonds are the relative amplitudes for the indicated POs, and the full line is the exponential fit of Eq. (5.23). The slope corresponds to a resonance width of $\Gamma = 56.1$ MHz. Reprinted from [104].

Eq. (5.17) is according to Eq. (B.1)

$$\rho_{\text{fluc}}^{(\text{ss})}(k) = \frac{2nL}{\pi} \sum_{\mu=1}^{\infty} \cos(2\mu nLk - 8\mu\delta). \quad (5.22)$$

This formula predicts a constant amplitude for all repetitions of the diamond orbit as can be seen in Fig. 5.8, where the FT of $\rho_{\text{fluc}}^{(\text{ss})}(k)$, i.e. the length spectrum for a single family of superscars, is plotted as dashed line in the top graph. As can be seen, $\rho_{\text{fluc}}^{(\text{ss})}(k)$ predicts the correct order of magnitude for the amplitudes. However, it does not reproduce their exponential decay because in Eq. (5.22) the imaginary part of k_m arising due to the finite lifetime of the resonances is not accounted for. In Fig. 5.9, the ratio between the peak amplitudes of the experimental and the constructed super-scar length spectrum (see top graph of Fig. 5.8) is plotted with respect to the lengths of the POs together with an exponential fit of the form

$$A_0 \exp(-n\ell_{po}\pi\Gamma/c). \quad (5.23)$$

The fitted parameters are $A_0 = 1.09$ and $\Gamma = 56.1$ MHz, which matches the typical widths of the resonances. Incorporation of the finite lifetime of the resonances,

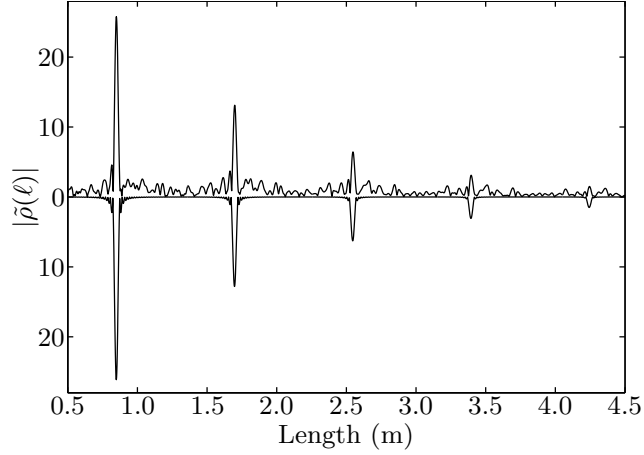


Fig. 5.10: Experimental length spectrum (top graph) and the superscar length spectrum multiplied with the exponential fit from Fig. 5.9, i.e. the FT of Eq. (5.24) (bottom graph). Reprinted from [104].

i.e. the openness of the system, in Eq. (5.22) leads to

$$\rho_{\text{fluc}}^{(\text{sse})}(k) = A_0 \frac{2nL}{\pi} \sum_{\mu=1}^{\infty} e^{-2\mu nL\pi\Gamma/c} \cos(2\mu nLk - 8\mu\delta). \quad (5.24)$$

Figure 5.10 demonstrates that the experimental length spectrum (top graph) is indeed precisely described by the FT of Eq. (5.24) (bottom graph), implying that the experimental length spectrum is completely understood in terms of a single family of superscars.

The Teflon square is an example for a system with just a single dominant PO which thus effectively acts like a one-dimensional system. It should be noted that further series of resonances, namely superscars with higher transverse excitation, may become discernible in the spectrum for higher frequencies or a higher index of refraction (cf. Fig. 4.2). In fact, frequency spectra with just one series of (roughly) equidistant resonances often occur for dielectric resonators, but the example of the Teflon circle (see Fig. 5.5) shows that such spectra are not necessarily connected with a single PO. The difference between the two examples is that the resonance states of the Teflon square are (super)scarred states, while those of the circle are not. Whether this is a general rule remains an open question. Therefore, the connection of a single resonance family to certain POs needs to be analyzed carefully in each case.

5.5 Square alumina resonator

The square alumina resonator (called the alumina square in the following) has a side length of $a = 300.0$ mm, a thickness of $b = 8.3$ mm and an index of refraction of $n = 3.050 \pm 0.008$, which corresponds to a critical angle of $\alpha_{\text{crit}} = 19.1^\circ$. It is, in fact, the same alumina plate which was used for the experiments described in chapter 4. In distinction to these, the alumina square is squeezed between two copper plates to obtain a quasi-2d setup. The frequency spectrum with antennas positioned as shown in Fig. 5.1(b) is plotted in Fig. 5.11. A frequency of 5 GHz corresponds to $ka = 31.4$. The spectrum shows many sharp resonances with quality factors of $Q = 200\text{--}2000$. The Q -values are higher than for the Teflon square because the radiation losses are smaller for a higher index of refraction and the absorption in the alumina is only slightly larger than in the Teflon. Altogether 212 resonances were identified in the range of 1.4–6.1 GHz out of the 1035 resonances expected according to Weyl’s law. In contrast to the Teflon square no single equidistant family of superscarred states can be seen in the spectrum. The reason for this is that due to the smaller value of α_{crit} the diamond PO is not the only PO confined by TIR in the alumina square. A generalized superscar model which takes into account also other trajectories can be constructed in a simple way [111]: For a ray with wave vector (k_x, k_y) traveling in the square, where the x - and y -axes are parallel to the sides of the square, the resonance condition after one roundtrip is

$$\exp(2iak_x)r^2(\chi) = 1 \quad \text{and} \quad \exp(2iak_y)r^2(\pi/2 - \chi) = 1 \quad (5.25)$$

with χ being the angle of incidence on the vertical sides of the resonator. This resonance condition is the generalization of Eq. (5.16) to angles of incidence χ different from 45° . A similar model was proposed in [112]. An approximate solution of this resonance condition is given by

$$\begin{aligned} k_x a &= m_x \pi + i \ln[r(\chi)] \\ k_y a &= m_y \pi + i \ln[r(\pi/2 - \chi)], \end{aligned} \quad (5.26)$$

where (m_x, m_y) are the x - and y -quantum numbers and the angle of incidence is approximated as $\chi = \arctan(m_y/m_x)$. Modes with $m_x \neq m_y$ are doubly

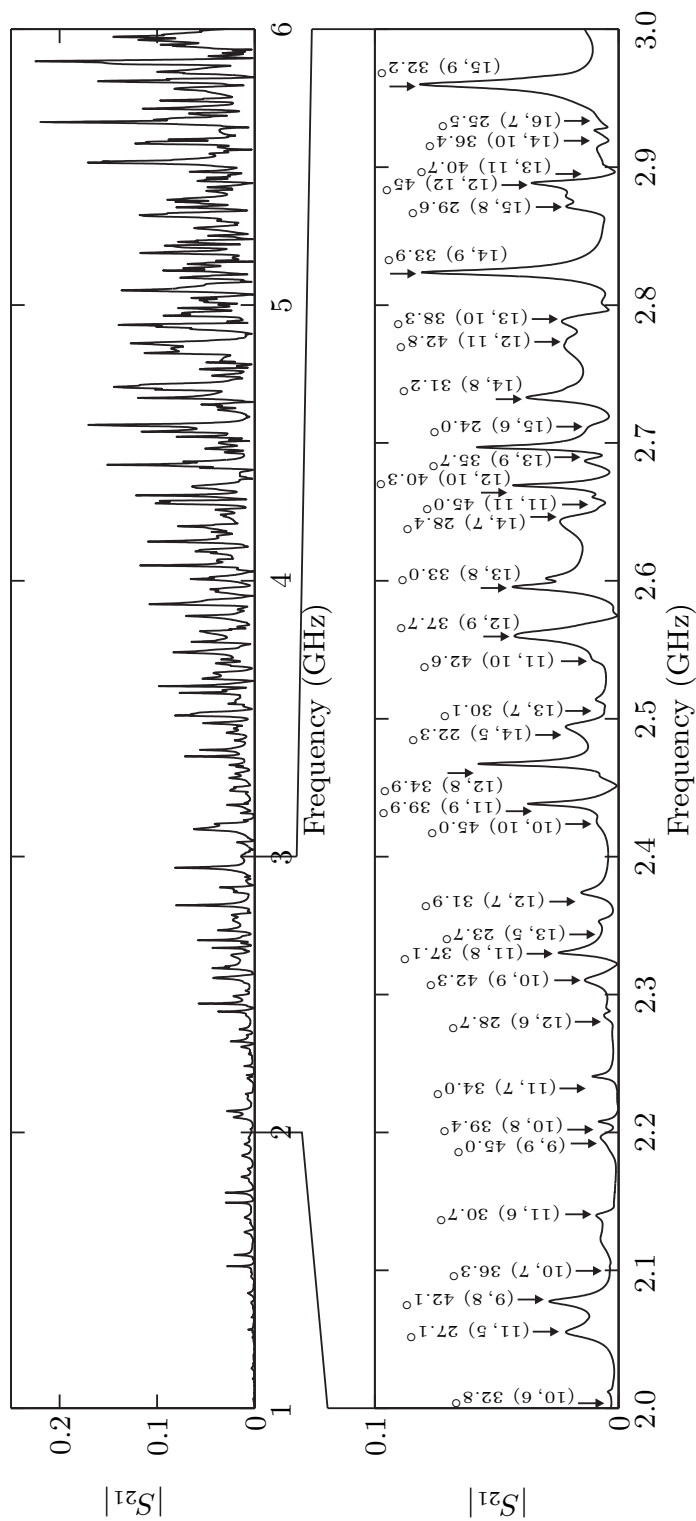


Fig. 5.11: Frequency spectrum of the alumina square. The spectrum shows many sharp resonances with irregular spacings, and cannot be divided into one or several families of equidistant resonances like for the Teflon circle and square. The lower graph shows a magnification of the frequency range from 2–3 GHz. The arrows indicate the resonance frequencies according to the generalized superscar model, Eq. (5.26). The associated quantum numbers (m_x, m_y) and the corresponding angle of incidence $\tilde{\chi}$ are also denoted. Reprinted from [104].

degenerate and the wave number is $k = \sqrt{k_x^2 + k_y^2}/n$. Equation (5.17) is recovered for $m_x \approx m_y$ and $\chi = 45^\circ$. In the magnified part of the spectrum (bottom graph in Fig. 5.11), the resonance frequencies computed from Eq. (5.26) are indicated by arrows together with the quantum numbers and the angle of incidence $\tilde{\chi} = \arctan(k_y/k_x) \approx \chi$ of the wave vector. Only those modes are indicated for which a corresponding resonance was found in the measured spectrum, and computed and measured resonance frequencies agree quite well in most cases. In some cases, on the other hand, there are small deviations, and in a few cases like at 2.7 GHz no clear correspondence was found. Equation (5.26) yields both modes with complex resonance frequencies ($\text{Im}(k) < 0$) for modes with $\chi < \alpha_{\text{crit}}$, i.e. modes with losses due to refractive escape, and lossless modes with $\text{Im}(k) = 0$ for $\chi > \alpha_{\text{crit}}$, which correspond to trajectories confined by TIR. In the latter case other radiative loss mechanisms, e.g. due to the corners [113], are neglected by this model, that is, it does not provide meaningful resonance widths for $\chi > \alpha_{\text{crit}}$. All resonance modes found in the measured spectrum are of this type. For these modes it would be expected in practice that the radiation losses get smaller when $\tilde{\chi}$ approaches 45° , so that the spectrum would be dominated by a series of resonances with $\tilde{\chi} \approx 45^\circ$ like for the Teflon square. The measured spectrum, however, shows no clear correlation between $\tilde{\chi}$ and the widths or amplitudes of the resonances. Preliminary numerical calculations indicate that there is an interaction between the superscar states of the model and the background states (cf. [74]), which would explain why the precision of the calculated resonance frequencies varies for different resonances. This interaction effect is however not yet understood and will be further investigated. Nonetheless the generalized superscar model explains the structure of the spectrum well with the exception of some details like the resonance widths.

The experimental length spectrum is shown in the upright graph of the top panel of Fig. 5.12. There are several peaks corresponding to POs confined by TIR, but most of them are only slightly higher than the noise level. No peaks at the lengths of POs not confined by TIR were observed as for the Teflon circle and square. A comparison with the FT of the trace formula in the bottom panel shows that the peak amplitudes of the experimental length spectrum are less than 35% of the semiclassical ones. This is surprising given that in the case of the circle billiard, 10% of all resonances were sufficient to obtain peaks as high as 80% of

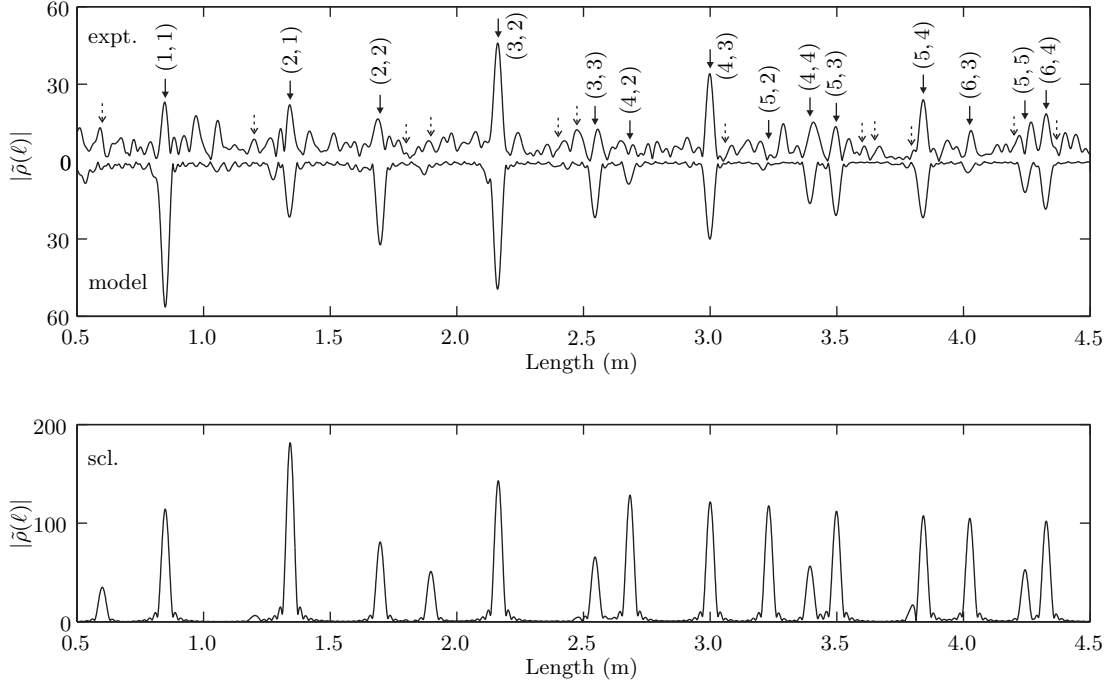


Fig. 5.12: Length spectrum for the alumina square. The upright graph in the top panel is the experimental length spectrum, the inverse graph is a computed length spectrum based on the generalized superscar model. The bottom panel shows the trace formula prediction. Note the different scales of top and bottom panel. The lengths of the POs are indicated by arrows (dashed arrows for POs not confined by TIR) and the indices (n_x, n_y) characterizing the POs are also indicated. The inverse graph in the top panel is the length spectrum for a set of modes computed according to the generalized superscar model, Eq. (5.26). This set of modes consists only of states with $\tilde{\chi} > 28^\circ$, and degenerate modes were counted only once. Reprinted from [104].

the semiclassical prediction, while 20% of all resonances were observed for the alumina square. We conjecture that the relation between the number of observed modes and the peak amplitudes of the experimental length depends strongly on the distribution of the resonance widths for the respective resonators, but this relation is not yet understood. Furthermore, the ratios between experimental and semiclassical peak amplitude vary significantly for the different POs as illustrated in Fig. 5.13. There, the relative peak amplitudes are plotted with respect to the

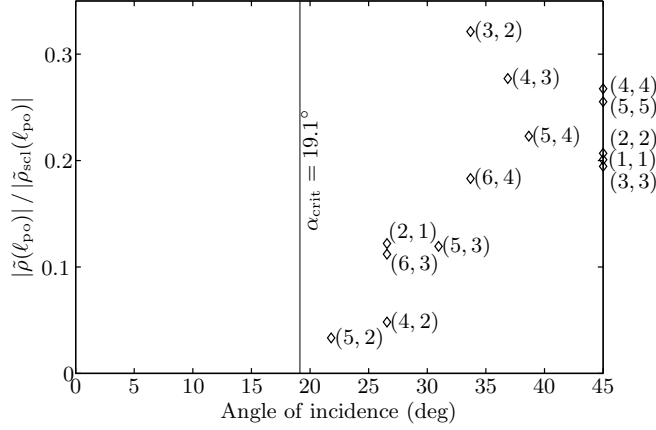


Fig. 5.13: The ratio between the peak amplitudes of the experimental and semi-classical length spectra with respect to the angle of incidence α_{po} of the corresponding PO. The indices (n_x, n_y) of the POs are indicated. The vertical line signifies the critical angle for TIR, and the relative peak amplitudes of the POs get smaller as they get closer to α_{crit} . Reprinted from [104].

angle of incidence α_{po} . It should be noted that the orbits in the square billiard are characterized by two angles of incidence, of which the smaller one is used here (the other one is $\pi/2 - \alpha_{\text{po}}$). The graph clearly shows that the relative peak amplitudes for POs with an angle of incidence close to the critical angle is smaller than for those POs with α_{po} significantly larger than α_{crit} . Exactly the same effect is observed for the Teflon circle in Fig. 5.4, where the higher-order polygons with a large angle of incidence have the highest peak amplitudes. Next, the experimental length spectrum is compared to the generalized superscar model. In fact, the trace formula Eq. (5.7) for the dielectric square can be deduced from Eq. (5.26) when all modes are taken into account [111]. We instead take into account that only a part of all resonances is observed in the measured spectrum and consider only modes computed via Eq. (5.26) with associated angle of incidence $\tilde{\chi}$ greater than a certain cutoff angle χ_{co} . Also, only one mode of each degenerate doublet is taken into account as in the measured spectrum. The cutoff angle was chosen as $\chi_{\text{co}} = 28^\circ$ so that the number of modes obtained from 1.4–6.1 GHz, 215, is comparable with the number of experimentally observed resonances, 212. The lower graph in Fig. 5.11 shows that indeed almost only modes with $\tilde{\chi} > \chi_{\text{co}}$ are observed experimentally. Furthermore, the relative peak amplitudes in Fig. 5.13

start to decline at a similar angle. A uniform resonance widths of $\Gamma = 8$ MHz was assumed for the computed modes since as outlined above the model does not yield a meaningful estimate of their resonance widths. This value of Γ is similar to the typical measured resonance widths. The length spectrum computed from this set of modes is plotted in the inverse graph of the top panel of Fig. 5.12, and it shows good agreement with the experimental length spectrum (upright graph). An exception are the (1,1)- and the (2,2)-orbit, for which peak amplitudes significantly larger than the experimental ones are obtained. In conclusion, even though some details cannot be explained by the generalized superscar model, it describes the general features of both the frequency and the length spectrum of the alumina square very well and thus enables a deeper understanding of the square alumina resonator.

The data for the alumina square confirms the observation which was made for the Teflon circle, namely that the most long-lived and thus experimentally observable modes mainly contribute to those POs with angles of incidence far away from the critical angle, while POs close to it are significantly suppressed. The comparison with the Teflon square furthermore shows that the larger number of POs confined by TIR due to the higher index of refraction is reflected in a frequency spectrum with a more complicated structure. Thus, the structure of the frequency and length spectrum of a resonator is not only determined by its shape, but also by the index of refraction respectively the critical angle for TIR.

5.6 Conclusions

In conclusions, the length spectra deduced from the measured frequency spectra of three different 2d dielectric microwave resonators show peaks at the lengths of the POs of the corresponding classical billiards as predicted by the trace formula proposed in [39]. The amplitudes of these peaks are, however, smaller than predicted by the trace formula because only between 2% and 20% of all resonances are actually observed experimentally. Moreover, peaks corresponding to POs not confined by TIR were not observed, even if a finite amplitude is predicted semi-classically. The deviations of the peak amplitudes for POs close to the critical

angle, but still confined by TIR, from the predicted ones are considerably larger than for POs far away from the critical angle. The reasons for this are twofold: First, the trace formula was derived in the strict semiclassical limit $k \rightarrow \infty$, whereas for large though finite k further corrections are necessary especially close to the critical angle [39]. Second, the experimentally observed, long-lived resonance modes seem to correspond mainly to those POs with angles of incidence far away from the critical angle, which in a classical dielectric billiard are the ones with the longest lifetimes. This systematics of observed and unobserved modes must be taken into account for an understanding of the experimental length spectra. The comparison of the Teflon and the alumina square furthermore demonstrates that there is a connection between the number of POs contributing to the length spectrum and the complexity of the frequency spectrum. Accordingly, not only the shape, but also the index of refraction and resulting number of POs confined by TIR should be taken into account for the design of dielectric cavities. Another important conclusion is that individual resonances or single families of resonances are in general not related to certain POs, and only scarred states may be an exception to this rule. Spectra with a single family of resonances often occur in microlaser or -cavity experiments, and the corresponding length spectra must be analyzed especially carefully.

In summary, the length spectrum and the trace formula for dielectric resonators are useful tools for the investigation of the ray-wave-correspondence in such devices. The advantage of such an analysis is that only the resonance frequencies and widths are needed, but no information on the field distributions of the resonance states. The drawback is that no information on individual resonances is obtained and that a sufficiently large number of resonances is needed to obtain a meaningful length spectrum. All three resonators investigated above are passive systems and have regular classical counterparts. Therefore, the test of the trace formula for (partially) chaotic systems or systems with an active medium like microlasers are future challenges. Furthermore, the resonators investigated here were two-dimensional, but microlasers typically have a flat, but three-dimensional geometry like the resonators investigated in chapter 3. The applicability of the trace formula for 2d dielectric cavities to flat 3d ones remains to be tested. First results are presented in chapter 6.

6 Trace formula for three-dimensional dielectric cavities

In the previous section, the trace formula for two-dimensional dielectric cavities was tested extensively with three resonators. However, typical microlasers and -cavities consisting of flat dielectric plates [see Fig. 2.1(c)] are not two-dimensional. It is not clear how to describe the length spectra of such resonators and whether the trace formula for 2d resonators is applicable or needs to be extended. In the following, we will investigate the length spectra of flat 3d dielectric resonators with two different approaches: the first approach is to treat the cavities as what they are, namely 3d objects with the index of refraction n of their material (3d–approach). This will be discussed in detail in section 6.1. It should be noted that trace formulas for metallic 3d microwave resonators exist and have been tested experimentally [98–100], but to the author’s knowledge none exist for dielectric 3d resonators. The second approach is based on the n_{eff} –model introduced in section 2.7, namely the cavity is treated as a 2d object with index of refraction equal to n_{eff} , and the 2d trace formula is combined with the n_{eff} –model to obtain a simplified semiclassical description (n_{eff} –approach). We demonstrated in chapter 3 that the n_{eff} –model does not precisely reproduce the measured frequency spectra, but rather suffers from a systematic error. Consequently, a test of the n_{eff} –approach, that is whether it yields a reasonable description of the length spectra, is necessary. This is discussed in section 6.2. The investigation of the trace formula for 3d dielectric cavities has not yet been completed, and in the following sections a number of open questions are posed. Nonetheless, a summary of the preliminary results and a comparison of the different approaches is given in section 6.3 along with the an outlook.

The measurements were performed with the same circular Teflon disks and setup as in chapter 3 (see Fig. 3.2). Disk A has a radius of $R = 274.8$ mm, a thickness of $b = 16.7$ mm and an index of refraction of $n = 1.434$, and disk B has $R = 274.9$ mm, $b = 5.0$ mm and $n = 1.439$. The resonances were classified according to their polarization using the technique described in section 3.1.

6.1 Three-dimensional approach

In the 3d–approach, the FT of the fluctuating part of the resonance density, $\rho_{\text{fluc}}(k)$, is calculated as

$$\tilde{\rho}(\ell) = \int_{k_{\text{min}}}^{k_{\text{max}}} dk \rho_{\text{fluc}}(k) \exp\{-ikn\ell\}, \quad (6.1)$$

with the real index of refraction n in the exponent as in Eq. (5.8). In contrast to chapter 5, no window function was used for the FT throughout this chapter to simplify the calculations. It should be noted that n cannot be determined from the length spectrum as in chapter 5 since there is no reliable prediction for the positions of the peaks. The length spectrum computed for 286 measured TM_0 modes³ of disk A in the regime of 6.8–20.0 GHz is shown in Fig. 6.1. All modes were counted twice (for a total of 572 modes) due to their double degeneracy. The length spectrum shows three dominant peaks in the plotted length regime, but their identification with certain POs proves difficult: From the length spectrum for the 2d Teflon circle in Fig. 5.4 it would be expected that the first two major peaks correspond to the pentagon and the hexagon orbit, respectively, and the third peak to the heptagon and octagon orbit. The lengths of the different POs in the 2d circle billiard, $\ell_{\text{po}}(q, \eta)$ given by Eq. (5.11), are indicated by the black arrows, along with the circumference $2\pi R$. The expected correspondence is, however, not confirmed; the peaks are located at larger lengths than in the 2d case (Fig. 5.4). In fact, the third peak is located at a length larger than the circumference, where no POs exist in the 2d circle billiard. This proves that the resonator has to be treated as a 3d object, that is the POs of the 3d circular cylinder billiard need to be considered. These can be designated with three indices, (q, η, ξ) , where q and η have the same meaning as for the 2d circle billiard, and ξ is half the number of bounces at the top and bottom surface of the cylinder. One example, the $(4, 1, 2)$ –orbit, is illustrated in Fig. 6.2. The lengths of the 3d POs are then

$$\ell_{\text{po}}(q, \eta, \xi) = \sqrt{\ell_{\text{po}}^2(q, \eta) + (2\xi b)^2} = \ell_{\text{po}}(q, \eta) / \sin \theta \quad (6.2)$$

³Modes with higher z –excitation appear in the spectrum at about 16 GHz, but could be excluded with the help of the measured intensity distributions.

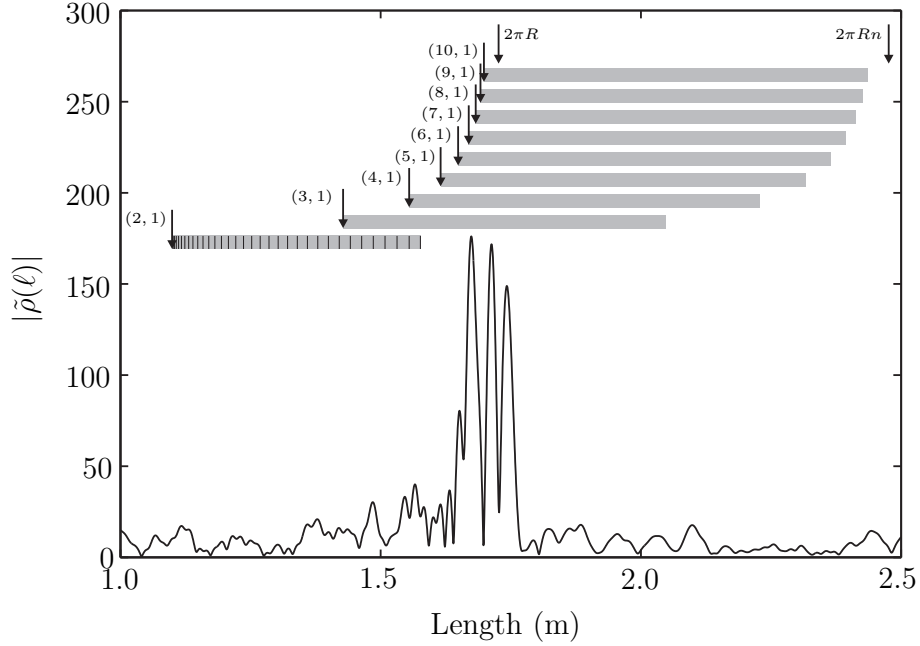


Fig. 6.1: Length spectrum (3d-approach) for the TM_0 modes of disk A. The black arrows indicate the lengths $\ell_{\text{po}}(q, \eta)$ of the 2d POs and of the circumference, $2\pi R$. For each 2d PO, there is a family of associated 3d POs, and the gray bars indicate the length regime in which the associated 3d POs are confined by TIR. For the $(2, 1)$ -orbit, the individual 3d POs are also indicated by small black lines. They almost form a continuum especially close to the associated 2d PO. Only POs with $q \leq 10$ and $\eta = 1$ are indicated. The peaks in the length spectrum cannot be identified with the 2d POs, and also not with certain 3d POs due to their large number and density.

where $\ell_{\text{po}}(q, \eta)$ is the length of the (q, η) -PO in the 2d circle billiard given by Eq. (5.11) and θ is the angle of incidence at the top and bottom surface of the cylinder. Accordingly, every 2d PO comes with an infinite series of corresponding 3d POs. Only those which are confined by TIR in z -direction, i.e. with $\theta \geq \alpha_{\text{crit}}$, are expected to yield a relevant contribution. These POs have lengths between $\ell_{\text{po}}(q, \eta)$ and $\ell_{\text{po}}(q, \eta, \xi_{\text{crit}}) \leq n \ell_{\text{po}}(q, \eta)$. The associated length intervals are indicated by the gray bars in Fig. 6.1. For the $(2, 1)$ -orbit, the individual 3d POs are in addition indicated by black lines to demonstrate that the 3d POs lie very densely and almost form a continuum close to the length of the related 2d PO.

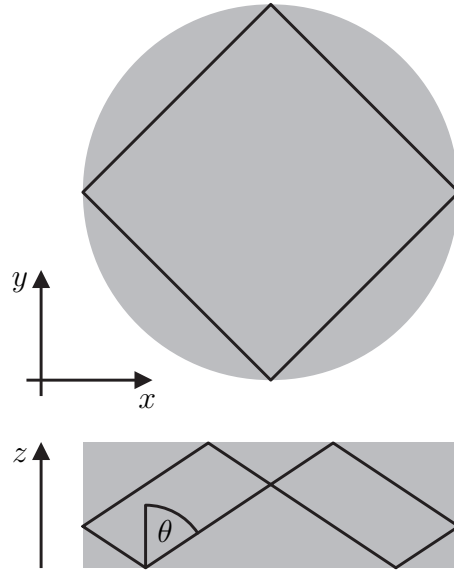


Fig. 6.2: Top view (upper panel) and side view (lower panel) of a PO in the circular cylinder billiard. It bounces back and forth twice in the z -direction, and is thus designated as $(4, 1, 2)$. The angle of incidence on the bottom and top surfaces is θ .

Due to the large number and the high density of the 3d POs, an identification of the peaks with certain 3d POs is impossible. Indeed, it is surprising that only three peaks are seen in the length spectrum and only in a small length regime despite the large number of 3d POs confined by TIR which moreover span a much larger length interval. An explanation might be that in a 3d trace formula for the RD most of the contributions of these closely spaced POs interfere destructively, but this can only be clarified by developing and investigating the trace formula for such cylindrical 3d dielectric resonators. Furthermore, it is questionable whether a semiclassical approximation is meaningful at all for the 3d-approach: the semiclassical regime corresponds to frequencies large, respectively wavelengths small as compared to the system's dimensions. The maximal frequency considered, $f_{\max} = 20$ GHz, corresponds to a free-space wavelength of $\lambda = 15$ mm, which is small compared to the radius R , but is in the same order of magnitude as the thickness b . This means that the semiclassical limit is not yet reached for the z -direction. The large aspect ratio R/b respectively small b is also the reason for the high density of the 3d POs, and a frequency of 20 GHz seems to be simply not sufficient to resolve the densely spaced POs.

The length spectrum for the TE₀ modes of disk A (not shown here) also shows a small number of dominant peaks which cannot be related to certain POs, i.e. exactly the same qualitative behavior as for the TM₀ modes is found. In conclusion, no clear interpretation in terms of POs could be obtained for the length spectrum of the Teflon disk A in the 3d–approach, and it remains doubtful whether this is actually possible since the semiclassical limit is not reached for the z –direction. Therefore, the n_{eff} –approach, i.e. treating the disk as an approximately two-dimensional system, seems more promising and will be investigated in the next section. Nonetheless, the length spectrum in the 3d–approach shows a simple and clear structure which should be understood.

6.2 Approach with effective index of refraction

In the n_{eff} –approach, the FT of the RD is calculated as

$$\begin{aligned}\widehat{\rho}(\ell) &= \int_{k_{\min}}^{k_{\max}} dk \rho_{\text{fluc}}(k) \exp\{-ikn_{\text{eff}}(k)\ell\} \\ &= \sum_j \exp\{-ik_j n_{\text{eff}}(k_j)\ell\} - \text{FT}\{\rho_{\text{Weyl}}(k)\},\end{aligned}\tag{6.3}$$

where the effective index of refraction is used instead of the real one. This means that the 3d resonator is considered as a 2d resonator with effective index of refraction here. This ”effective” length spectrum for the TM₀ modes of disk A (same data set as in the previous section) is plotted as solid line in the top graph of Fig. 6.3. The solid arrows indicate the lengths of the POs depicted as insets. The dashed line in the top graph is the FT (taken from 6.8–20 GHz) of the exact trace formula

$$\rho_{\text{fluc}}(k) = \sum_{\text{po}=(q,\eta)=-\infty}^{\infty} \int dm \frac{4}{\pi^2 k} \exp(2\pi i \eta m) P_m(R_m E_m)^q + \text{c.c.}\tag{6.4}$$

The details of the terms P_m , R_m and E_m (which are functions of k and n_{eff} each) are given in appendix C together with a derivation of the formula. It is a modification of Eq. (66) in [39] incorporating the frequency dependence of n_{eff} . The semiclassical trace formula Eq. (5.7) for the circle (with n replaced by n_{eff})

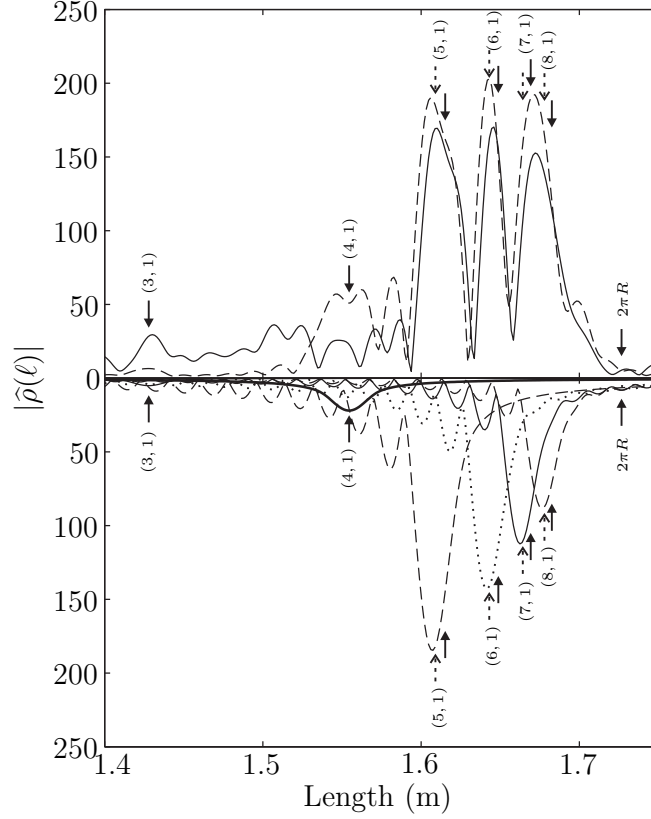


Fig. 6.3: Length spectrum (n_{eff} -approach) for the TM_0 modes of disk A. The solid line in the top graph is the experimental length spectrum evaluated according to Eq. (6.3), and the dashed line is the FT of the exact trace formula, Eq. (6.4). The curves in the bottom graph are the contributions of the individual POs to the exact trace formula. The solid arrows denote the lengths of the POs denoted by (q, η) , and the dashed arrows indicate the peak positions of the trace formula estimated from Eq. (6.8).

is recovered in the limit $k \rightarrow \infty$. When calculating the integral over m in this limit, the term R_m^q becomes the total Fresnel coefficient R_{po} , the term $e^{2\pi i \eta m} E_m^q$ becomes the oscillating term $e^{i(nk\ell_{\text{po}} + \varphi_{\text{po}})}$, and P_m contributes to the amplitude B_{po} . This exact trace formula is used instead of its semiclassical approximation Eq. (5.7) because the latter does not give the correct amplitudes for the POs close to the critical angle (see section 5.3 and Fig. 5.4). While this concerned only the $(4, 1)$ -orbit in Fig. 5.4, this is not the case here. Figure 6.4 shows the critical angle $\alpha_{\text{crit}} = \arcsin(1/n_{\text{eff}})$ with respect to the frequency. Indeed, most POs are close to the critical angle in some part of the considered frequency interval. Only

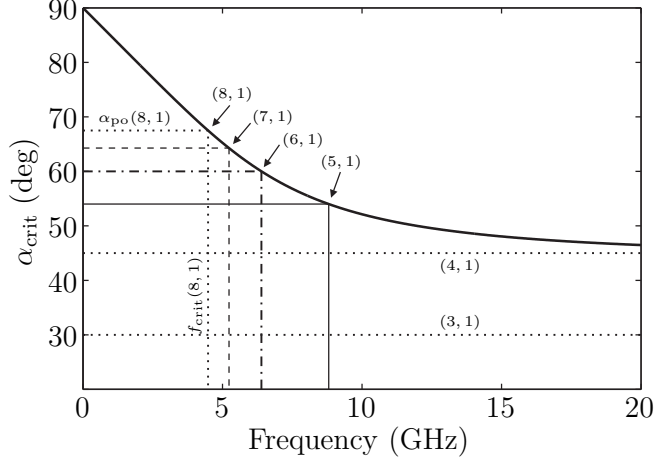


Fig. 6.4: Critical angle $\alpha_{\text{crit}} = \arcsin(1/n_{\text{eff}})$ with respect to the frequency for the TM_0 modes of disk A. The horizontal lines indicate the angles of incidence α_{po} of the (q, η) -orbits, and the vertical lines indicate the critical frequency f_{crit} at which the POs become confined by TIR. Some POs like the $(4, 1)$ -orbit are not confined in the whole frequency regime.

POs with $\eta = 1$ and $q \leq 10$ were used in the calculation of the exact trace formula to keep the computation time reasonable. The small peak at the length $\ell \approx 1.7$ m between the $(8, 1)$ -orbit and the circumference $2\pi R$ is an artifact due to the finite q . A close inspection of the graph shows that the positions of the peaks of the experimental length spectrum (solid line) do not agree with the lengths of the POs (solid arrows), and the positions of the peaks of the FT of the trace formula (dashed line) agree with neither of them. There are two reasons for these discrepancies. The first reason is the frequency dependence of n_{eff} [cf. Fig. 3.7(a)]. This leads to a shift of the peaks of the trace formula to lengths smaller than those of the POs. The second reason is the systematic error of the n_{eff} -model, due to which the peaks of the experimental length spectrum are shifted to larger lengths than predicted by the trace formula. The second effect thus partly compensates the first one. They are explained in detail in the following.

Concerning the first effect the crucial point is that the Fresnel reflection coefficient also depends on the frequency in the case considered here since it is a function of $n_{\text{eff}}(k)$. Thus a PO confined by TIR has a frequency dependent Fresnel phase (denoted by $\arg(R_{\text{po}})$ in the semiclassical trace formula). Each peak in the length spectrum is formed by the contributions of one PO over the whole

frequency range, and the interference between the corresponding Fresnel phases leads to a shift of the peak position. This effect is similar to (but not the same as) the Goos-Hänchen shift [114, 115]. The effect is seen best in the bottom graph of Fig. 6.3, where the contributions of individual POs, i.e. of certain summands of the exact trace formula Eq. (6.4), are shown. The positions of the peaks, ℓ_{peak} , clearly deviate from the lengths of the POs indicated by the solid arrows for the POs confined by TIR, whereas those of the square and triangle orbit, which are not confined in the frequency interval considered (see Fig. 6.4), are not shifted. The magnitude of the shift can be estimated from the semiclassical trace formula as follows: When taking the FT [as in Eq. (6.3)] of the semiclassical trace formula Eq. (5.7) with n replaced by n_{eff} , the oscillating term of the integrand reads

$$\exp \{ig(k)\} = \exp \left\{ i \left[n_{\text{eff}} k (\ell_{\text{po}} - \ell) + \frac{\pi}{4} - q \frac{\pi}{2} + \arg [R_{\text{po}}(n_{\text{eff}})] \right] \right\}. \quad (6.5)$$

The integral over this term is largest for those ℓ for which the phase is stationary, i.e. the derivative $\frac{dg}{dk}$ of the exponent is equal to zero. The Fresnel phase is

$$\arg [R_{\text{po}}(n_{\text{eff}})] = -2q \delta(\alpha_{\text{po}}, n_{\text{eff}}) \quad (6.6)$$

with

$$\delta(\alpha, n) = \arctan \left\{ \frac{\sqrt{n^2 \sin^2(\alpha) - 1}}{n \cos(\alpha)} \right\} \quad (6.7)$$

and the definition Eq. (2.26) for δ . Computing $\frac{dg}{dk}$ and solving for ℓ yields

$$\ell_{\text{peak}} \approx \ell_{\text{po}} - 2q \left. \frac{\frac{\partial \delta}{\partial n_{\text{eff}}} \frac{dn_{\text{eff}}}{dk}}{n_{\text{eff}} + \frac{dn_{\text{eff}}}{dk} k} \right|_{k_0} \quad (6.8)$$

for the position of the peaks, referred to in the following as the peak positions of the trace formula. They are equal to the lengths of the corresponding POs plus a correction due to the frequency dependent Fresnel phase. This approximation corresponds to a linear Taylor expansion of g around k_0 , which is chosen as

$$k_0 = \begin{cases} \frac{1}{2}(k_{\text{min}} + k_{\text{max}}) & : k_{\text{crit}} < k_{\text{min}} \\ \frac{1}{2}(k_{\text{crit}} + k_{\text{max}}) & : k_{\text{crit}} \geq k_{\text{min}} \end{cases} \quad (6.9)$$

with $f_{\text{crit}} = ck_{\text{crit}}/(2\pi)$ corresponding to the frequency where α_{crit} is reached (see Fig. 6.4). The reason for this choice of k_0 is that the frequency regime below

f_{crit} does not contribute to the shift of the PO since $\arg[R_{\text{po}}] = 0$ there. Moreover the peak position depends on the frequency interval $[f_{\text{min}}, f_{\text{max}}]$ considered. The resulting estimates Eq. (6.8) for ℓ_{peak} are indicated by the dashed arrows in Fig. 6.3, and they reproduce the peak positions of the trace formula prediction very well. However, the estimate may be worse if g cannot be approximated well with a linear function in the considered frequency regime. The same effect is also responsible for the oscillating tail to the left of the single orbit contributions to the trace formula (see e.g. the dashed line for the pentagon-orbit in the bottom graph of Fig. 6.3), which are not observed for those POs not confined as e.g. the square-orbit (solid line). These tails can lead to unexpected interference patterns, for example the right shoulder around 1.62 m of the (5, 1)-peak of the trace formula prediction (dashed line in the top graph) stems from the tail of the (6, 1)-contribution, and the double peak at the length of the (4, 1)-orbit around 1.55 m originates from interference between the (4, 1)- and the (5, 1)-contributions. It should be noted that the shift of the peak positions due to the frequency dependent Fresnel phase also appears for a 2d dielectric resonator with a frequency dependent index of refraction.

Concerning the second effect it was shown in Fig. 3.9 for the TM modes of disk A that the resonance spacings (for modes with the same radial quantum number) predicted by the n_{eff} -model are slightly, but systematically larger than the measured spacings. These deviations are accompanied by a shift of the peaks in the length spectrum. Namely, a system with equidistant resonances with resonance spacing Δf (i.e. a particle in a 1d box potential or a resonator with a family of WGMs) has a length spectrum with a peak at

$$\ell_{\text{po}} = c/(\Delta f). \quad (6.10)$$

A small shift $\delta(\Delta f)$ of the resonance spacing leads to a shift $\delta(\ell_{\text{po}})$ of the peak position, related via

$$\frac{\delta(\ell_{\text{po}})}{\ell_{\text{po}}} = -\frac{\delta(\Delta f)}{\Delta f}. \quad (6.11)$$

Therefore, a deviation $\delta(\Delta f_m) = \Delta f_m^{\text{expt}} - \Delta f_m^{\text{calc}} \approx -0.4$ MHz compared to a resonance spacing $\Delta f_m \approx 120$ MHz corresponds to a shift $\delta(\ell_{\text{po}}) = \ell_{\text{po}}^{\text{expt}} - \ell_{\text{po}}^{\text{calc}}$ of about 5 mm for a peak at about 1.6 m. Indeed, it equals $\delta(\ell_{\text{po}}) \approx 4$ mm for the pentagon-orbit and $\delta(\ell_{\text{po}}) \approx 3$ mm for the hexagon-orbit. Of course Eq. (6.11) is only an approximation for the effect of the systematic error, but it explains

the principle well and yields a reasonable estimate for the magnitude of the shift, even though in practice the magnitude of the deviations between the n_{eff} -model expectation and experimental data cannot be predicted reliably. Furthermore, an error in the determination of the index of refraction n of the material would lead to an additional shift of the peaks. Nonetheless, Fig. 6.3 demonstrates that the combination of the trace formula for 2d dielectric billiards with the n_{eff} -model yields a satisfactory prediction for the experimental length spectrum, and that the peaks can be successfully identified with the POs.

The length spectrum for the TM_0 modes of disk B is shown as solid line in the

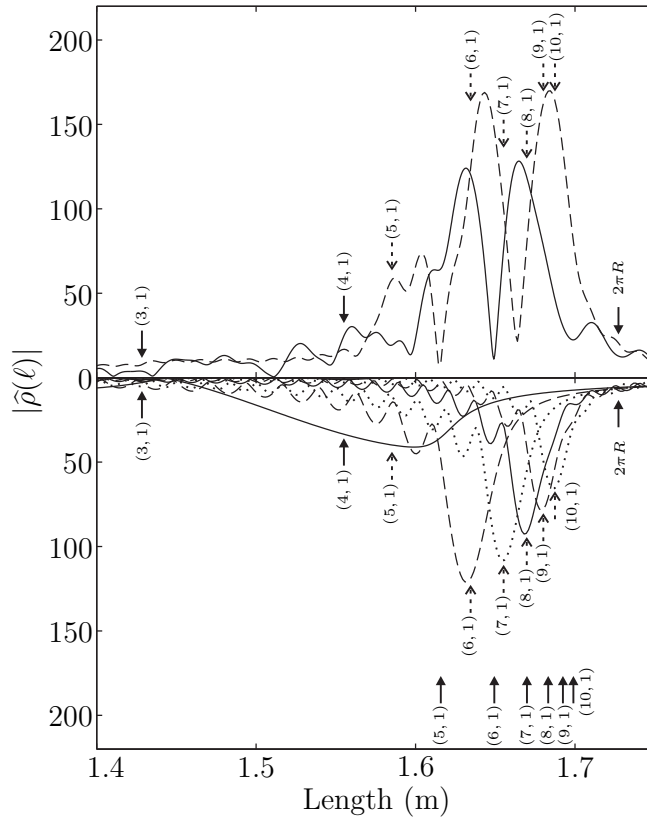


Fig. 6.5: Length spectrum (n_{eff} -approach) for the TM_0 modes of disk B. The solid line in the top graph is the experimental length spectrum according to Eq. (6.3), and the dashed line is the FT of the exact trace formula, Eq. (6.4). The curves in the bottom graph are the contributions of the individual POs to the exact trace formula. The solid arrows denote the lengths of the POs denoted with (q, η) , and the dashed arrows indicate the peak positions of the trace formula estimated from Eq. (6.8).

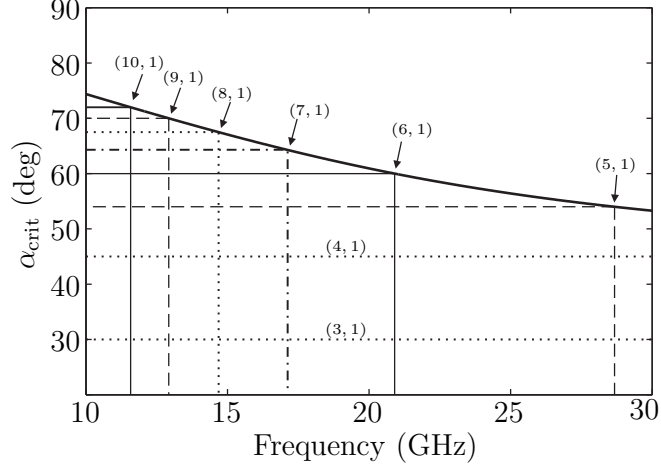


Fig. 6.6: Critical angle $\alpha_{\text{crit}} = \arcsin(1/n_{\text{eff}})$ with respect to the frequency for the TM_0 modes of disk B. The horizontal lines indicate the angles of incidence α_{po} of the (q, η) -orbits, and the vertical lines indicate the critical frequency f_{crit} at which the POs become confined by TIR.

top graph of Fig. 6.5. The dashed line is the FT of the exact trace formula from 16.1–30 GHz with $q \leq 10$. The lengths of the POs are indicated with the solid arrows while the dashed arrows indicate the estimated peak positions of the trace formula, ℓ_{peak} according to Eq. (6.8). Both the experimental length spectrum and the FT of the trace formula have two major peaks. A comparison of the trace formula prediction (dashed line) with the estimates ℓ_{peak} (dashed arrows) shows that the first peak corresponds to the (6, 1)- and (7, 1)-orbits and the second one to the (9, 1)- and (10, 1)-orbits, while the (8, 1)-orbit is located in between. This surprising correspondence between the peaks and the POs is attributed to the strong interference between the different contributions of the individual POs (see bottom graph). The difference between the peak positions of the experimental length spectrum and the trace formula prediction is $\delta(\ell_{\text{po}}) = -12$ mm for the first peak and -19 mm for the second one. The deviation between measured and calculated resonance spacings is $\delta(\Delta f_m) \approx 0.8$ MHz, which corresponds to $\delta(\ell_{\text{po}}) = -11$ mm according to Eq. (6.11). The sign of the shift differs from that for disk A since the experimental resonance spacings are larger than the calculated ones in this case. Furthermore, the shift is significantly larger for the second peak compared to the first one and also to the estimate from Eq. (6.11). An explanation for this might be that the contribution of the (8, 1)-orbit interferes

constructively with the other PO-contributions instead of destructively as predicted by the trace formula. Moreover the small double peak at the $(5, 1)$ -orbit observed for the FT of trace formula is not found in the experimental length spectrum. The reason for this is that the pentagon orbit is not confined by TIR in almost the whole frequency range, as can be seen in Fig. 6.6.

In conclusion, the length spectra obtained with the n_{eff} -approach can be successfully interpreted in terms of POs. However it is crucial to account for the two mechanisms leading to shifts of the peaks, i.e. the frequency dependence of the Fresnel phase and the systematic error of the n_{eff} -model. For example, the peak position of the trace formula for the $(8, 1)$ -orbit (dashed arrow) in Fig. 6.5 is almost identical with the geometrical length of the $(7, 1)$ -orbit (solid arrow), which allows for a false identification of the peak. The shifts in the case of disk A are smaller and lead to less confusion than for the case of disk B which is a rather extreme one. The main problem with the second mechanism is that the magnitude of the systematic error is generally not known and cannot be predicted. Furthermore, the peak amplitudes of the experimental length spectra are not understood: From Fig. 5.4 it is expected that the amplitudes predicted by the trace formula are more accurate for the higher-order polygons, but the opposite is the case in Fig. 6.5. The reason for this is not clear, but it could also be related to a further systematic error of the n_{eff} -model. Figures 3.12 and 3.15 demonstrate that the n_{eff} -model predicts incorrect resonance widths, and these are related to the amplitudes of the peaks in the length spectrum. Nonetheless, the 2d trace formula combined with the n_{eff} -model provides good predictions for the experimental length spectra at least on a qualitative level.

6.3 Conclusions

A comparison between the two approaches shows that so far only the n_{eff} -approach allows for a clear interpretation of the experimental length spectra, although different mechanisms leading to shifts of the peaks must be taken into account. While the basic principles and important effects for this approach are understood, the peak amplitudes of the length spectrum are not. Furthermore,

a trace formula for the TE modes is still missing. The main drawbacks of the n_{eff} -approach, however, are that the trace formula is mathematically rather complicated and that the systematic error of the n_{eff} -model remains an effect of unpredictable magnitude. The 3d-approach, on the other hand, should not suffer from systematic errors and might be mathematically less complicated since no frequency dependent n_{eff} is used, but up to now there is no 3d trace formula or any other means of interpreting the experimental length spectrum. In conclusion, both approaches are not yet fully understood, but the results presented demonstrate that it is worthwhile to develop both of them further in order to achieve a full understanding of the length spectra of flat 3d dielectric resonators.

7 Conclusions

Dielectric cavities are of great interest not only due to the multitude of applications concerning microcavities and -lasers, but also because they are paradigms of wave-mechanical chaos in open systems. Especially the correspondence between the wave- and ray-dynamics has attracted much attention. In this thesis, different aspects of dielectric resonators were investigated experimentally with macroscopic dielectric microwave resonators.

The first part of the thesis was the test of the n_{eff} -model, a 2d approximation for flat 3d resonators, as e.g. used for microlasers. This approximation is widely applied due to its simplicity and was also utilized for the other parts of the thesis. The experiments showed that the model predicts the correct order of magnitude for resonance frequencies and widths, but is too imprecise for a direct comparison with the measured spectra. This systematic error is a considerable drawback of the model and demonstrates the need for improvement. It is conjectured that a better treatment of the boundary conditions at the edges of the resonator is essential.

The other parts of the thesis dealt with the connections between different properties of the dielectric resonators and the periodic orbits of the corresponding classical billiards. First, the near field distributions of a square resonator were measured. The measurements confirmed the existence of superscarred states in dielectric cavities as predicted by [38], and provide the first direct experimental evidence. It is expected that similar states are found for cavities of other polygonal shapes as well. In addition, scarred states with unexpected properties were observed, raising the question of their physical origin. It is believed that the existence of (super-)scarred states in polygonal resonators is related to the scattering properties of the dielectric corners, which are not well understood so far, despite the many applications of polygonal cavity shapes.

Furthermore, the resonance density of both 2d and 3d resonators was investigated and compared to the predictions of a trace formula for 2d dielectric resonators which relates it to the periodic orbits [39]. The length spectra for different 2d resonators clearly revealed the influence of the periodic orbits. Deviations from the trace formula prediction were attributed to the large number of resonances not observed experimentally. Furthermore, the experimental results demonstrated a

connection between the most long-lived resonant states and the best confined periodic orbits. The experimental data for the 3d resonators was analyzed with a combination of the 2d trace formula and the n_{eff} -model. Then the connection between the resonance density and the periodic orbits emerges, but additional effects due to the dispersion of the effective index of refraction and the systematic error of the n_{eff} -model must be taken into account. The results thus demonstrate again both the usefulness of the trace formula and the need of an improved n_{eff} -model.

In conclusion, the experimental results provide evidence of the importance of periodic orbits for the understanding of dielectric resonators. Most investigations concerning periodic orbits focus on the connections between periodic orbits and the far field distributions [32–34], but our results demonstrate their much broader impact. Especially the length spectra are a practical tool for analyzing their influence. Furthermore, there seems to be a connection between the occurrence of scarred states and the structure of the length spectrum, as was observed for square resonators with different indices of refraction. However, these connections are not clear yet and need to be further investigated. Furthermore, all experiments were done with cavities with integrable classical counterparts, i.e. circular and square resonators. The study of e.g. the trace formula for systems with chaotic dynamics remains an interesting future problem.

A Effective index of refraction for other setups

A.1 Setup with additional metal plate

In this section, the effective index of refraction for the setup shown in Fig. A.1 is calculated. This setup is used in chapter 4 and for measuring the polarization of resonance modes (cf. section 3.1). The only modification of the setup with respect to the one shown in Fig. 2.3 is the additional metal plate at a distance D to the dielectric plate.

A.1.1 Modified Fresnel reflection coefficients

First, we calculate the modification of the Fresnel reflection coefficients for the setup shown in Fig. A.2, where a ray traveling in medium I is reflected at the interface with medium II and at the metal plate which is placed at a distance D behind the interface between medium I and II. The coordinate system used in this section is shown in Fig. A.2. The general ansatz for the field E_z (TM modes) respectively B_z (TE modes) of a wave traveling in the z -direction is (cf. section 2.7)

$$E_z, B_z = \begin{cases} A\Psi(x, y) (e^{ik_z z} + r e^{-ik_z z}) e^{-i\omega t} & : z \leq 0 \\ \Psi(x, y) (b_1 e^{-qz} + b_2 e^{+qz}) e^{-i\omega t} & : 0 \leq z \leq D \end{cases} \quad (\text{A.1})$$

where A , b_1 and b_2 are constants and r is the modified Fresnel reflection coefficient. The wave function Ψ satisfies $(\Delta + \gamma^2)\Psi = 0$, and γ , k_z and q fulfill the dispersion

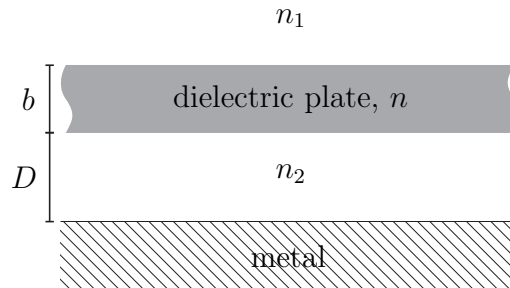


Fig. A.1: Dielectric plate with additional metalplate beneath.

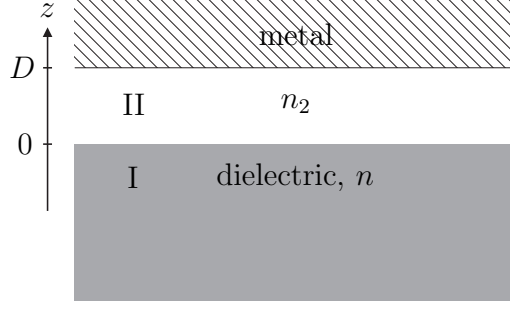


Fig. A.2: Coordinate system for the calculation of the modified Fresnel reflection coefficients.

relation

$$\frac{\omega^2}{c^2} = k^2 = \frac{\gamma^2 + k_z^2}{n^2} = \frac{\gamma^2 - q^2}{n_2^2} = \frac{\gamma^2}{n_{\text{eff}}^2}. \quad (\text{A.2})$$

It should be noted that we assume that the wave is totally reflected at the interface between medium I and II, which corresponds to a real decay constant q , but the following calculations are also correct for complex q . First we consider TM modes. Since E_z must fulfill Neumann boundary conditions at the metal plate at $z = D$, the field in II can be written in the form

$$E_z^{(II)} = B\Psi \cosh [q(z - D)]e^{-i\omega t} \quad (\text{A.3})$$

where B is another constant. Now we introduce the boundary conditions at the interface at $z = 0$. Since $n_j^2 \vec{E}_\perp^{(j)} \propto E_z$ must be continuous, we get with Eqs. (A.1) and (A.3)

$$n^2 A(1 + r) = n_2^2 B \cosh (qD). \quad (\text{A.4})$$

Furthermore, $\vec{E}_t \propto \frac{\partial E_z}{\partial z}$ [cf. Eq. (2.6)] must be continuous, so

$$ik_z A(1 - r) = -Bq \sinh (qD). \quad (\text{A.5})$$

Taking the ratio of the above two equations and solving for r yields the modified Fresnel reflection coefficient

$$r_{\text{TM}}(D) = \frac{1 - i \frac{n_2^2 q}{n^2 k_z} \tanh (qD)}{1 + i \frac{n_2^2 q}{n^2 k_z} \tanh (qD)}. \quad (\text{A.6})$$

Writing the reflection coefficient as a pure phase as in Eq. (2.26) and inserting

$$q = k\sqrt{n_{\text{eff}}^2 - n_2^2} \quad \text{and} \quad k_z = k\sqrt{n^2 - n_{\text{eff}}^2} \quad (\text{A.7})$$

results in

$$\tan [\delta_{\text{TM}}(D)] = \frac{n^2 \sqrt{n_{\text{eff}}^2 - n_2^2}}{n_2^2 \sqrt{n^2 - n_{\text{eff}}^2}} \tanh \left(kD \sqrt{n_{\text{eff}}^2 - n_2^2} \right). \quad (\text{A.8})$$

The calculation for TE modes is analogous. Since B_z obeys Dirichlet boundary conditions at $z = D$, the field in II is

$$B_z^{(II)} = B\Psi \sinh [q(z - D)]e^{-i\omega t}. \quad (\text{A.9})$$

With B_z and $\vec{B}_t \propto \frac{\partial B_z}{\partial z}$ continuous at $z = 0$, we get

$$\begin{aligned} A(1 + r) &= -Bq \sinh(qD) & \text{and} \\ ik_z A(1 - r) &= Bq \cosh(qD), \end{aligned} \quad (\text{A.10})$$

leading to

$$r_{\text{TE}}(D) = \frac{1 - i \frac{\sqrt{n_{\text{eff}}^2 - n_2^2}}{\sqrt{n^2 - n_{\text{eff}}^2}} \coth(kD \sqrt{n_{\text{eff}}^2 - n_2^2})}{1 + i \frac{\sqrt{n_{\text{eff}}^2 - n_2^2}}{\sqrt{n^2 - n_{\text{eff}}^2}} \coth(kD \sqrt{n_{\text{eff}}^2 - n_2^2})} \quad (\text{A.11})$$

and

$$\tan [\delta_{\text{TE}}(D)] = \frac{\sqrt{n_{\text{eff}}^2 - n_2^2}}{\sqrt{n^2 - n_{\text{eff}}^2}} \coth \left(kD \sqrt{n_{\text{eff}}^2 - n_2^2} \right). \quad (\text{A.12})$$

For $qD \gg 1$, that means the metal plate is much further away than the penetration depth of the fields, the usual Fresnel reflection coefficients are recovered [cf. Eq. (2.29)].

A.1.2 Effective index of refraction with additional metal plate

The quantization condition for the effective index of refraction is deduced again from Eq. (2.25), but with r_2 replaced by $r_2(D)$ given by Eq. (A.6) or (A.11). The condition then reads

$$\begin{aligned} kb\sqrt{n^2 - n_{\text{eff}}^2} &= \zeta\pi + \arctan \left(\nu_1 \frac{\sqrt{n_{\text{eff}}^2 - n_1^2}}{\sqrt{n^2 - n_{\text{eff}}^2}} \right) + \\ &+ \arctan \left(\nu_2 \frac{\sqrt{n_{\text{eff}}^2 - n_2^2}}{\sqrt{n^2 - n_{\text{eff}}^2}} h \left[kD \sqrt{n_{\text{eff}}^2 - n_2^2} \right] \right) \end{aligned} \quad (\text{A.13})$$

with $\nu_j = n^2/n_j^2$ for TM and $\nu_j = 1$ for TE modes. The function $h(x)$ is

$$h(x) = \begin{cases} \tanh x & : \text{ TM} \\ \coth x & : \text{ TE} \end{cases}. \quad (\text{A.14})$$

When removing the metal plate, that is for $D \rightarrow \infty$, Eq. (2.29) is recovered. In the following, we will calculate $n_{\text{eff}}(D)$ for large D in order to understand the effect of the metal plate on the resonance frequencies (see Fig. 3.5), which is used to measure the polarization of resonance modes. The resonance frequencies are roughly proportional to $1/n_{\text{eff}}$. Thus, the direction of their shift due to the metal plate is determined from the sign of $\frac{\partial n_{\text{eff}}}{\partial D}$. To determine it, we rewrite Eq. (A.13) as

$$kb = \frac{1}{\sqrt{n^2 - n_{\text{eff}}^2}} \{\delta_1 + \delta_2(D) + \zeta\pi\} = g(n_{\text{eff}}, D) \quad (\text{A.15})$$

with $n_{\text{eff}} = n_{\text{eff}}(D)$ and the abbreviations

$$\delta_j(D) = \arctan\left(\eta_j h[D/(2\Delta)]\right) \quad \text{with} \quad \eta_j = \nu_j \frac{\sqrt{n_{\text{eff}}^2 - n_j^2}}{\sqrt{n^2 - n_{\text{eff}}^2}} \quad (\text{A.16})$$

and $\delta_j = \delta_j(D \rightarrow \infty)$. The term

$$\Delta_j = \frac{1}{2k\sqrt{n_{\text{eff}}^2 - n_j^2}} \quad (\text{A.17})$$

is the penetration depth of the field intensity into the medium with index of refraction n_j . For fixed k , the derivative of n_{eff} with respect to D is given with Eq. (A.15) as

$$\frac{\partial n_{\text{eff}}}{\partial D} = -\frac{\partial g}{\partial D} / \frac{\partial g}{\partial n_{\text{eff}}}. \quad (\text{A.18})$$

Since n_{eff} increases monotonically with kb , the quantity $\frac{\partial g}{\partial n_{\text{eff}}}$ is always positive [see Eq. (A.15)]. The other term is given as

$$\frac{\partial g}{\partial D} = \frac{1}{\sqrt{n^2 - n_{\text{eff}}^2}} \frac{\partial \delta_2}{\partial D} \quad (\text{A.19})$$

with

$$\frac{\partial \delta_2}{\partial D} = \frac{1}{1 + \eta_2^2 h^2} \frac{\eta_2}{2\Delta_2} h'[D/(2\Delta_2)]. \quad (\text{A.20})$$

The derivative of $h(x)$ is

$$h'(x) = \begin{cases} \frac{1}{\cosh^2(x)} & : \text{ TM} \\ -\frac{1}{\sinh^2(x)} & : \text{ TE} \end{cases}. \quad (\text{A.21})$$

In the limit of large x respectively D , in which we are interested, $h'(x)$ becomes

$$h'(x \rightarrow \infty) = 4ve^{-2x} \quad (\text{A.22})$$

with v equal to $+1$ for TM and to -1 for TE modes. Putting everything together yields

$$\frac{\partial n_{\text{eff}}}{\partial D} = -\frac{C}{\Delta_2} ve^{-D/\Delta_2} \quad (\text{A.23})$$

with the constant C given as

$$C = \frac{1}{\frac{\partial g}{\partial n_{\text{eff}}}} \frac{2}{\sqrt{n^2 - n_{\text{eff}}^2}} \frac{\eta_2}{1 + \eta_2^2 h^2[D/(2\Delta_2)]}. \quad (\text{A.24})$$

With $\frac{\partial g}{\partial n_{\text{eff}}} > 0$ and $\eta_2 > 0$ [see Eq. (A.16)] we obtain $C > 0$. We now expand $n_{\text{eff}}(D)$ around $D = \infty$ using

$$n_{\text{eff}}(D) - n_{\text{eff}}(D = \infty) = \int_{\infty}^D dD' \frac{\partial n_{\text{eff}}}{\partial D'} \approx -\frac{C|_{D=\infty}}{\Delta_2} v \int_{\infty}^D dD' e^{-D'/\Delta_2}, \quad (\text{A.25})$$

which leads to the final result

$$n_{\text{eff}}(D) \approx n_{\text{eff}}(D = \infty) + \begin{cases} +Ce^{-D/\Delta_2} & : \text{ TM} \\ -Ce^{-D/\Delta_2} & : \text{ TE} \end{cases}. \quad (\text{A.26})$$

This explains the resonance shifts in Fig. 3.5: For TM modes, the metal plate shifts n_{eff} to higher values, which leads to lower resonance frequencies since these are roughly $\propto 1/n_{\text{eff}}$. For TE modes, it is the other way round. The above approximation for n_{eff} is of course only valid for $D \gg \Delta_2$, but even beyond this regime n_{eff} is a strictly monotonic function of D , so that the measurement of the polarization with a metal plate works the same way also for small D .

A.2 Quasi-2d setup with air gap

The ansatz for a TM mode in the setup shown in Fig. A.3 is

$$E_z = \begin{cases} A\Psi(x, y) \cos[k_z z]e^{-i\omega t} & : 0 \leq z \leq b \\ B\Psi(x, y) \cos[\kappa_z(z - b - d)]e^{-i\omega t} & : b \leq z \leq b + d \end{cases} \quad (\text{A.27})$$

with A and B constants, b and d the thicknesses of the dielectric plate and the air gap, respectively, and

$$\kappa_z = \frac{1}{n} \sqrt{k_z^2 - (n^2 - 1)\gamma^2}, \quad (\text{A.28})$$

where γ^2 is the eigenvalue of the wave function Ψ . These fields satisfy the Neumann boundary conditions at the copper plates per construction, and from the boundary conditions at the dielectric interface at $z = b$ follows the quantization condition

$$\frac{k_z}{n^2} \tan(k_z b) = -\kappa_z \tan(\kappa_z d). \quad (\text{A.29})$$

Inserting Eq. (A.28) for κ_z in the limit of small air gaps and not too large frequencies, i.e. $k_z b, \kappa_z d \ll 1$, we obtain

$$-k_z^2 d + (n^2 - 1)\gamma^2 d = k_z^2 b. \quad (\text{A.30})$$

Inserting Eq. (A.7) and using $\gamma = n_{\text{eff}} k$ and $d/b \ll 1$ leads to the final result

$$n_{\text{eff}} = \frac{n}{1 + \frac{d}{2b}(n^2 - 1)} \quad (\text{A.31})$$

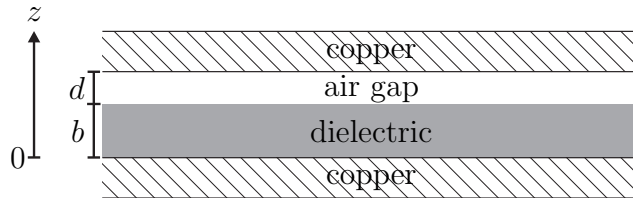


Fig. A.3: Dielectric plate between two copper plates with an air gap. The size of the air gap is exaggerated: the thickness of the air gap is usually $d < 0.1$ mm while the thickness of the dielectric plate is e.g. $b = 5$ mm.

for the effective index of refraction in the quasi-2d setup with a small air gap. It should be noted that the case of air gaps above and below the dielectric plate leads to the same expression when d is the total size of both air gaps. The formula demonstrates that e.g. an air gap as small as $d/b = 2\%$ leads to a deviation of n_{eff} from n which is about 1% of n with $n \approx 1.4$. For larger n , the deviation increases rapidly.

B Trace formula for single and multiple subspectra of the dielectric circle

B.1 Single resonance family

The resonance density for a series of resonances with wave numbers given as $k = f(m)$, where m is the quantum number and f is a monotonic function, is

$$\rho(k) = D|F'(k)| \left\{ 1 + 2 \sum_{\eta=1}^{\infty} \cos [2\pi\eta F(k)] \right\} \quad (\text{B.1})$$

where F is the inverse function of f , i.e. $m = F(k)$, and D is the degeneracy factor of the modes [12]. We consider a single family of resonances of the dielectric circle with fixed radial quantum number n_r , whose wave numbers are given by Eq. (5.14). The imaginary parts of the wave numbers k_{m,n_r} of the WGMs are small. Therefore, it is dropped to simplify the following calculations. The approximate inverse of Eq. (5.14) is

$$F_{n_r}(k) = Ak - Bx_{n_r}k^{1/3} + \frac{n}{\sqrt{n^2 - 1}} \quad (\text{B.2})$$

with

$$A = nR \quad \text{and} \quad B = \left(\frac{nR}{2} \right)^{1/3} \quad (\text{B.3})$$

and $D = 2$. We neglect the third term in $F(k)$ since it only adds a phase to the RD, and the dependence of F and x on the radial quantum number n_r is suppressed in the notation. As usually, the RD decomposes into a smooth part,

$$\rho_{\text{Weyl}}(k) = 2 \left(A - \frac{1}{3} Bxk^{-2/3} \right), \quad (\text{B.4})$$

and a fluctuating part,

$$\rho_{\text{fluc}}(k) = 4 \left(A - \frac{1}{3} Bxk^{-2/3} \right) \sum_{\eta=1}^{\infty} \cos [2\pi\eta(Ak - Bxk^{1/3})]. \quad (\text{B.5})$$

The corresponding length spectrum is then

$$\begin{aligned} \tilde{\rho}(\ell) &= \int_{k_{\min}}^{k_{\max}} dk e^{-ikn\ell} \rho_{\text{fluc}}(k) \\ &= 2 \sum_{\eta=1}^{\infty} \int_{k_{\min}}^{k_{\max}} dk \left(A - \frac{1}{3} Bxk^{-2/3} \right) e^{i(2\pi\eta F(k) - kn\ell)} \end{aligned} \quad (\text{B.6})$$

where in the cos-function the term $\exp\{-2\pi i\eta F(k)\}$ was omitted since it only gives a contribution for $\ell < 0$. This integral is computed with the stationary phase approximation

$$\int_{-\infty}^{\infty} dy h(y) e^{ig(y)} = \sqrt{\frac{2\pi}{|g''(y_0)|}} h(y_0) e^{i\{g(y_0) + \text{sign}[g''(y_0)]\pi/4\}} \quad (\text{B.7})$$

where $e^{ig(y)}$ is a rapidly oscillating function while h varies only slowly, and y_0 is the single stationary point of g . In our case,

$$g(k) = 2\pi\eta F(k) - kn\ell \quad (\text{B.8})$$

and the stationary point is

$$k_0 = \left(\frac{2/3 \pi \eta B x}{2\pi \eta A - \ell n} \right)^{3/2}. \quad (\text{B.9})$$

It should be noted that k_0 depends on η . The second derivative of g at the stationary point is then

$$g''(k_0) = \frac{4}{9} \pi \eta B x \left(\frac{2\pi \eta A - \ell n}{2/3 \pi \eta B x} \right)^{5/2}. \quad (\text{B.10})$$

With this the stationary phase approximation yields

$$\begin{aligned} \tilde{\rho}(\ell) &= 9 \sum_{\eta=1}^{\infty} \left(A - \frac{1}{3} B x_{n_r} k_0^{-2/3} \right) \frac{1}{\sqrt{2\pi \eta B x_{n_r}}} \left(\frac{2/3 \pi \eta B x_{n_r}}{2\pi \eta A - \ell n} \right)^{5/4} \times \\ &\quad \times \exp [i(2\pi \eta F(k_0) - k_0 \ell n + \text{sign}(k_0)\pi/4)] \\ &= \sum_{\eta=1}^{\infty} \frac{C(\eta)}{(2\pi R \eta - \ell)^{5/4}}. \end{aligned} \quad (\text{B.11})$$

This formula predicts an increase of $|\tilde{\rho}(\ell)|$ with ℓ and singularities at the multiples of the circumference, $2\pi R \eta$. The increase can indeed be seen in Fig. 5.5, but $|\tilde{\rho}(\ell)|$ has a peak and decreases again at a length $\ell < 2\pi R$. The reason for this is that the stationary phase approximation fails if the stationary point k_0 is outside the interval of integration $[k_{\min}, k_{\max}]$. This happens for lengths longer than a certain ℓ_0 and for $\ell > \ell_0$ the integral drops to zero quickly. The stationary point reaches k_{\max} for the length

$$\ell_0 = 2\pi R \eta \left(1 - \frac{1}{3nR} \left(\frac{nR}{2} \right)^{1/3} x_{n_r} k_{\max}^{-2/3} \right) < 2\pi R \eta, \quad (\text{B.12})$$

yielding that the peak in the length spectrum lies close to but below ℓ_0 and thus also below $2\pi R\eta$. This explains why the position of the peak in the length spectrum for a single resonance family depends on the maximal frequency considered, but is not related to any PO.

B.2 Two resonance families

In the following we will calculate the resonance density for the combination of two resonance families of the dielectric circle and the corresponding length spectrum. Adding the resonance densities $\rho_{\text{fluc}}(k)$ according to Eq. (B.5) for two families with different n_r (e.g. $n_r = 1$ and 2) and applying a trigonometric addition theorem results in the RD

$$\begin{aligned} \rho_{\text{fluc}}(k) &= 8 \left(A - \frac{1}{3} B \bar{x} k^{-2/3} \right) \times \\ &\times \sum_{\eta=1}^{\infty} \cos [2\pi\eta(A - B\bar{x}k^{1/3})] \cos [\pi\eta B\Delta x k^{1/3}] \end{aligned} \quad (\text{B.13})$$

with $\bar{x} = (x_1 + x_2)/2$ and $\Delta x = x_2 - x_1$. We calculate the corresponding length spectrum again with the stationary phase approximation and use that only the first cosine-term is a rapidly oscillating function of k . The result is

$$\begin{aligned} \tilde{\rho}(\ell) &= \sum_{\eta=1}^{\infty} \frac{2\ell n}{\eta} \sqrt{\frac{3}{\pi}} e^{i\Phi_\eta} \sqrt[4]{\frac{(2/3 \pi \eta B \bar{x})^3}{(2\pi n R \eta - \ell n)^5}} \times \\ &\times \cos \left[\pi \eta B \Delta x \sqrt{\frac{2/3 \pi \eta B \bar{x}}{2\pi n R \eta - \ell n}} \right]. \end{aligned} \quad (\text{B.14})$$

The details of the phase Φ_η are omitted here as it is irrelevant for what follows. Again, the stationary phase approximation is only valid for lengths shorter than ℓ_0 defined by Eq. (B.12) with x_{n_r} replaced by \bar{x} . The modulus of the cosine term is maximal for its argument equal to $q\pi$, where q is an integer, i.e. the peaks of $|\tilde{\rho}(\ell)|$ are expected at the lengths

$$\ell_{\text{max}}(q, \eta) = 2\pi R\eta \left[1 - \frac{\bar{x}}{6} \left(\frac{\eta \Delta x}{q} \right)^2 \right]. \quad (\text{B.15})$$

The numerical values of ℓ_{max} are compared with the exact lengths of the POs in the circle billiard in Table B.1. The agreement is very good for large q/η ,

q	$\ell_{\text{po}}(q, \eta = 1)$ (m)	$\ell_{\text{max}}(q, \eta = 1)$ (m)	$\Delta\ell$ (m)
3	1.4284	1.4126	0.0158
4	1.5551	1.5502	0.0049
5	1.6158	1.6140	0.0018
6	1.6494	1.6486	0.0008
7	1.6698	1.6694	0.0004
8	1.6832	1.6830	0.0002
9	1.6924	1.6923	0.0001
10	1.6990	1.6989	0.0001

Tab. B.1: Comparison of the lengths ℓ_{po} of the periodic orbits in the Teflon circle with the length ℓ_{max} according to Eq. (B.15). The values are computed for $R = 274.9$ mm and $\eta = 1$. The agreement is very good for large q , and reasonable even for smaller q . Reprinted from [104].

which explains the appearance of peaks at lengths close to those of the POs in Fig. 5.6(b). They are the result of an interference between the contributions of the two resonance families to the trace formula. Indeed, on one hand the lengths of the POs can be approximated as

$$\ell_{\text{po}}(q/\eta \rightarrow \infty) = 2\pi R\eta \left[1 - \frac{1}{6} \left(\frac{\eta\pi}{q} \right)^2 \right], \quad (\text{B.16})$$

and on the other hand it can be shown that in Eq. (B.15) the factor $\bar{x}(\Delta x)^2 \approx \pi^2$ for adjacent zeros x_j, x_{j+1} of the Airy-function $\text{Ai}(x)$, such that $\ell_{\text{max}}(q, \eta) \approx \ell_{\text{po}}(q, \eta)$.

C Exact trace formula for the dielectric circle billiard

In this appendix, the exact trace formula Eq. (6.4) is derived. The calculations are simplified as they ignore mathematical intricacies, and are based on [116]. In the following it will be assumed that n is frequency dependent, as is the case for $n_{\text{eff}}(k)$, but the explicit frequency dependence is suppressed for the sake of brevity.

The starting point is the quantization condition for the TM modes of the dielectric circle [see Eq. (3.3)],

$$s_m(x) = n \frac{J'_m}{J_m}(nx) - \frac{H_m^{(1)'}}{H_m^{(1)}}(x) \quad (\text{C.1})$$

where $x = kR$. The resonance density in terms of the roots k_{m,n_r} of $s_m(x)$ is written as

$$\rho(k) = \sum_{m=-\infty}^{+\infty} \sum_{n_r=1}^{\infty} \delta(k - k_{m,n_r}). \quad (\text{C.2})$$

An alternate expression for the RD would be a sum of Lorentzians, that is of “ δ ”-functions with finite widths, see Eq. (5.2). We now use that

$$\delta[g(z)] = \sum_j \frac{\delta(z - z_j)}{|g'(z)|} \quad (\text{C.3})$$

with z_j denoting the roots of $g(z)$ to obtain

$$\rho(k) = \sum_{m=-\infty}^{+\infty} \left| \frac{ds_m}{dk} \right| \delta[s_m(k)]. \quad (\text{C.4})$$

With $\lim_{\epsilon \rightarrow 0^+} \frac{1}{z+i\epsilon} = \mathcal{P}\frac{1}{z} - i\pi\delta(z)$ and $x = kR$ we arrive at

$$\rho(k) = -\frac{R}{\pi} \sum_{m=-\infty}^{+\infty} \left| \frac{ds_m}{dx} \right| \text{Im} \left(\frac{1}{s_m} \right). \quad (\text{C.5})$$

The next step is to calculate $\frac{ds_m}{dx} = \frac{\partial s_m}{\partial x} + \frac{\partial s_m}{\partial n} \frac{dn}{dx}$. The first term yields

$$\frac{\partial s_m}{\partial x} = n^2 \left[\frac{J_m''}{J_m}(nx) - \left(\frac{J_m'}{J_m} \right)^2 (nx) \right] - \left[\frac{H_m^{(1)''}}{H_m^{(1)'}}(x) - \left(\frac{H_m^{(1)'}}{H_m^{(1)'}} \right)^2 (x) \right]. \quad (\text{C.6})$$

With the property

$$\frac{Z_m''(z)}{Z_m(z)} = -\frac{Z_m'(z)}{zZ_m(z)} - \left(1 - \frac{m^2}{z^2}\right) \quad (\text{C.7})$$

of Bessel-functions Z_m this can be further simplified to

$$\frac{\partial s_m}{\partial x} = -(n^2 - 1) - \frac{s_m}{x} - s_m \left(n \frac{J_m'}{J_m}(nx) + \frac{H_m'^{(1)}}{H_m^{(1)}}(x) \right). \quad (\text{C.8})$$

The second term is

$$\frac{\partial s_m}{\partial n} = -nx \left[1 - \frac{m^2}{n^2 x^2} + \frac{1}{n^2} \left(\frac{H_m'^{(1)}}{H_m^{(1)}} \right)^2 (x) \right] \quad (\text{C.9})$$

where we replaced $\frac{J_m'}{J_m}(nx)$ by $\frac{1}{n} \frac{H_m'^{(1)}}{H_m^{(1)}}(x)$ since $s_m(x) = 0$. For $m \gg x$ we can use the approximation

$$\frac{H_m'^{(1)}}{H_m^{(1)}}(x) \approx -\sqrt{\frac{m^2}{x^2} - 1} \quad (\text{C.10})$$

to obtain

$$\frac{\partial s_m}{\partial n} = -\frac{x}{n}(n^2 - 1). \quad (\text{C.11})$$

It should be noted that this is the only approximation in the whole calculation, and it has been checked numerically that the approximation is very precise. Therefore, the final result Eq. (6.4) can be regarded as an exact trace formula. Thus, we get

$$\frac{\frac{ds_m}{dx}}{s_m} = -\frac{n^2 - 1}{s_m} - \frac{1}{x} - \left(n \frac{J_m'}{J_m}(nx) + \frac{H_m'^{(1)}}{H_m^{(1)}}(x) \right) - \frac{dn}{dx} \frac{x}{n} \frac{n^2 - 1}{s_m} \quad (\text{C.12})$$

It can be argued that only the first and fourth term give the relevant poles for $\rho(k)$ [116], and therefore the second and third one are dropped. The result is

$$\rho(k) = \frac{R(n^2 - 1)}{\pi} \left(1 + \frac{k}{n} \frac{dn}{dk} \right) \sum_{m=-\infty}^{+\infty} \text{Im} \left(\frac{1}{s_m} \right). \quad (\text{C.13})$$

which is Eq. (40) from [39] multiplied with $2k$ and the factor $(1 + \frac{k}{n} \frac{dn}{dk})$ to account for the frequency dependence of n . Following the procedure of [39] we finally obtain Eq. (6.4). For the sake of completeness, this is also outlined in the following. First we use $\text{Im}(z) = \frac{z}{2i} + \text{c.c.}$ to get

$$\rho(k) = \frac{R(n^2 - 1)}{2\pi i} \left(1 + \frac{k}{n} \frac{dn}{dk} \right) \sum_{m=-\infty}^{+\infty} \frac{1}{s_m(x)} + \text{c.c.} \quad (\text{C.14})$$

Next, we rewrite s_m in the more convenient form

$$s_m(x) = n \frac{H'_m{}^{(1)}(nx) + H'_m{}^{(2)}(nx)}{H_m^{(1)}(nx) + H_m^{(2)}(nx)} - \frac{H'_m{}^{(1)}(x)}{H_m^{(1)}(x)}. \quad (\text{C.15})$$

Extracting the term $[H_m^{(1)}(nx)/H_m^{(2)}(nx) + 1]^{-1}$ leads to

$$s_m(x) = \frac{1}{E_m(x) + 1} [E_m(x)A_m(x) + B_m(x)] \quad (\text{C.16})$$

with the definitions

$$\begin{aligned} E_m(x) &= \frac{H_m^{(1)}(nx)}{H_m^{(2)}(nx)}, \\ A_m(x) &= n \frac{H'_m{}^{(1)}(nx)}{H_m^{(1)}(nx)} - \frac{H'_m{}^{(1)}(x)}{H_m^{(1)}(x)} \quad \text{and} \\ B_m(x) &= n \frac{H'_m{}^{(2)}(nx)}{H_m^{(2)}(nx)} - \frac{H'_m{}^{(1)}(x)}{H_m^{(1)}(x)} \end{aligned} \quad (\text{C.17})$$

as in [39]. Then

$$\frac{1}{s_m(x)} = \frac{E_m + 1}{B_m} \frac{1}{E_m A_m / B_m + 1}, \quad (\text{C.18})$$

and with the definition

$$R_m(x) = -\frac{A_m(x)}{B_m(x)} \quad (\text{C.19})$$

and the geometric series $1/(1-z) = \sum_{q=0}^{\infty} z^q$ this becomes

$$\frac{1}{s_m(x)} = \frac{1}{B_m} + \left(1 + \frac{1}{R_m}\right) B_m \sum_{q=1}^{\infty} (E_m R_m)^q. \quad (\text{C.20})$$

The prefactor

$$\tilde{P}_m = \left(1 + \frac{1}{R_m}\right) B_m = \frac{n}{A_m B_m} \frac{H_m^{(1)} H_m^{(2)} - H_m^{(1)} H'_m{}^{(2)}}{H_m^{(1)} H_m^{(2)}}(nx) \quad (\text{C.21})$$

is simplified to

$$\tilde{P}_m = \frac{4i/(\pi x)}{A_m B_m H_m^{(1)}(nx) H_m^{(2)}(nx)} \quad (\text{C.22})$$

with the Wronskian [117]

$$W[H_m^{(2)}(z), H_m^{(1)}(z)] = \frac{4i}{\pi z}. \quad (\text{C.23})$$

Inserting the result for $1/s_m(x)$ into Eq. (C.14) yields

$$\rho(k) = \frac{R(n^2 - 1)}{2\pi i} \left(1 + \frac{k}{n} \frac{dn}{dk}\right) \sum_{m=-\infty}^{+\infty} \left(\frac{1}{B_m} + \tilde{P}_m \sum_{q=1}^{\infty} (E_m R_m)^q \right) + \text{c.c.} \quad (\text{C.24})$$

The first term, $1/B_m$, corresponds to the smooth part of the DOS and is therefore ignored in the following, leaving

$$\rho_{\text{fluc}}(k) = \frac{2R}{\pi^2 x} \sum_{m=-\infty}^{+\infty} P_m \sum_{q=1}^{\infty} (E_m R_m)^q + \text{c.c.} \quad (\text{C.25})$$

with

$$P_m = \frac{(n^2 - 1)(1 + \frac{k}{n} \frac{dn}{dk})}{A_m B_m H_m^{(1)}(nx) H_m^{(2)}(nx)}. \quad (\text{C.26})$$

With the Poisson-resummation formula this becomes

$$\rho_{\text{fluc}}(k) = \frac{2R}{\pi^2 x} \sum_{\eta=-\infty}^{+\infty} \int_{m=-\infty}^{+\infty} dm e^{2\pi i \eta m} P_m \sum_{q=1}^{\infty} (E_m R_m)^q + \text{c.c.} \quad (\text{C.27})$$

The last step is to replace the summation $\sum_{\eta=-\infty}^{+\infty} \sum_{q=1}^{\infty}$ by $2 \sum_{\eta=1}^{\infty} \sum_{q=2\eta}^{\infty} = 2 \sum_{\text{po}}$, where the fact was used that certain combinations of η and q do not give relevant contributions (namely those that do not correspond to POs). This yields the final result

$$\rho_{\text{fluc}}(k) = \frac{4}{\pi^2 k} \sum_{\eta=1}^{\infty} \sum_{q=2\eta}^{\infty} \int_{m=-\infty}^{+\infty} dm e^{2\pi i \eta m} P_m (R_m E_m)^q + \text{c.c.} \quad (\text{C.28})$$

The semiclassical trace formula Eq. (5.7) can then be deduced as presented in [39].

References

- [1] I. Newton: *Philosophiae naturalis principia mathematica* (Jussu Societas Regiae ac Typis Josephi Streater, London, 1686).
- [2] H. Poincaré: *Les Méthodes Nouvelles de la Méchanique Celeste* (Gauthier-Villars, Paris, 1892), reprinted in N.A.S.A. Translation TTF-450/452, U.S. Fed. Clearinghouse, Springfield, VA, USA (1967).
- [3] H. G. Schuster: *Deterministic Chaos* (VHC, Weinheim, 1989).
- [4] O. Bohigas, M. J. Giannoni, and C. Schmit: *Characterization of Chaotic Quantum Spectra and Universality of Level Fluctuation Laws*, Phys. Rev. Lett. **52**, 1 (1984).
- [5] J. B. Garg, J. Rainwater, J. S. Petersen, and W. W. Havens, Jr.: *Neutron Resonance Spectroscopy. III. Th^{232} and U^{238}* , Phys. Rev. **134**, B985 (1964).
- [6] R. U. Haq, A. Pandey, and O. Bohigas: *Fluctuation Properties of Nuclear Energy Levels: Do Theory and Experiment Agree?*, Phys. Rev. Lett. **48**, 1086 (1982).
- [7] J. Enders, T. Guhr, A. Heine, P. von Neumann-Cosel, V. Y. Ponomarev, A. Richter, and J. Wambach: *Spectral statistics and the fine structure of the electric pygmy dipole resonance in $N=82$ nuclei*, Nucl. Phys. A **741**, 3 (2004).
- [8] S. Åberg, A. Heine, G. Mitchell, and A. Richter: *Isospin symmetry breaking in ^{93}Tc and statistical properties*, Phys. Lett. B **598**, 42 (2004).
- [9] H. Friedrich and D. Wintgen: *The hydrogen atom in a uniform magnetic field — An example of chaos*, Phys. Rep. **183**, 37 (1989).
- [10] M. C. Gutzwiller: *Energy Spectrum According to Classical Mechanics*, J. Math. Phys. **11**, 1791 (1970).
- [11] M. C. Gutzwiller: *Periodic Orbits and Classical Quantization Conditions*, J. Math. Phys. **12**, 343 (1971).
- [12] M. Brack and R. K. Bhaduri: *Semiclassical Physics* (Westview Press, Oxford, 2003).

- [13] E. N. Lorenz: *Deterministic Nonperiodic Flow*, J. Atmos. Sci. **20**, 130 (1963).
- [14] L. A. Bunimovich: *On the Ergodic Properties of Nowhere Dispersing Billiards*, Commun. Math. Phys. **65**, 295 (1979).
- [15] C. M. Marcus, A. J. Rimberg, R. M. Westervelt, P. F. Hopkins, and A. C. Gossard: *Conductance Fluctuations and Chaotic Scattering in Ballistic Microstructures*, Phys. Rev. Lett. **69**, 506 (1992).
- [16] H.-J. Stöckmann: *Quantum Chaos: An Introduction* (Cambridge University Press, Cambridge, England, 2000).
- [17] A. Richter: *Playing Billiard with Microwaves — Quantum Manifestations of Classical Chaos*, in *Emerging Applications of Number Theory*, **109**, The IMA Volumes in Mathematics and its Applications, Ed.: D. A. Hejhal, J. Friedmann, M. C. Gutzwiller, and A. M. Odlyzko (Springer, New York, 1999), pp. 479–523.
- [18] H. Alt, H.-D. Gräf, R. Hofferbert, C. Rangacharyulu, H. Rehfeld, A. Richter, P. Schardt, and A. Wirzba: *Chaotic dynamics in a three-dimensional superconducting microwave billiard*, Phys. Rev. E **54**, 2303 (1996).
- [19] H. Alt, C. Dembowski, H.-D. Gräf, R. Hofferbert, H. Rehfeld, A. Richter, R. Schuhmann, and T. Weiland: *Wave Dynamical Chaos in a Superconducting Three-Dimensional Sinai Billiard*, Phys. Rev. Lett. **79**, 1026 (1997).
- [20] P. Bertelsen, C. Ellegaard, T. Guhr, M. Oxborrow, and K. Schaadt: *Measurement of Parametric Correlations in Spectra of Resonating Quartz Blocks*, Phys. Rev. Lett. **83**, 2171 (1999).
- [21] K. Schaadt, T. Guhr, C. Ellegaard, and M. Oxborrow: *Experiments on elastomechanical wave functions in chaotic plates and their statistical features*, Phys. Rev. E **68**, 036205 (2003).
- [22] S. L. McCall, A. F. J. Levi, R. E. Slusher, S. J. Pearton, and R. A. Logan: *Whispering-gallery mode microdisk lasers*, Appl. Phys. Lett. **60**, 289 (1992).

- [23] *Optical Microcavities*, Advanced Series in Applied Physics, Ed.: K. Vahala (World Scientific Publishing Co. Pte. Ltd., Singapore, 2004).
- [24] D. K. Armani, T. J. Kippenberg, S. M. Spillane, and K. J. Vahala: *Ultra-high- Q toroid microcavity on a chip*, Nature **421**, 925 (2003).
- [25] L. Collot, V. Lefèvre-Seguin, M. Brune, J. M. Raimond, and S. Haroche: *Very High- Q Whispering-Gallery Mode Resonances Observed on Fused Silica Microspheres*, Europhys. Lett. **23**, 327 (1993).
- [26] J. U. Nöckel, A. D. Stone, and R. K. Chang: *Q spoiling and directionality in deformed ring cavities*, Opt. Lett. **19**, 1693 (1994).
- [27] J. U. Nöckel and A. D. Stone: *Ray and wave chaos in asymmetric resonant optical cavities*, Nature **385**, 45 (1997).
- [28] J. Wiersig and M. Hentschel: *Combining Directional Light Output and Ultralow Loss in Deformed Microdisks*, Phys. Rev. Lett. **100**, 033901 (2008).
- [29] C. Yan, Q. J. Wang, L. Diehl, M. Hentschel, J. Wiersig, N. Yu, C. Pflügl, F. Capasso, M. A. Belkin, T. Edamura, M. Yamanishi, and H. Kan: *Directional emission and universal far-field behavior from semiconductor lasers with limaçon-shaped microcavity*, Appl. Phys. Lett. **94**, 251101 (2009).
- [30] Q. Song, W. Fang, B. Liu, S.-T. Ho, G. S. Solomon, and H. Cao: *Chaotic microcavity laser with high quality factor and unidirectional output*, Phys. Rev. A **80**, 041807 (2009).
- [31] J. Wiersig and M. Hentschel: *Unidirectional light emission from high- Q modes in optical microcavities*, Phys. Rev. A **73**, 031802 (2006).
- [32] H. G. L. Schwefel, N. B. Rex, H. E. Tureci, R. K. Chang, A. D. Stone, T. Ben-Messaoud, and J. Zyss: *Dramatic shape sensitivity of directional emission patterns from similarly deformed cylindrical polymer lasers*, J. Opt. Soc. Am. B **21**, 923 (2004).
- [33] R. Schäfer, U. Kuhl, and H.-J. Stöckmann: *Directed emission from a dielectric microwave billiard with quadrupolar shape*, New J. Phys. **8**, 46 (2006).

- [34] E. G. Altmann: *Emission from dielectric cavities in terms of invariant sets of the chaotic ray dynamics*, Phys. Rev. A **79**, 013830 (2009).
- [35] E. J. Heller: *Bound-State Eigenfunctions of Classically Chaotic Hamiltonian Systems: Scars of Periodic Orbits*, Phys. Rev. Lett. **53**, 1515 (1984).
- [36] C. Gmachl, E. E. Narimanov, F. Capasso, J. N. Baillargeon, and A. Y. Cho: *Kolmogorov-Arnold-Moser transition and laser action on scar modes in semiconductor diode lasers with deformed resonators*, Opt. Lett. **27**, 824 (2002).
- [37] T. Harayama, T. Fukushima, P. Davis, P. O. Vaccaro, T. Miyasaka, T. Nishimura, and T. Aida: *Lasing on scar modes in fully chaotic microcavities*, Phys. Rev. E **67**, 015207(R) (2003).
- [38] M. Lebental, N. Djellali, C. Arnaud, J.-S. Lauret, J. Zyss, R. Dubertrand, C. Schmit, and E. Bogomolny: *Inferring periodic orbits from spectra of simply shaped microlasers*, Phys. Rev. A **76**, 023830 (2007).
- [39] E. Bogomolny, R. Dubertrand, and C. Schmit: *Trace formula for dielectric cavities: General properties*, Phys. Rev. E **78**, 056202 (2008).
- [40] J. D. Jackson: *Classical Electrodynamics* (John Wiley & Sons, Inc., New York, 1999).
- [41] H. G. L. Schwefel, A. D. Stone, and H. E. Tureci: *Polarization properties and dispersion relations for spiral resonances of a dielectric rod*, J. Opt. Soc. Am. B **22**, 2295 (2005).
- [42] J. Wiersig: *Boundary element method for resonances in dielectric microcavities*, J. Opt. A **5**, 53 (2002).
- [43] J. U. Nöckel and R. K. Chang: *2-d Microcavities: Theory and Experiments*, Contribution for Cavity-Enhanced Spectroscopies, edited by Roger D. van Zee and John P. Looney (a volume of Experimental Methods in the Physical Sciences), Academic Press, San Diego, 2002.
- [44] M. Hentschel and K. Richter: *Quantum chaos in optical systems: The annular billiard*, Phys. Rev. E **66**, 056207 (2002).

- [45] H. E. Türeci, H. G. L. Schwefel, P. Jacquod, and A. D. Stone: *Modes of wave-chaotic dielectric resonators*, Progress in Optics **47**, 75 (2005).
- [46] J. W. S. Rayleigh: *Scientific Papers, vol. 5* (Cambridge University Press, London, 1912), pp. 617–620.
- [47] A. E. Bate: *Note on the whispering gallery of St Paul’s Cathedral, London*, Proc. Phys. Soc. **50**, 293 (1938).
- [48] M. Lebental, J. S. Lauret, R. Hierle, and J. Zyss: *Highly directional stadium-shaped polymer microlasers*, Appl. Phys. Lett. **88**, 031108 (2006).
- [49] G. D. Chern, H. E. Tureci, A. D. Stone, R. K. Chang, M. Kneissl, and N. M. Johnson: *Unidirectional lasing from InGaN multiple-quantum-well spiral-shaped micropillars*, Appl. Phys. Lett. **83**, 1710 (2003).
- [50] E. I. Smotrova, A. I. Nosich, T. M. Benson, and P. Sewell: *Cold-Cavity Thresholds of Microdisks With Uniform and Nonuniform Gain: Quasi-3-D Modeling With Accurate 2-D Analysis*, IEEE Selected Topics in Quantum Electronics **11**, 1135 (2005).
- [51] C. Mahaux and H. A. Weidenmüller: *Shell-Model Approach to Nuclear Reactions* (North Holland, Amsterdam, 1969).
- [52] H. Alt, P. von Brentano, H.-D. Gräf, R. Hofferbert, M. Philipp, H. Rehfeld, A. Richter, and P. Schardt: *Precision Test of the Breit-Wigner Formula on Resonances in a Superconducting Microwave Cavity*, Phys. Lett. B **366**, 7 (1996).
- [53] U. Fano: *Effects of Configuration Interaction on Intensities and Phase Shifts*, Phys. Rev. **124**, 1866 (1961).
- [54] F. Schäfer: *Untersuchung der Zeitumkehrinvarianz in Quantenbillards*, Diplomarbeit, TU Darmstadt, 2005 (unpublished).
- [55] H.-D. Gräf, H. L. Harney, H. Lengeler, C. H. Lewenkopf, C. Rangacharyulu, A. Richter, P. Schardt, and H. A. Weidenmüller: *Distribution of Eigenmodes in a Superconducting Stadium Billiard with Chaotic Dynamics*, Phys. Rev. Lett. **69**, 1296 (1992).

- [56] C. Gmachl, F. Capasso, E. E. Narimanov, J. U. Nöckel, A. D. Stone, J. Faist, D. L. Sivco, and A. Y. Cho: *High-Power Directional Emission from Microlasers with Chaotic Resonators*, Science **280**, 1556 (1998).
- [57] J. Dai, C. X. Xu, K. Zheng, C. G. Lv, and Y. P. Cui: *Whispering gallery-mode lasing in ZnO microrods at room temperature*, Appl. Phys. Lett. **95**, 241110 (2009).
- [58] J. Yang, S. Moon, S.-B. Lee, J.-H. Lee, K. An, J.-B. Shim, H.-W. Lee, and S.-W. Kim: *Development of a deformation-tunable quadrupolar microcavity*, Rev. Sci. Instrum. **77**, 083103 (2006).
- [59] M. Ghulinyan, D. Navarro-Urrios, A. Pitanti, A. Lui, G. Pucker, and L. Pavesi: *Whispering-gallery modes and light emission from a Si-nanocrystal-based single microdisk resonator*, Opt. Express **16**, 13218 (2008).
- [60] Q. Song, H. Cao, S. T. Ho, and G. S. Solomon: *Near-IR Subwavelength Microdisk Lasers*, Appl. Phys. Lett. **94**, 061109 (2009).
- [61] S. Bittner, B. Dietz, M. Miski-Oglu, P. Oria Iriarte, A. Richter, and F. Schäfer: *Experimental test of a two-dimensional approximation for dielectric microcavities*, Phys. Rev. A **80**, 023825 (2009).
- [62] M. D. Janezic, E. F. Kuester, and J. B. Jarvis: *Broadband complex permittivity measurements of dielectric substrates using a split-cylinder resonator*, IEEE MTT-S International Microwave Symposium Digest **3**, 1817 (2004).
- [63] G. Kent: *An evanescent-mode tester for ceramic dielectric substrates*, IEEE Transactions on Microwave Theory and Techniques **36**, 1451 (1988).
- [64] L. C. Maier and J. C. Slater: *Field Strength Measurements in Resonant Cavities*, J. Appl. Phys. **23**, 68 (1952).
- [65] E. Bogomolny, B. Dietz, T. Friedrich, M. Miski-Oglu, A. Richter, F. Schäfer, and C. Schmit: *First Experimental Observation of Superscars in a Pseudointegrable Barrier Billiard*, Phys. Rev. Lett. **97**, 254102 (2006).
- [66] M. Miski-Oglu: *Superscars und Statistik der Knotengebiete in einem symmetrischen Barrierenbilliard*, Dissertation D17, TU Darmstadt, 2007.

- [67] G. Annino, D. Bertolini, M. Cassettari, M. Fittipaldi, I. Longo, and M. Martinelli: *Dielectric properties of materials using whispering gallery dielectric resonators: Experiments and perspectives of ultra-wideband characterization*, J. Chem. Phys. **122**, 2308 (2000).
- [68] Computer Simulation Technology AG (CST): *CST Studio Suite*, <http://www.cst.com>.
- [69] C. Classen, B. Bandlow, and R. Schumann: *Computational Analysis of Whispering Gallery Modes in Flat Dielectric Disks*, (unpublished).
- [70] S. W. McDonald: *Wave dynamics of regular and chaotic rays*, Technical Report No. LBL-14837, Lawrence Berkley Laboratory Report, 1983, (unpublished).
- [71] S. Sridhar: *Experimental Observation of Scarred Eigenfunctions of Chaotic Microwave Cavities*, Phys. Rev. Lett. **67**, 785 (1991).
- [72] E. Bogomolny and C. Schmit: *Structure of Wave Functions of Pseudointegrable Billiards*, Phys. Rev. Lett. **92**, 244102 (2004).
- [73] T. M. Antonsen, E. Ott, Q. Chen, and R. N. Oerter: *Statistics of wavefunction scars*, Phys. Rev. E **51**, 111 (1995).
- [74] S. Åberg, T. Guhr, M. Miski-Oglu, and A. Richter: *Superscars in billiards: A model for doorway states in quantum spectra*, Phys. Rev. Lett. **100**, 204101 (2008).
- [75] H. E. Tureci, H. G. L. Schwefel, A. D. Stone, and E. E. Narimanov: *Gaussian-optical approach to stable periodic orbit resonances of partially chaotic dielectric micro-cavities*, Opt. Express **10**, 752 (2002).
- [76] J. Unterhinninghofen, J. Wiersig, and M. Hentschel: *Goos-Hänchen shift and localization of optical modes in deformed microcavities*, Phys. Rev. E **78**, 016201 (2008).
- [77] S.-Y. Lee, S. Rim, J.-W. Ryu, T.-Y. Kwon, M. Choi, and C.-M. Kim: *Quasiscarred Resonances in a Spiral-Shaped Microcavity*, Phys. Rev. Lett. **93**, 164102 (2004).

- [78] S.-Y. Lee, S. Rim, J.-W. Ryu, T.-Y. Kwon, M. Choi, and C.-M. Kim: *Ray and wave dynamical properties of a spiral-shaped dielectric microcavity*, J. Phys. A **41**, 275102 (2008).
- [79] C.-M. Kim, S. H. Lee, K. R. Oh, and J. H. Kim: *Experimental verification of quasiscarred resonance mode*, Appl. Phys. Lett. **94**, 231120 (2009).
- [80] E. G. Altmann, G. Del Magno, and M. Hentschel: *Non-Hamiltonian dynamics in optical microcavities resulting from wave-inspired corrections to geometric optics*, Europhys. Lett. **84**, 10008 (2008).
- [81] P. J. Richens and M. V. Berry: *Pseudointegrable systems in classical and quantum mechanics*, Physica D **2**, 495 (1981).
- [82] A. W. Poon, F. Courvoisier, and R. K. Chang: *Multimode resonances in square-shaped optical microcavities*, Opt. Lett. **26**, 632 (2001).
- [83] E. Marchena, S. Shi, and D. Prather: *Fabrication and characterization of optimized corner-cut square microresonators*, Opt. Express **16**, 16516 (2008).
- [84] I. Braun, G. Ihlein, F. Laeri, J. U. Nöckel, G. Schulz-Ekloff, F. Schüth, U. Vietze, Ö. Weiß, and D. Wöhrle: *Hexagonal microlasers based on organic dyes in nanoporous crystals*, Appl. Phys. B **70**, 335 (2000).
- [85] D. Wang, H. W. Seo, C.-C. Tin, M. J. Bozack, J. R. Williams, M. Park, and Y. Tzeng: *Lasing in whispering gallery mode in ZnO nanonails*, J. Appl. Phys. **99**, 093112 (2006).
- [86] Morgan Advanced Ceramics: data sheet “DeranoxTM995”.
- [87] J. Stein, H.-J. Stöckmann, and U. Stoffregen: *Microwave Studies of Billiard Green Functions and Propagators*, Phys. Rev. Lett. **75**, 53 (1995).
- [88] T. Tudorovskiy, R. Höhmann, U. Kuhl, and H. J. Stöckmann: *On the theory of cavities with point-like perturbations: part I. General theory*, J. Phys. A **41**, 275101 (2008).
- [89] U. Kuhl, E. Persson, M. Barth, and H.-J. Stöckmann: *Mixing of wavefunctions in rectangular microwave billiards*, Eur. Phys. J. B **17**, 253 (2000).

- [90] E. Bogomolny and C. Schmit: *Asymptotic behaviour of multiple scattering on an infinite number of parallel half-planes*, Nonlinearity **16**, 2035 (2003).
- [91] J. Wiersig: *Formation of Long-Lived, Scarlike Modes near Avoided Resonance Crossings in Optical Microcavities*, Phys. Rev. Lett. **97**, 253901 (2006).
- [92] V. V. Sokolov and V. Zelevinsky: *Simple mode on a highly excited background: Collective strength and damping in the continuum*, Phys. Rev. C **56**, 311 (1997).
- [93] H. Kohler, H.-J. Sommers, S. Åberg, and T. Guhr: *Exact fidelity and full fidelity statistics in regular and chaotic surroundings*, Phys. Rev. E **81**, 050103(R) (2010).
- [94] H. Kohler, H.-J. Sommers, and S. Åberg: *Survival probability of a doorway state in regular and chaotic environments*, J. Phys. A **43**, 215102 (2010).
- [95] H. Kohler, T. Guhr, and S. Åberg: *Coupling coefficient distribution in the doorway mechanism*, New J. Phys. **12**, 073026 (2010).
- [96] M. L. Du and J. B. Delos: *Effect of Closed Classical Orbits on Quantum Spectra: Ionization of Atoms in a Magnetic Field*, Phys. Rev. Lett. **58**, 1731 (1987).
- [97] H. Olofsson, S. Åberg, O. Bohigas, and P. Leboeuf: *Correlations in Nuclear Masses*, Phys. Rev. Lett. **96**, 042502 (2006).
- [98] R. Balian and B. Duplantier: *Electromagnetic Waves Near Perfect Conductors. I. Multiple Scattering Expansions. Distribution of Modes*, Ann. Phys. (N.Y.) **104**, 300 (1977).
- [99] O. Frank and B. Eckhardt: *Eigenvalue density oscillations in separable microwave resonators*, Phys. Rev. E **53**, 4166 (1996).
- [100] C. Dembowski, B. Dietz, H.-D. Gräf, A. Heine, T. Papenbrock, A. Richter, and C. Richter: *Experimental Test of a Trace Formula for a Chaotic Three-Dimensional Microwave Cavity*, Phys. Rev. Lett. **89**, 064101 (2002).

- [101] A. Wirzba, N. Søndergaard, and P. Cvitanović: *Wave chaos in elastodynamic cavity scattering*, Europhys. Lett. **72**, 534 (2005).
- [102] G. Tanner and N. Søndergaard: *Wave chaos in acoustics and elasticity*, J. Phys. A **40**, R443 (2007).
- [103] Y.-F. Chen, Y.-T. Yu, Y.-J. Huang, P.-Y. Chiang, K.-W. Su, and K.-F. Huang: *Extracting photon periodic orbits from spontaneous emission spectra in laterally confined vertically emitted cavities*, Opt. Lett. **35**, 2723 (2010).
- [104] S. Bittner, E. Bogomolny, B. Dietz, M. Miski-Oglu, P. Oria Iriarte, A. Richter, and F. Schäfer: *Experimental test of a trace formula for two-dimensional dielectric resonators*, Phys. Rev. E **81**, 066215 (2010).
- [105] D. Lacey, J. C. Gallop, and L. E. Davis: *The effects of an air gap on the measurement of the dielectric constant of SrTiO₃ at cryogenic temperatures*, Meas. Sci. Technol. **9**, 536 (1998).
- [106] W. H. Press, B. P. Flannery, S. A. Teukolsky, and W. T. Vetterling: *Numerical Recipes: The Art of Scientific Computing* (Cambridge University Press, Cambridge, 1987).
- [107] M. Sieber, H. Primack, U. Smilansky, I. Ussishkin, and H. Schanz: *Semi-classical quantization of billiards with mixed boundary conditions*, J. Phys. A **28**, 5041 (1995).
- [108] M. Hentschel and H. Schomerus: *Fresnel laws at curved dielectric interfaces of microresonators*, Phys. Rev. E **65**, 045603(R) (2002).
- [109] W. Fang and H. Cao: *Wave interference effect on polymer microstadium laser*, Appl. Phys. Lett. **91**, 041108 (2007).
- [110] R. Dubertrand, E. Bogomolny, N. Djellali, M. Lebental, and C. Schmit: *Circular dielectric cavity and its deformations*, Phys. Rev. A **77**, 013804 (2008).
- [111] E. Bogomolny and R. Dubertrand: *Dielectric cavities of simple forms and dynamical localization*, (private communication).

- [112] K.-J. Che, Y.-D. Yang, and Y.-Z. Huang: *Mode Characteristics for Square Resonators With a Metal Confinement Layer*, IEEE Journal of Quantum Electronics **46**, 414 (2010).
- [113] J. Wiersig: *Hexagonal dielectric resonators and microcrystal lasers*, Phys. Rev. A **67**, 023807 (2003).
- [114] F. Goos and H. Hänchen: *Ein neuer und fundamentaler Versuch zur Totalreflexion*, Ann. Phys. **436**, 333 (1947).
- [115] K. Artmann: *Zur Reflexion einer seitlich begrenzten Lichtwelle am dünneren Medium in einigem Abstand vom Grenzwinkel der Totalreflexion*, Ann. Phys. **443**, 270 (1950).
- [116] E. Bogomolny: *Proof of formula (66)*, (private communication).
- [117] H. Bateman: in *Higher Transcendental Functions*, vol. II, Ed.: A. Erdélyi (McGraw-Hill, New York, 1953).

Acknowledgments

Last but not least, I would also like to thank all the people who have helped and supported me in the making of this thesis.

First of all I would like to thank Professor Dr. Dr. h.c. mult. Achim Richter for giving me the opportunity of working in the great quantum chaos group in Darmstadt. His continuous and determined encouragement is a source of inspiration for me and all other members of the quantum chaos group.

I also want to thank Professor Dr. Wambach for taking over the Korreferat.

Dr. Eugene Bogomolny I want to thank for all our discussions and the hospitality provided in Orsay. None of the results presented in this thesis would have been possible without his help and his profound physical insight.

Furthermore my thanks go to my parents and my family for giving me trust and encouragement in all my endeavors. I could not have wished for greater support. My thanks of course also go to all the present and previous members of the quantum chaos group who have made my time in Darmstadt most memorable. Among these are Dr. Barbara Dietz–Pilatus whom I want to thank for the support with her great mathematical skills and all the long hours that she spent reading and improving my manuscripts, Dr. Thomas Friedrich who introduced me to the fascinating field of quantum chaos, Dr. Maksim Miski-Oglu who introduced me to the art of wave function measurements and who with his great knowledge in experimental technique has influenced my work more than anybody else, Dr. Florian Schäfer whose skill with computers and care of the electronic infrastructure of our group has been the base of all of our work, and Dr. Pedro Oria Iriarte for the great time that we spent together here. Last but not least I would like to mention all the other people who have worked or are working in the quantum chaos group. You have helped to make this group the best and most lively one in the world.

Thanks also go to Professor Dr. Thomas Weiland, Dr. Wolfgang Ackermann and Dr. Wolfgang Müller from TEMF for their help with numerical simulations and the provision of computer power.

The work presented in this thesis was supported by the DFG within the subproject of C4 of the SFB 634.

Lebenslauf

Stefan Bittner

18. Oktober 1980	geboren in Frankfurt am Main
1987–2000	Schulbildung (Grundschule, Gymnasium) in Frankfurt am Main
Juni 2000	Abitur
2001–2007	Studium der Physik an der Technischen Universität Darmstadt
März 2007	Diplom in Physik; Abschluss des Studiums
seit April 2007	Doktorand am Institut für Kernphysik an der Technischen Universität Darmstadt

